

Mesoscale Convective Cloud Rings in the Tropics

By
David C. Loranger

Department of Atmospheric Science
Colorado State University
Fort Collins, Colorado

This research was supported by the NSF, Atmospheric Sciences Section,
under Grant GA-31588.
November 1974



**Department of
Atmospheric Science**

MESOSCALE
CONVECTIVE CLOUD RINGS
IN THE TROPICS

by

David C. Loranger

This research was supported by the National Science Foundation,
Atmospheric Sciences Section, under Grant GA-31588

Department of Atmospheric Science

Colorado State University

Ft. Collins, Colorado

80523

November, 1974

Atmospheric Science Paper Number 229

ABSTRACT

The physical, thermodynamic and dynamic characteristics of convective cloud rings (open cell convection) occurring on July 18, 1969 during the fourth phase of the Barbados Oceanographic and Meteorological Experiment (BOMEX) in the tropical North Atlantic Ocean are studied in detail. A time-consistent non-random configuration of growing and decaying cumulus elements comprising the cloud ring and a relatively clear center area forms the primary definition of cloud ring structures. Single and multiple occurrences are observed. Data from the ATS III geosynchronous satellite, from BOMEX fixed ship station weather radar and from aircraft provide cloud ring size, height, motion and life-time information. Fixed ship station surface and radiosonde and Nimbus III sun-synchronous satellite observations provide synoptic scale surface and upper air temperature, moisture and wind field data. Synoptic scale horizontal velocity divergence and relative vorticity profiles are obtained using a polygon method; vertical velocity profiles are kinematically computed from the divergence profiles. Both single time and time mean values and profiles of thermodynamic and dynamic parameters are obtained.

The BOMEX July 18 tropical cloud rings have a mean diameter of 80 km, a mean height of 6 km, a lifetime of 6 hours and display motion with the mean wind over their depth. Occurrence is located in a relatively undisturbed weather region associated with a surface and upper level anticyclone. Deep ring cloud elements appear to precipitate.

Thermodynamically the ring occurrence region is characterized by a moist, relatively unstable boundary layer and a (lower) middle level stable layer with rapid drying above; otherwise the atmosphere is nearly moist adiabatic to the tropopause. Significant upward heat flux from the ocean is prevalent beneath the rings. Dynamically the cloud rings are occurring in a region of light wind speeds and small vertical shear over their depth. Low level cyclonic and high level anticyclonic horizontal shear prevails in the area. Low level convergence, upward motion and cyclonic relative vorticity and mid to higher level divergence, subsidence and anticyclonic relative vorticity are prevalent. Correlation is made between physical, thermodynamic and dynamic results. Ring and non-ring region meteorological conditions are found to differ in many respects.

Comparison of the BOMEX results with other tropical and mid latitude cloud ring investigation findings reveals a significant similarity, plus a strong correlation between stable layer height and cloud height. A single case of cloud ring passage over a ship station reveals significant drying in the ring center. Ring occurrence thermodynamic conditions are found to lie close in many details to those of the tropical mean, while the dynamic situation differs significantly from the mean and lies intermediate between disturbed and undisturbed weather cases.

A basic circulation model of cloud rings including correlations with thermodynamic and dynamic parameter distributions is presented.

Cloud ring mesoscale data are now needed to further the understanding of these convective structures and lead to their parameterization in atmospheric diagnostic and prognostic models.

ACKNOWLEDGMENTS

Sincere thanks for their assistance in accomplishing this study and preparing the paper are extended to Dr. Thomas H. Vonder Haar, Dr. Wayne Schubert, Dr. Eberhard Ruprecht and Dr. Howard Frisinger, presently at Colorado State University, and to Dr. Thomas McKee and Dr. Hans Korff, formerly at Colorado State University, for their invaluable personal communications and advice. I also thank Ms. Charline Polifka for computer programming aid, to Pam Ragouzis for drafting the figures and to Ms. Lyn Koch and Ms. Cheryl Ellefson for typing the manuscript. Further appreciation is extended to Dr. William Marlatt of CSU for providing the cloud ring photographs presented in the Introduction. This research was supported by the Atmospheric Sciences Section of the National Science Foundation under Grant GA-31588.

TABLE OF CONTENTS

	<u>Page</u>
ABSTRACT.	ii
ACKNOWLEDGMENTS	iv
TABLE OF CONTENTS	v
LIST OF TABLES.	vii
LIST OF FIGURES	viii
1.0 INTRODUCTION	1
1.1 Scope and Purpose	1
1.2 Cloud Ring Definition	4
2.0 BOMEX DATA: ANALYSIS AND RESULTS.	6
2.1 Cloud Ring Physical Description	13
2.1.1 ATS III Satellite.	13
2.1.1.1 Dimensions.	18
2.1.1.2 Duration.	19
2.1.1.3 Motion.	20
2.1.2 Weather Radar.	21
2.1.2.1 Cloud Height.	23
2.1.3 Aircraft Cloud Photography and Meteorological Observations.	30
2.1.3.1 Supporting.	30
2.1.3.2 Non-Supporting.	31
2.1.4 Summary.	31
2.2 Cloud Ring Thermodynamic Description.	32
2.2.1 Temperature.	34
2.2.2 Moisture	38
2.2.3 General T-q Findings	39
2.2.4 Summary.	41
2.3 Cloud Ring Dynamic Description.	42
2.3.1 Winds.	43
2.3.2 Divergence	48
2.3.3 Vertical Velocity.	53
2.3.4 Relative Vorticity	57
2.3.5 Summary.	60

TABLE OF CONTENTS (cont.)

	<u>Page</u>
3.0 CLOUD RING - TROPICAL ATMOSPHERE COMPARISONS	62
3.1 Physical Comparisons	62
3.2 Thermodynamic Comparisons.	65
3.3 Dynamics Comparisons	81
4.0 SUMMARY DISCUSSION AND HYPOTHESES	92
4.1 Cloud Ring System Composite Summary.	92
4.2 Cloud Ring Model Hypotheses.	94
5.0 CONCLUSIONS	99
REFERENCES	105
APPENDIX A. ATS III CAMERA SYSTEM TECHNICAL ASPECTS AND DATA PROCESSING.	108
I. Analog to Digital Data Conversion and Use.	108
II. ATS III Digital Data Normalization Procedure	110
APPENDIX B. RADAR CLOUD HEIGHT DETERMINATION.	119
I. Cloud Height Goometry.	119
II. Apparent Cloud Height Correction	123
APPENDIX C. POLYGON METHOD DYNAMIC PARAMETER CALCULATIONS	127
I. Horizontal Divergence.	127
II. Relative Vorticity	132

LIST OF TABLES

<u>Table</u>	<u>Page</u>
1 Cloud Ring Size, BOMEX Phase IV July 18, 1969 South Ring Grid.	19
2 BOMEX Fixed Ships - Barbados Polygon Data.	50
3 Cloud Ring Physical Description: Comparison of Various Investigation Findings	63
4 Cloud Ring Thermodynamic Description: Comparison of Various Investigation Findings	77
5 Cloud Ring System: Present Understanding.	100
6 Comparison and Contrast of Tropical and Mid-Latitude Convective Cloud Rings	101

LIST OF FIGURES

<u>Figure</u>		<u>Page</u>
1A	Convective Cloud Ring Structure Observed in the 1969 BOMEX area.	2
1B	Same as Figure 1A	2
2	July 18, 1969 1431Z ATS III MSCC Visible Spectrum Cloud Photograph, Tropical North Atlantic Position, with BOMEX Ring Study Grids Outlined (Dashed Lines)	7
3	July 18, 1969 BOMEX Phase IV Fixed Ship, Aircraft, Island and Satellite Observation Locations, with Ring Study Grids Outlined (Dashed Lines)	9
4	July 18, 1969 12Z North Atlantic Region WMO Surface Analysis, with Ring Study Grids Outlined (Dashed Lines) .	10
5	Same as Figure 4 for 700 mb level	11
6	Same as Figure 4 for 500 mb level	12
7	July 18, 1969 1431Z ATS III Digitized Cloud Picture, Portion of South BOMEX Ring Study Grid, Showing Cloud Ring Structures	15
8	July 18, 1969 1431 ATS III Range Printout Cloud Picture, Portion of South BOMEX Ring Study Grid, Showing Cloud Ring Structures and Figure 7 Area Outline	17
9	BOMEX July 18 1433Z <u>Discoverer</u> Weather Radar PPI Scope Cloud Echo Picture at 0° Antenna Elevation and Normal Gain (Horizontal Range Circles at 50 nm Intervals) . . .	24
10	BOMEX July 18 Fixed Ship Rawinsonde Temperature and Dew Point Soundings and Nimbus III SIRS-A Radiation Inversion Temperature Soundings.	35
11	BOMEX July 18 Fixed Ship Wind Field Observations Time-North ↔ South Space - Height Cross Section Plotted in Conventional Wind Observation Symbols. (Half feather = 5 kts, Full feather = 10 kts)	45
12	BOMEX July 18 15Z Ring Study Area Horizontal Velocity Divergence Vertical Profiles Obtained Using Polygon Method.	52

<u>Figure</u>	<u>Page</u>
13 BOMEX July 18 15Z Ring Study Area Vertical Velocity Vertical Profiles Kinematically Computed from Fig- ure 12 Horizontal Divergence Profiles	55
14 Same as Figure 12 for Relative Vorticity.	59
15 BOMEX July 18 Fixed Ship Rawinsonde Temperature and Dew Point and NIMBUS III SIRS-A Radiation Inversion Temperature Soundings and BOMEX Phase IV mean SIRS-A Temperature Soundings	67
16 BOMEX July 18 and BOMEX Phase IV Mean Fixed Ship Rawinsonde Temperature and Dew Point Soundings.	69
17 BOMEX Phase IV Time-Height Cross Section of Fixed Ship <u>Discoverer</u> 12Z Daily Temperature (0°C) Anomaly Profiles Based on Rawinsonde Data (Contour Interval 1°C).	72
18 Same as Figure 17 for Specific Humidity Moisture in gr/kg (Contour Interval 1 gr/kg).	73
19 APEX March 19, 1969 R.V. <u>Meteor</u> Equivalent Potential Temperature θ_e Time - Height Cross Sections during Cloud Ring Passage over Ship Station (After Ruprecht et al, 1973).	80
20 BOMEX July 18 and BOMEX Phase IV Mean Fixed Ship Rawin- sonde Zonal (u) and Meridional (v) Component Winds Aloft Profiles.	83
21 BOMEX July 18 and BOMEX Phase IV Mean Ring Study Area Horizontal Velocity Divergence Vertical Profiles Obtained Using Polygon Method	85
22 BOMEX July 18 and BOMEX Phase IV Mean Ring Study Area Vertical Velocity Vertical Profiles Kinematically Com- puted from Figure 21 Horizontal Divergence Profiles . . .	87
23 Same as Figure 21 for Relative Vorticity.	88
24 Zonal (u) Component Winds Aloft Profiles in Regions of Ring Cloud Occurrence as Obtained from Various Cloud Ring Investigations	90
A1 Sun - Reflective Element - Satellite Geometry (After Sikula and Vonder Haar, 1972)	115
B1 Radar Cloud Height Geometry	120

1.0 INTRODUCTION

1.1 Scope and Purpose

A particular cloud phenomenon, first noted over the North Atlantic Ocean from TIROS I cloud pictures by Krueger and Fritz (1961), by Vonder Haar et al. (1968) from ATS I pictures over the equatorial Pacific Ocean and by others intermediately, is a generally circular cloud structure whose form is that of a doughnut with convective cells forming the cloud ring and a clear area at the center. The tropical structures noted by Vonder Haar and colleagues were observed to be embedded in the easterly flows near the equator. They occurred generally in clusters, were on the order of a degree of latitude maximum diameter, and had lifetimes of at least 8 hours with estimates on the order of 14 to 16 hours. In the time mean the clouds forming the rings covered about 3/4 of the ring circle.

The study presented in this paper deals basically with the analysis of similar cloud ring structures noted in ATS III pictures of the tropical North Atlantic Ocean area during the 1969 Barbados Oceanographic and Meteorological Experiment (BOMEX). Examples of the BOMEX cloud rings are shown in the aerial photographs Figs. 1A and 1B taken at ~10 km altitude from the NASA Convair 990 aircraft. It is found that an estimated 20 percent of the BOMEX days show cloud ring patterns of some sort occurring in the area, that these rings are on the order of 80 km in diameter and that they have a lifetime of ~6 hours. Results from the physical analyses of these ring cloud structures will be compared to available findings in other ring cloud studies, some of which are mentioned above. For the first time a detailed study of the synoptic

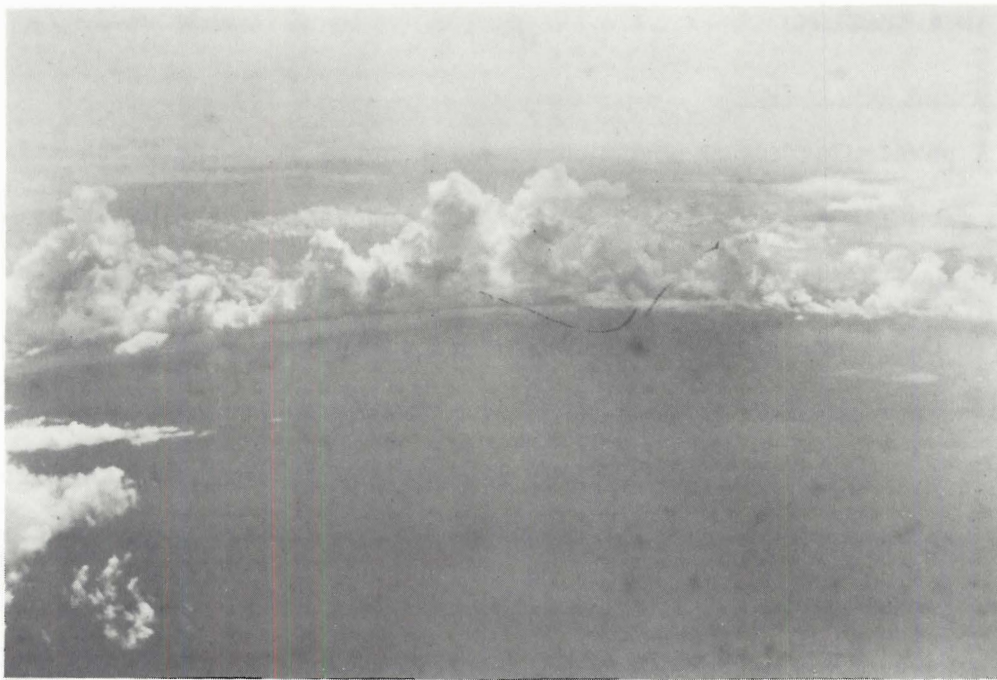


Figure 1A Convective Cloud Ring Structure Observed in the 1969 BOMEX area.



Figure 1B Same as Figure 1A.

scale thermodynamic and dynamic environments of the rings will be presented. Comparison of these findings with other cloud ring investigation results will be made. Comparison of ring occurrence conditions to appropriate mean conditions will also be made.

There are two major purposes for this study. The first purpose is to attain as complete an understanding as is presently possible of the nature of convective cloud ring systems including their interactions with other atmospheric scales of motion. The second purpose, following from the first and forming the ultimate though not presently realizable goal of this study, is to discover means by which the ring cloud system processes, the understanding of which is deduced from the ring cloud investigation findings, can be entered in atmospheric circulation prognostic or diagnostic models. Entering as many of the real atmospheric processes as possible into a model and entering these processes as accurately as possible makes the model and its output more closely representative of the real atmosphere. Numerous studies of cumulus convection scale processes are at present underway with a major purpose of incorporating these small scale, but important, processes into atmospheric models. Presently available and future knowledge of the mesoscale ring cloud structures in the tropics will lead to their role in the atmospheric circulation also being incorporated into the models, resulting in a better understanding of atmospheric circulation processes as a whole.

This report is extracted from the Master's Thesis (Loranger, 1974) in which additional detail is presented.

1.2 Cloud Ring Definition

Before delving in detail into the discussion of ring clouds in this paper, a definition must be made of exactly what is meant by the terms "ring," "ring pattern," and "ring structure," all of which are used synonymously. So far rings have been referred to as a generally circular, usually broken, cloud wall surrounding a clear area. This condition could be met, however, by a random distribution of clouds which, at a given time and place come together in the stated pattern. This is not what is meant by "rings" in this study. The critical condition for "rings" in the present study is duration of the pattern. We are looking for ring structures that show persistence of form with time and that do not change configuration over a short period as, for example, a cloud mass appearing in the center of a previous "apparent" ring. This would indicate that this situation was not a part of the persistent pattern being looked for, but was likely a random occurrence. These determinations of persistence or non-persistence in the present study are mainly accomplished utilizing sequences of ATS III photographs, with note of any cloud drift. In describing the persistent pattern of rings, it is important to note that it is not meant that the pattern is exactly the same, element for element, from observation to observation. It is the general form of cloud rings and clear centers that must remain the same. However there may be changes in the makeup of the ring walls with regard to the amount of cloudiness present there or change in ring size or shape. A notable change is that of ring cloudiness, in which a portion of a ring will be filled in by clouds at one time and at the next observation that portion is cloud free and another

segment of the ring may have filled in with cloud cells whereas that segment was cloud free previously. Thus the persistent pattern is a kind of "mold" in which clouds form and decay in the ring wall portion and clear centers appear in the middle of the ring forms. The cloud and clear center distribution is then just the visual result of the invisible flow pattern that is causing convection to occur in a certain way in certain places. It is this flow pattern that is the persistent system under study in actuality. One study which showed the existence of this persistent ring pattern was mentioned above and other investigations, as stated, have noted structures of a ring nature. A further definition of the rings under study here is that of "open cell" convection, discussed in several theoretical and observational investigations, as compared to "closed cell" convection.

2.0 BOMEX DATA: ANALYSIS AND RESULTS

The day chosen for the detailed study of cloud rings was July 18, 1969 during the BOMEX Phase IV which covered the period from July 11 to July 28, 1969. On this day the ATS III pictures show a number of rings present in the BOMEX area. The July 18 1431Z BOMEX area ATS III cloud photo with cloud rings within the dashed portions is shown in Figure 2. ATS pictures for this day are available starting at 1100Z and every 25 minutes thereafter until 1456Z. From the end of the 1456Z picture until the 1818Z picture starts, there are no ATS picture data available.* This gap in the ATS satellite photographic data is one shortcoming of the chosen day in regard to ring duration and motion calculations to be discussed in detail later. A single BOMEX area ESSA 7 satellite cloud picture is available at ~1700Z and provides some qualitative cloud ring data in the ATS III data gap. Cloud rings are also observed to occur in the BOMEX area in varying numbers on other days of the fourth phase and also during the earlier three phases of the BOMEX (~20 percent of the days) and thus are not to be considered an exclusive occurrence of July 18 only. Additional BOMEX cloud picture data are available from RB-57 aircraft flights from ~18 km altitude and NOAA Research Flight Facility (RFF) aircraft flights from near surface to 5.5 km altitudes. Surface meteorological observation data including sea surface temperatures, as well as marine observations, are available at fixed ship station locations in the BOMEX area. Fixed ship rawinsonde

* Note that all ATS picture times mentioned in this paper refer to the start times of the picture, i.e., when the camera starts its scan from north to south over the earth disk. Adding 25 minutes gives the end time of a picture for a full scan, 13 minutes added for a half scan.

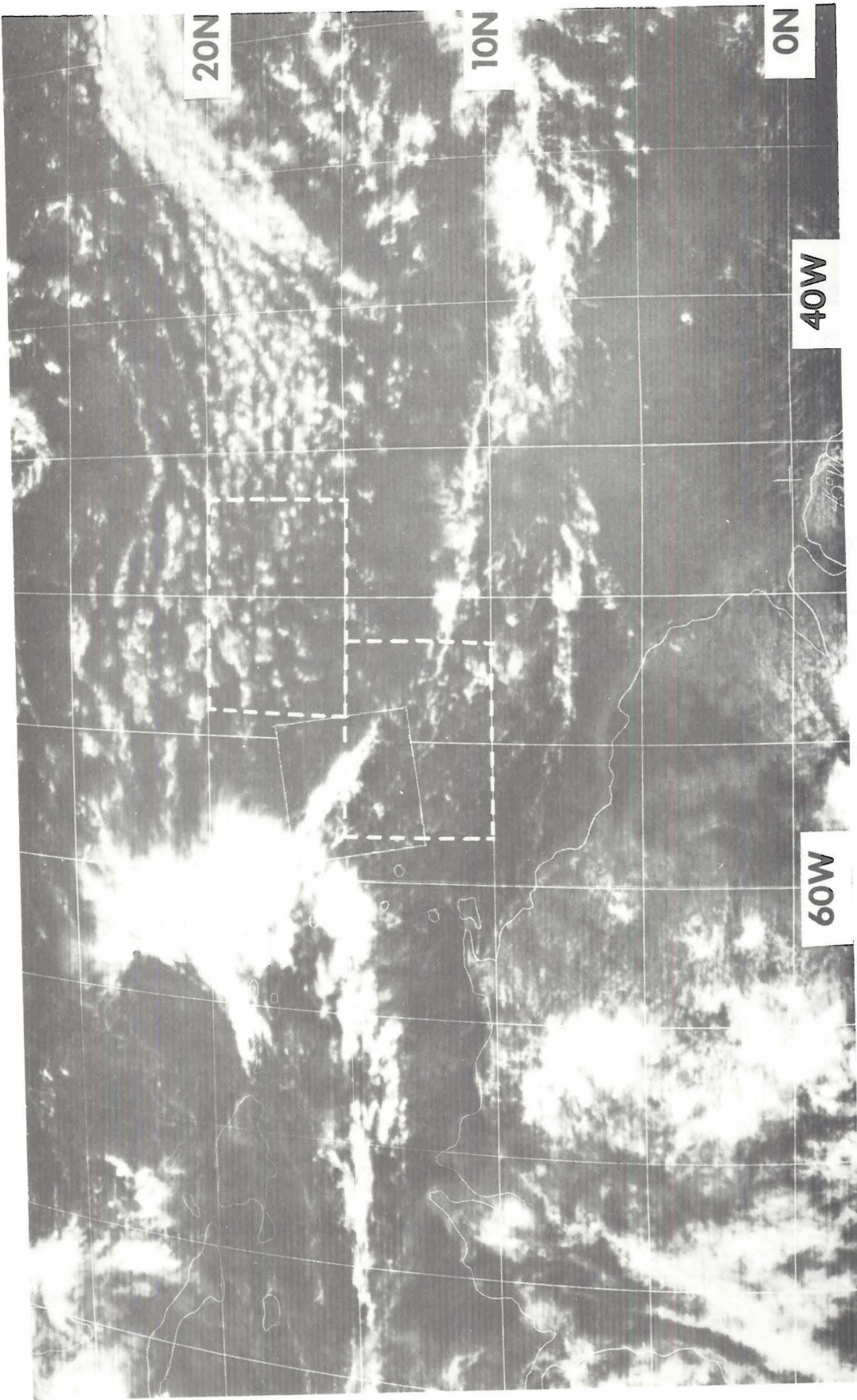


Figure 2 July 18, 1969 1431Z ATS III MSCC Visible Spectrum Cloud Photograph, Tropical North Atlantic Portion, with BOMEX Ring Study Grids Outlined (Dashed Lined).

ascents, as well as RFF and other aircraft, provide upper level temperature, moisture and wind data. In addition there are solar and terrestrial radiation measurements by aircraft, radiometersonde and satellite, from the latter of which are available inferred sea surface temperature and vertical temperature profile data (Nimbus III SIRS-A). Fixed ship Discoverer and Barbados, West Indies weather radar data are also available. Film loops, created from a day's sequence of ATS III cloud pictures and allowing ease of observation of weather system motions and evolution, are available for July 18, 1969 and selected other days and years in both the BOMEX and other regions.

With the good availability of data for the desired portions of the study on July 18, along with a sizeable number of ring structures, the chosen day is considered a good choice. Figure 3 shows the BOMEX area along with the July 18 Phase IV fixed ship locations, aircraft data flight tracks, Nimbus III satellite sounding locations, and Ring Study Grids.

The portion of the BOMEX region chosen in which rings were observed was divided into North Grid and South Grid areas. The North Grid boundary was set at 15N to 20N Latitude and 47W to 54W Longitude and the South Grid was defined by 10N to 15N Latitude and 52W to 58W Longitude. These were chosen both to encompass the ring structures and to allow for their motion. The synoptic meteorological situation at 1200Z on July 18, displayed by WMO surface, 700 mb, and 500 mb analyses, is shown in Figures 4 through 6 whereon the Ring Study Grids have also been located. From the maps it can be seen that there is a tropical easterly wave located to the west of the ring areas and that the ring

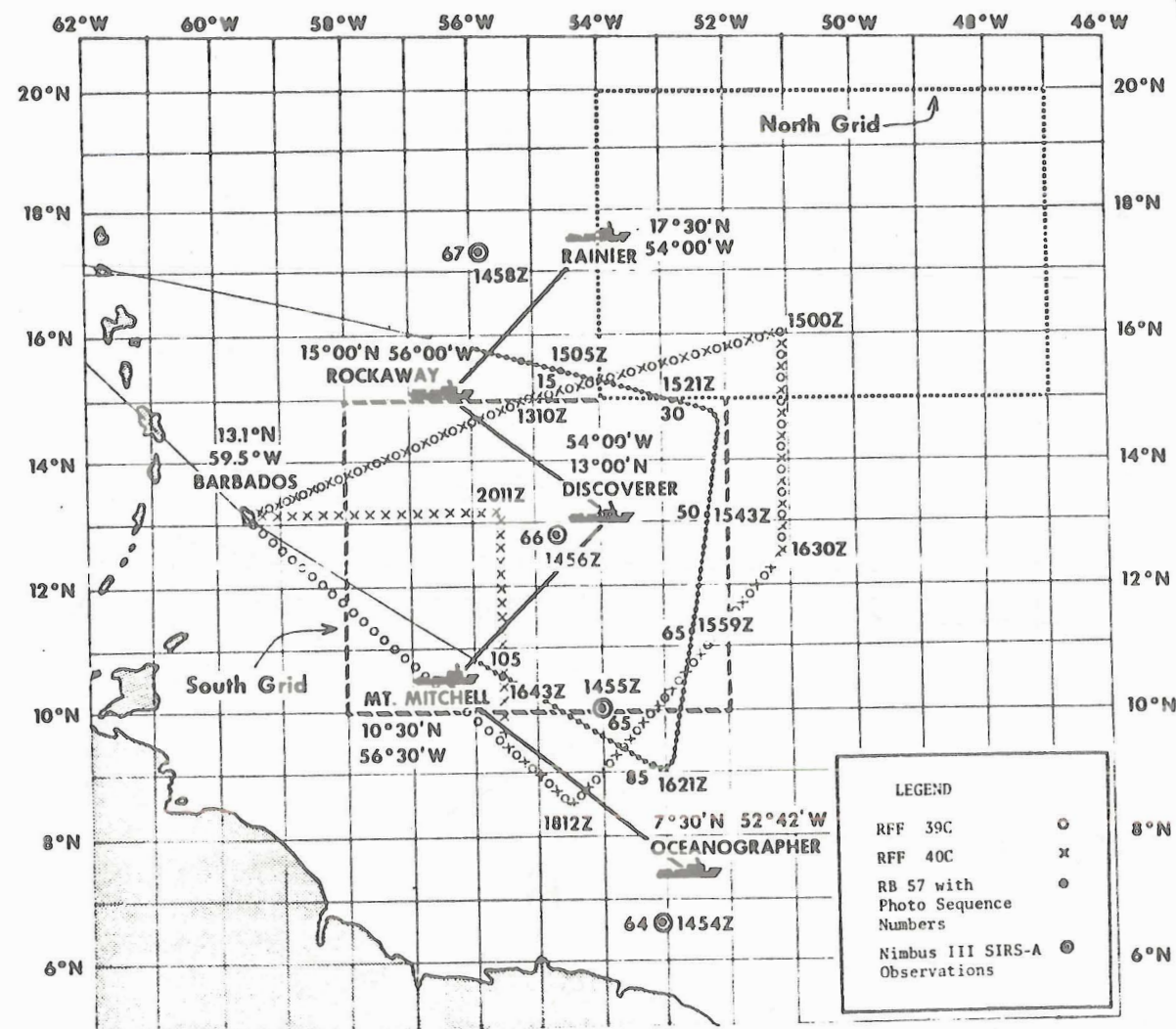


Figure 3 July 18, 1969 BOMEX Phase IV Fixed Ship, Aircraft, Island and Satellite Observation Locations, with Ring Study Grids Outlined (Dashed Lines).

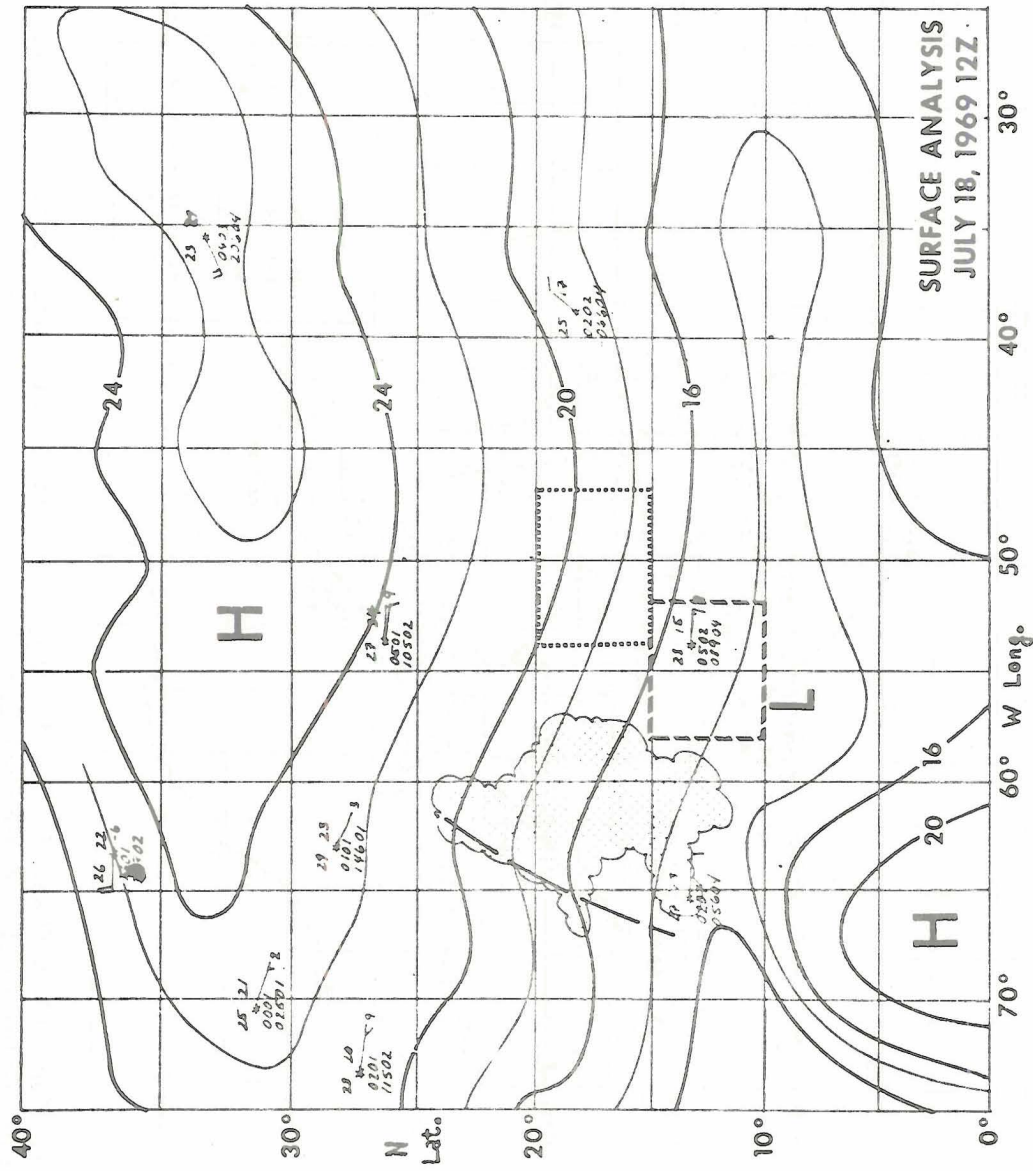


Figure 4 July 18, 1969 12Z North Atlantic Region WMO Surface Analysis, with Ring Study Grids Outlined (Dashed Lines).

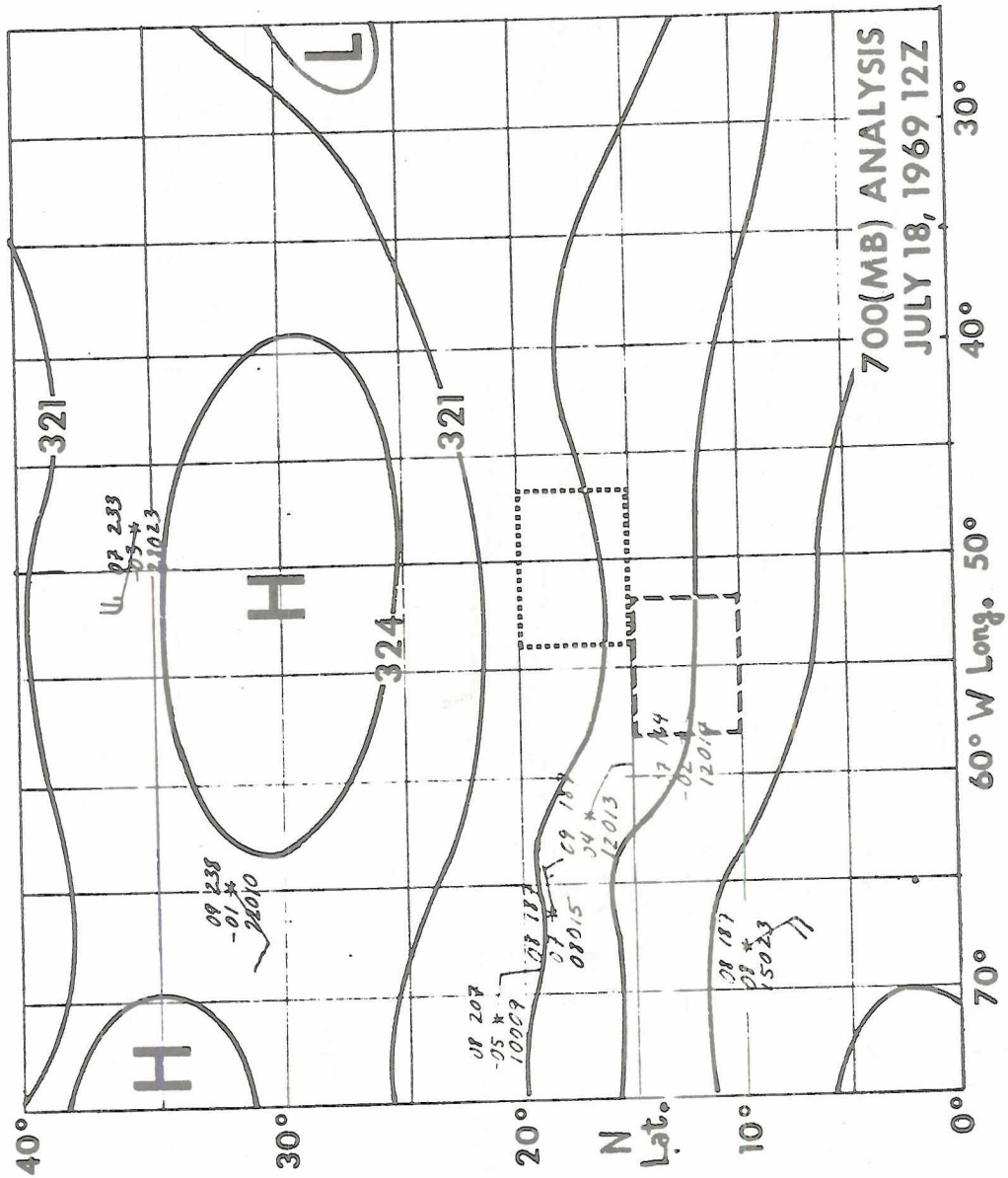


Figure 5 Same as Figure 4 for 700 mb level.

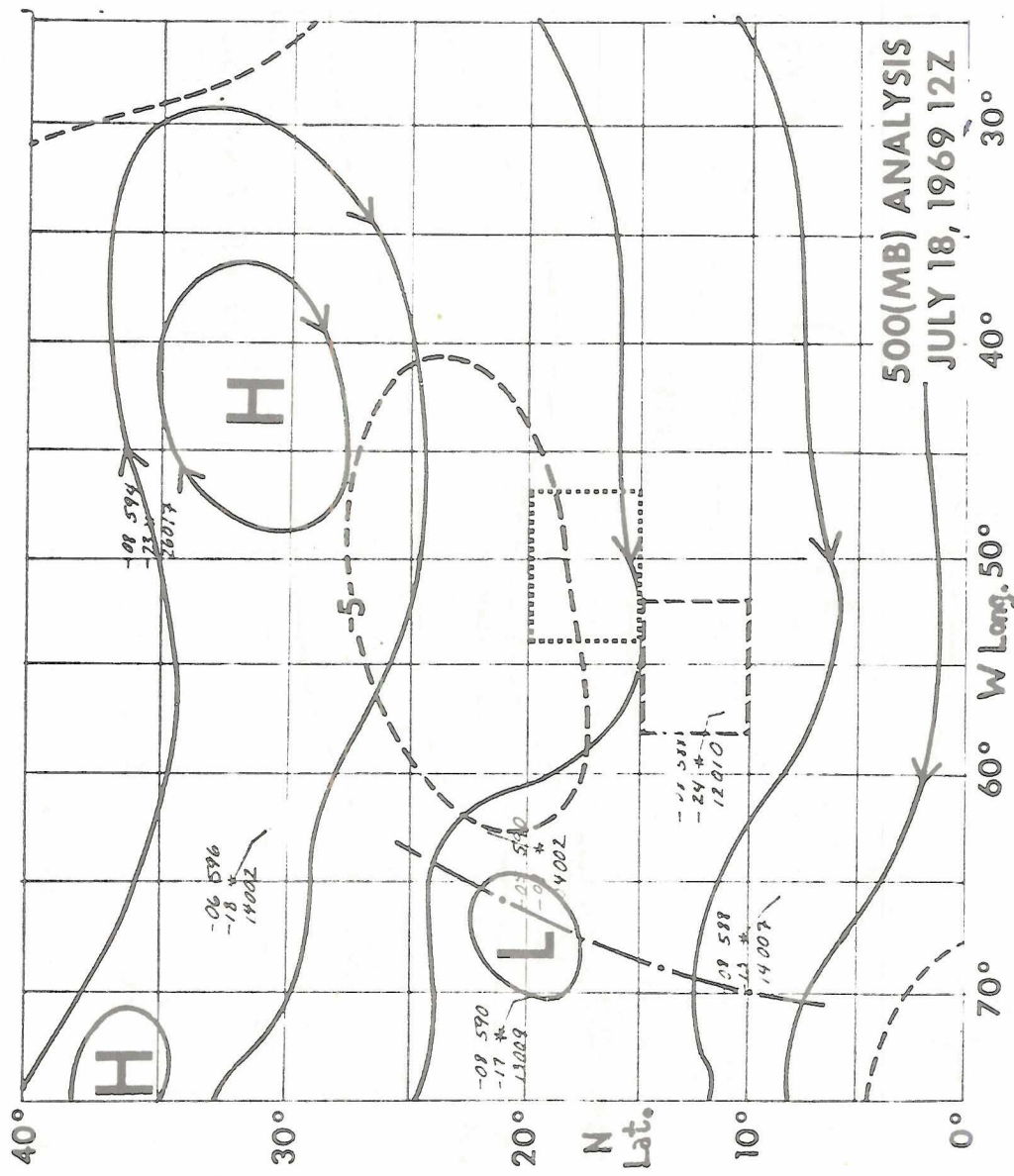


Figure 6 Same as Figure 4 for 500 mb level.

areas are located in the "ridge" region of the easterly flow, while the disturbance is the "trough" area. The ring areas are seen to be located on the southern side of the surface anticyclone, away from the high pressure center toward the equatorial edge. The cloud pattern over the area as seen in the satellite photographs also bears out the wave nature of the flow on this day. The 1431Z ATS III cloud picture in Figure 2 shows this cloud pattern as well as the ring patterns under study with the chosen grid areas also denoted. Thus a first look at the synoptic pattern shows that the rings appear to be a phenomena of the less disturbed tropical areas. There are none observed "near" the disturbed area on this day. The picture also shows more rings present in the South Grid area than in the North Grid area and that some also occur at other South Grid latitudes, but further east.

2.1 Cloud Ring Physical Description

2.1.1 ATS III Satellite

The satellite cloud photographs are very useful for initial viewing of the cloud patterns present. However, more quantitative analyses are possible using the magnetic tape digital data computer printouts of the satellite camera data, which digital data tapes are prepared from the analog data magnetic tapes. These tape data represent the ATS III camera system voltage output at the ground, which voltage is proportional to the reflected solar energy (cloud or other reflective element brightness) input to the camera at the satellite. This reflected power P_{rs} is defined by:

$$P_{rs} = N_{rs} \omega_c A_c \quad [2-1]$$

where N_{rs} is the reflected radiance at the satellite, ω_c is the solid angle field of view of the camera (0.1 milliradian or ~2nm earth spot size at geosynchronous altitude) and A_c is the camera aperture area. The analog voltage data are then linearly converted to a proportional set of digital values from 1 to 255 where brighter clouds or other reflective elements are represented by higher digital values. The ATS III analog data to digital data conversion is discussed in detail in Appendix A, Part I.

The ATS III digital data tapes are utilized to print out the July 18 1247Z, 1431Z and 1818Z North and South Ring Study Grids cloud pictures. These times were chosen to span the duration of the cloud ring patterns and allow for non-excessive motion between pictures. The digital printouts are contour analyzed, as in pressure surface analysis, etc., yielding a picture of cloud (including cellular structure) and clear regions. A minimum contour value of 40 is chosen mainly for its continuity and generally delineates the boundary between well-defined cloud masses and small scattered cloud elements with considerable clear space. A portion of the South Ring Grid July 18 1431Z digital cloud picture, displaying the contour analysis in the region of numerous rings, is presented in Figure 7.

A subsequent mechanical method of digital data contouring is employed. During the printout process the original digital data are represented by symbols representative of given digital value ranges. The above July 18 ATS III picture and digital value 40 minimum contour

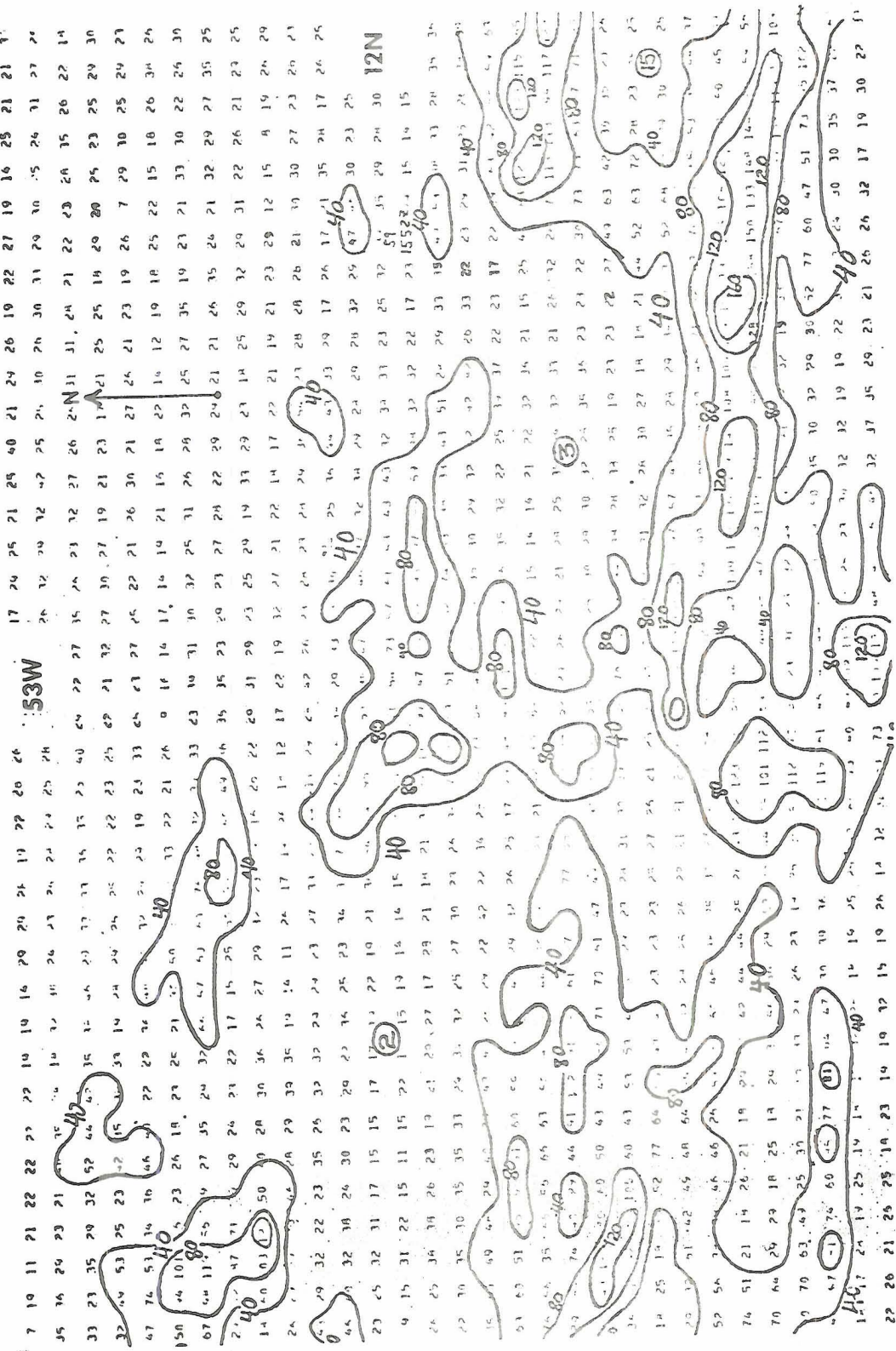


Figure 7 July 18, 1969 1431Z ATS. III Digitized Cloud Picture, Portion of South BOMEX Ring Study Grid, Showing Cloud Ring Structures.

are again utilized. Figure 8 displays the 1431Z range printout cloud picture in the South Grid ring occurrence region, along with the digital range-symbol relationship. Comparing Figure 8 with Figures 7 and 2 shows that the cloud and clear regions are very similarly represented by all three methods. It is the range printouts that are generally used in the specific study of cloud rings outlined in this paper. However, in order to obtain accurate results from the use of the ATS III digital and subsequent range data, several factors relating to the representativeness of the data over various areas and periods of time must be considered. These considerations are necessary because space and time comparisons form the basis of this and similar studies. The first factor is the matter of the MSSC satellite and ground receiving system variable voltage gain settings. This factor leads to multiple (a given) output voltage(s) and related digital value(s) representing a given (multiple) reflected energy value(s) or brightness(es). Thus an ambiguity arises as to the true brightness being measured. The second factor leading to brightness ambiguity relates to reflected energy being a function of the relative positions of the sun, reflective element and satellite. Time of day, cloud or other element earth position and satellite position with respect to earth define this sun-object-satellite geometry. In order to legitimately compare the ATS III pictures covering space and time, a "normalization" procedure is used to relate all picture data to a common voltage gain state and common set of space-time coordinates. After this is done the desired "normalized" pictures are comparable and differences in digital brightness values are due only to reflective element differences themselves,

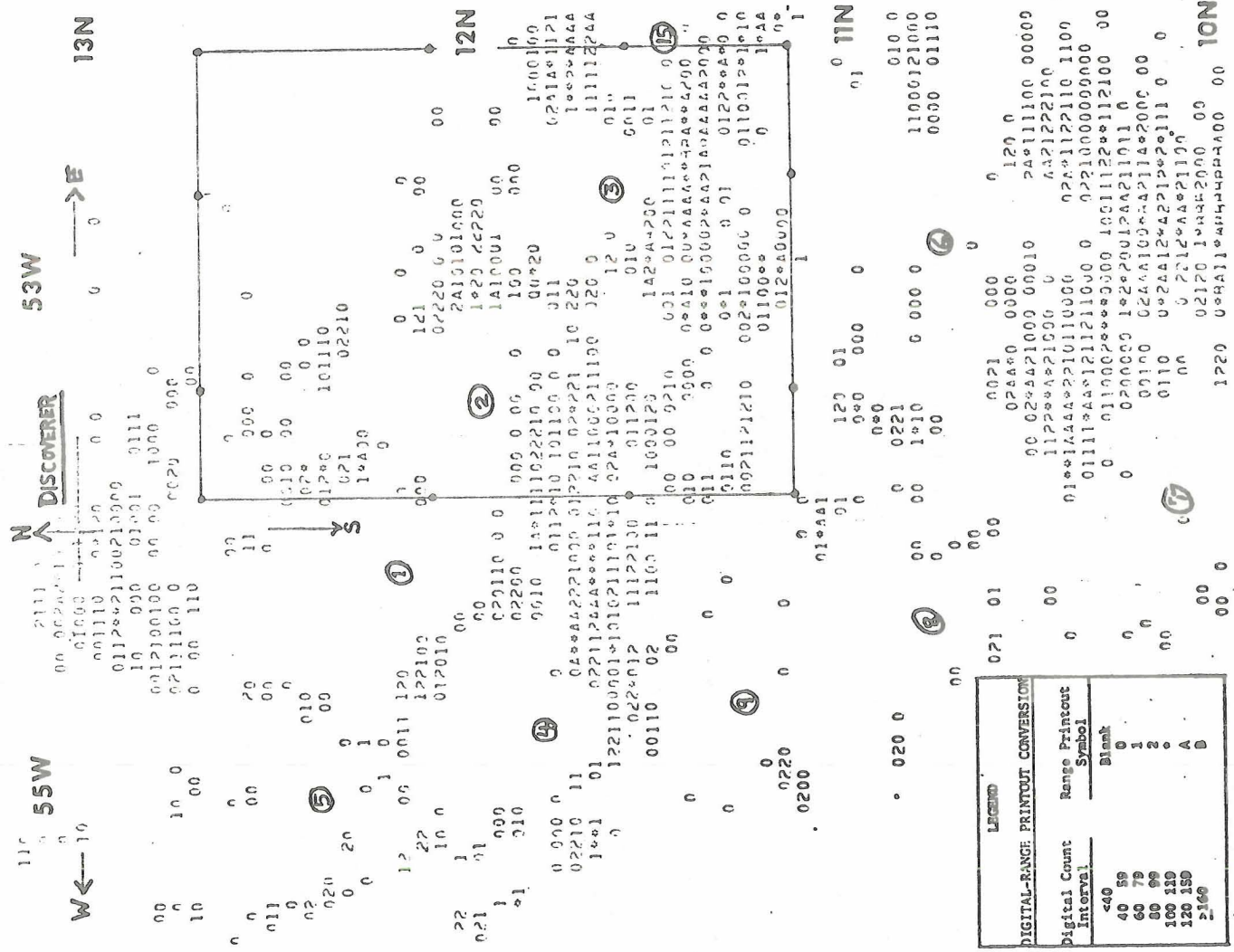


Figure 8 July 18, 1969 1431Z ATS III Range Printout Cloud Picture, Portion of South BOMEX Ring Study Grid, Showing Cloud Ring Structures and Figure 7 Area Outline.

such as cloud thickness, droplet size distribution, etc. The normalization procedure is discussed in detail in Appendix A, Part II.

On July 18 the ATS III pictures were obtained in a common voltage gain state and thus there is no need for normalization with regard to that factor. The results of the geometry normalization calculations for July 18 in the BOMEX area and the 1247Z, 1431Z and 1818Z picture times under consideration are that for the clouds the normalization factors ranged from very nearly 1.00 to 1.10 and for the ocean from 0.7 to 1.0. Thus the normalization does not significantly affect the cloud patterns at the times of consideration and it is the clouds that are the concern here. Thus the pictures are considered to be comparable as is. However, in later studies at more diverse times and places the normalization factors will likely be significant and the corrections will have to be made.

The "normalized" July 18 ATS digital data in their range printout form are used to obtain measurements of: (a) ring cloud diameters and cloud wall dimensions; (b) durations; and (c) motion.

2.1.1.1 Dimensions

The diameter size parameter is important in theoretical considerations of open cell convection through the diameter-height ratio which will be discussed in a later section. Thirteen rings present in the South Ring Grid area at both the 1247Z and 1431Z ATS III picture times are considered to obtain E-W, N-S, and composite mean ring inside diameters for the two times. Inside diameter measurements are made

from the latitude-longitude gridded ATS III range printout cloud pictures, considering the <40 digital values (blank area) as the cloud ring clear center area bounded by the cloud wall (digital values ≥ 40). The mean cloud ring diameter results are presented in Table 1.

TABLE 1

CLOUD RING SIZE

BOMEX PHASE IV, July 18, 1969, SOUTH RING GRID

Inside Diameter-Kilometers

TIME	NO. OF RINGS	N-S MEAN INSIDE DIA.	E-W MEAN INSIDE DIA.	MEAN INSIDE DIAMETER
1247Z	13	57 km	102 km	80 km
1431Z	13	59 km	98 km	79 km

The table shows that the rings are elongated in the east-west direction (with an E-W to N-S ratio of ~ 1.7), more or less along the mean wind direction as will be seen later. It is noted that the sizes change very little over the 104 minute interval between pictures. The individual composite mean ring diameters range from 55 km to 115 km, both of these occurring at 1247Z. Also from the range printouts a range of 9 km to 19 km is found for the widths of the ring cloud walls.

2.1.1.2 Duration

Duration of the July 18 ring patterns is obtained from observation of the large number of rings forming the "honeycomb" system in the

eastern portion of the South Ring Grid south of the fixed ship Discoverer. Some of these rings are shown in Figure 8; this pattern appears in the days' earliest ATS picture at ~1100Z and is present continuously until the picture data gap begins at ~1500Z. In the next picture at 1818Z only one ring remains. But utilizing the Discoverer weather radar pictures and ESSA 7 satellite photographs for ~1700Z reveals that the pattern is still present in many details. Thus the observed lifetime of the major ring system on July 18 is considered to be 6 hours. The other rings in the South Grid and the two in the North Grid have lifetimes shorter than this in general, ~1 to 3 hours, or they move out of the grid and are not considered further.

2.1.1.3 Motion

The next effort in connection with the physical description of the BOMEX July 18 rings using the ATS data is to determine the mean motion of the rings over a period of time. It is desired to utilize rings that persist and that can be correlated well across the time interval chosen. A time interval is desired which is long enough to allow significant motion of the rings, but not so long that the patterns will disappear or be affected by considerable variance in wind fields due to long time span of the motion. This ring motion determination is made in connection with the desire to correlate that motion with vertical means of the horizontal wind field vertical profiles obtained from fixed ship rawinsonde wind soundings. The cloud base to cloud top mean wind of ~10 m/sec from ~100 degrees in the ring motion computation area and its correlation with the mean ring motion will be discussed in detail later.

The 1247Z to 1431Z interval, utilizing the South Ring Grid ATS III data from the range printouts and "honeycomb" ring pattern between Mt. Mitchell and Discoverer, provides the desired type of ring structures. The remaining rings are not considered due to their short-lived nature and/or the questionable Rainier upper level wind data. Eight rings in the South Grid ring pattern are used in computing the 1247Z to 1431Z period mean ring motion. Ring displacements, from which are calculated the speeds and directions (from which rings are moving), are obtained from superimposition of the 1247Z and 1431Z gridded range printout cloud pictures. The resulting 8-ring mean ring cloud motion is 10.5 m/sec from 101° . Individual rings show variations of ± 2.5 m/sec and $\pm 20^{\circ}$ from the mean.

A final but important recent observation using ATS III data is that of the definite though short-lived existence of ring cloud patterns over land, specifically in the tropical Amazon River Basin region on September 8, 1972. These rings are observed in the ATS III picture sequence film loop for this day and display lifetimes of up to approximately 2 hours. The occurrence of cloud rings over land surfaces evokes considerable speculation and opens up a wider field of study related to open cell convection in the tropics.

2.1.2 Weather Radar

Two weather radars, one located on the island of Barbados and the other on the fixed ship Discoverer, were in operation during BOMEX. Only the latter's Selenia METEOR 200 RMT-2S 3.2cm X-band radar data are

utilized in this ring cloud study. Two important pieces of information are obtained from analysis of this data. The first is that the nighttime existence of cloud ring structures is established for the first time, not previously ascertained from ATS satellite cloud observations due to the daytime visible spectrum nature of the data. From 0200Z to 0600Z on July 18 ring patterns were present and persisted in the vicinity of Discoverer. The second result is an estimate of the height of cloud ring elements.

The important aspect of cloud droplet size distribution is taken into consideration here in order to determine whether it is cloud ($<100\mu\text{m}$) or "hard core" precipitation ($>100\mu\text{m}$) droplet echoes that are being observed by the Discoverer 3.2cm radar. USAF Air Weather Service Technical Report 184 dealing with weather radars states that 3cm radars are preferentially "seeing" $\approx 100\mu\text{m}$ size droplets. Results of a wintertime Caribbean area cumulus cloud survey (Braham, Jr. et al., 1957) show that $70\mu\text{m}$ droplets have a number density of $10^5/\text{m}^3$. A further consideration is that the summertime enhanced convective clouds likely possess a greater number of larger droplets compared to wintertime clouds and from the Braham Jr. survey of summertime central US cumulus clouds it is found that developed cumulus congestus are composed of droplets 50% larger than those making up the smaller fair weather cumulus humilus. BOMEX ring cloud heights, to be discussed shortly, are found to be considerably greater than those of the Caribbean cumulus surveyed by Braham, Jr.

Considering all the above it appears likely that the Discoverer radar echoes are largely those from clouds and not solely "hardcore"

precipitation echoes. Tropical cloud heights determined by the 3.2cm radar would be somewhat (not excessively) low with respect to its droplet detection characteristics. Discussion of this and other factors affecting the validity of the radar-determined cloud heights follows. In regard to precipitation BOMEX RFF aircraft cloud film data reveal that on July 18 showers occurred in the cloud ring region only after 1700Z. The radar data analyzed here are those previous to 1700Z. However, it must be remembered that larger droplets are retained within a convective cloud by the updrafts.

2.1.2.1 Cloud Height

The major use of the Discoverer weather radar data is for estimating the heights of the cloud elements making up the ring structures. This determination provides the other value in the theoretically important ring cloud pattern diameter-height ratio mentioned earlier. During the weather observation phase the radar operated in two modes (De La Moriniere, 1972). Radar echo data obtained in the "normal gain-elevation step sequence" mode are used in this study to calculate ring cloud heights. These follow from the PPI (Plan Position Indicator) scan echo disappearance elevation (radar antenna elevation is stepped up 1° every other 12-second revolution) and echo element horizontal distance from the radar site (obtained from the PPI scope with reference to the 50 nm increment range circles). Figure 9 displays the July 18, 1969 1433Z PPI scan radarscope picture which shows a portion of the ring system south and southwest of Discoverer. A cloud-earth curvature-radar site geometry was derived and a computer computation performed,

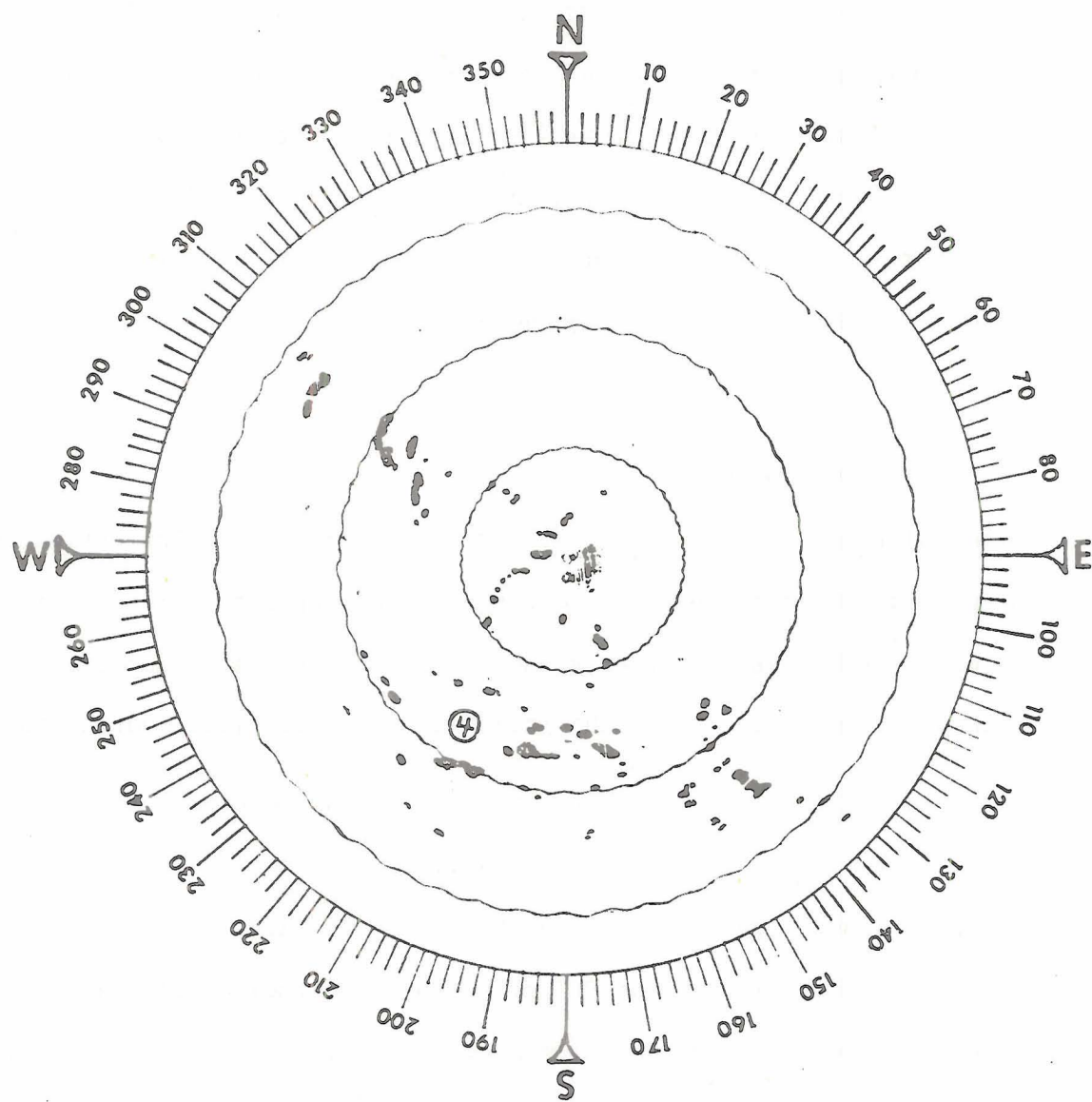


Figure 9 BOMEX July 18 1433Z Discoverer Weather Radar PPI Scope Cloud Echo Picture at 0° Antenna Elevation and Normal Gain (Horizontal Range Circles at 50 nm Intervals).

yielding apparent cloud heights above the cloud's local earth surface subpoint in terms of 1° increment cloud top echo disappearance (beam center) elevations and 5nm increment horizontal distances. The earth-curvature-corrected apparent cloud height equation, whose derivation and the radar observation geometry are discussed in detail in Appendix B, Part I, is:

$$h = \frac{\overline{OF}^2}{2R_E} + \overline{OF} \tan \beta \quad [2-2]$$

where h is the cloud height, \overline{OF} is the horizontal distance of the cloud element from the radar site, β is the echo disappearance elevation, and R_E is the earth's radius, 6370km. Also since the antenna elevation steps are 1° , there is a subjective estimate of the cloud echo disappearance elevation for echo disappearance between steps, leading to an echo disappearance elevation uncertainty on the order of 0.5° .

The apparent cloud heights are a quite valid representation of cloud top locations with consideration of the implicit assumption that cloud top is located at radar beam center. But since the radar does not possess a pencil beam but one which displays a spread with distance, the cloud tops lie below the beam center and the apparent heights are too high. This beam spread aspect also leads to an apparent increase in cloud height with distance for a large random sample of clouds. The apparent heights must be corrected in this respect to yield in part "true" cloud heights. It is noted that no "true" cloud height can lie below the radar horizon (0° antenna elevation with related increasing height of horizon above surface with horizontal distance) except if

beam curvature or other variables are present. There is thus a minimum cloud height visible at a given horizontal distance, which height increases with that distance.

In addition to the Discoverer radar cloud height corrections for (a) beam spread which leads to an overestimate of cloud height and (b) earth curvature (taken into account in Equation |2-2|) which leads to underestimate, corrections for the effects of (c) cloud droplet size distribution leading to height underestimate, (d) beam curvature, due either to atmospheric refraction resulting from water vapor gradients or to bounce from temperature inversions, leading to height underestimate or overestimate correlated with the occurrence of skyward or earthward curvature, respectively, and (e) beam side lobes which lead to height overestimate must be considered in order to obtain accurate cloud heights. The latter effect is considered negligible due to (1) the relation between the relatively low cloud reflectivity over tropical oceans and the low power of the side lobe emissions and (2) the $\sim 3^\circ$ angle between beam center and side lobe emissions implying that this effect is only of concern for antenna elevations $> \sim 3^\circ$ (Ruprecht, personal communication), which elevations are few for clouds observed on July 18. With regard to the beam curvature effect (d) it is considered that the observed presence of an inversion and drying aloft in the Discoverer area on July 18 leads to earthward beam curvature and thus an overestimate of cloud heights. Therefore effects (c) and (d) and the corrections for them will tend to cancel one another and are assumed to do so here.

For the July 18 1303Z and 1433Z Discoverer weather radar elevation

sequence observations, the anomalous increase in cloud heights with distance from the ship (mainly due to the beam spread effect (a)) is observed and cloud height corrections (considering the minimum visible cloud height aspect) are determined. These are applied to the apparent heights through a modification of the original cloud height computer program, yielding estimated cloud heights (again given in terms of cloud echo disappearance elevation and horizontal distance) which are considered an upper bound, due to the minimum nature of the corrections. The anomalous cloud height increase and cloud height correction procedure are discussed in detail in Appendix B, Part II.

To obtain an idea of the July 18 estimated upper bound ring cloud heights for the period of the mean ring motion and mean wind determinations, the well-defined ring #4 is chosen from the South Grid ring region (Figure 8) where the mean ring motion was obtained, which ring is observed on both the 1303Z and 1433Z (Figure 9) cloud radar pictures. In correlation with this choice, a visual comparison of the 1303Z and 1433Z radar cloud ring pictures with the 1247Z and 1431Z ATS III cloud ring pictures, respectively, is made and a good correlation of cloud elements and locations for the given times is found to exist there. The estimated mean upper bound ring cloud height for Ring #4 at 1303Z is 7400m, at 1433Z is 6800m and is an average over the 1303Z to 1433Z interval of 7100m, with individual cloud heights ranging from 5000 to 11,000m, this latter likely being a large cumulonimbus. The echo disappearance elevation uncertainty of $\pm 0.5^\circ$ yields uncertainty in the mean cloud height of $\pm 1300m$, based on an $\sim 3^\circ$ average echo disappearance elevation at a mean ring cloud element horizontal distance of $\sim 80nm$. The true mean ring cloud heights are estimated to be $\sim 6km$, i.e., they

are estimated to be lower than the upper bound heights by an amount equal to the 0.5° uncertainty or ~1km. Although these results are based on one particular ring, there is no reason to believe that it is not quite representative of all rings in the near area during the period.

The qualitative 5-6 km mean maximum cloud height finding from the RFF 39C aircraft photographic data (to be discussed in the following section) is seen to be somewhat in agreement with the radar-estimated cloud heights, keeping in mind the distance from aircraft and upper bound height aspects, respectively, connected with these height determinations. The mean ring motion-wind profile correlation findings and thermodynamic sounding data to follow tend to support the validity of the cloud heights estimated from the radar and aircraft observations. The cloud height measurement made in the present study was not previously available for tropical rings and shows that these rings, in contrast to those in the subtropics as will be seen later, are composed of deep convective clouds.

A method of cloud height determination, based on the above discussed corrected radar cloud heights program and ATS III digital data brightness values, was devised by Reynolds and Vonder Haar (1973). They coincidentally chose July 18, 1969 and the Ring #4 region of the BOMEX area during the 1300Z to 1500Z period for their analysis. Utilizing the nearly simultaneous Discoverer radar and ATS III observations in the above time period, a relationship between cloud height and cloud brightness represented by digital data values was derived. To accomplish this, corresponding cloud elements were located on the nearly simultaneous radar echo and contoured ATS digitized pictures, the estimated heights of

these elements were determined in the manner discussed previously in this section, and the digital values representative of the brightness of these elements were obtained from the digitized satellite picture. A graphical plot of cloud height versus digital brightness value was made and the result is that cloud brightness (digital value) increases more or less linearly with cloud height. Thus it appears that higher (thicker) clouds are also brighter clouds. For the cloud elements of Ring #4 the Reynolds and Vonder Haar method yields a mean upper bound cloud height of 5.3km compared to the 7km mean height found in this study. Since there is inherent in the above cloud height determination methods an uncertainty in the interpretation of the cloud echo disappearance elevation due to the 1° -step nature of the radar antenna elevation during the PPI scans, the above difference in Ring #4 cloud height is likely the result of a lower estimate of echo disappearance elevation by Reynolds and Vonder Haar with consequent lower cloud heights. It should be noted that both of the above cloud height methods are subject to variations in ATS III camera system voltage gains and/or radar beam power and receiver gain reduction. Also of note is that there is inherent ambiguity in the cloud heights determined by the Reynolds and Vonder Haar "cumuliform" method when the clouds under consideration are thin cirrus, thick altostratus, and such layers.

2.1.3. Aircraft Cloud Photography and Meteorological Observations

These data fall into two categories: (a) supporting; and (b) non-supporting, in regard to their providing or not providing additional knowledge of the cloud ring systems occurring in the BOMEX area on July 18, 1969.

2.1.3.1. Supporting

NOAA RFF DC-6 aircraft cloud film data provide information in the form of approximate cloud height ranges. RFF flight altitudes on July 18 ranged from ~100 m above the sea surface to ~5.4 km. Cloud photo data from the 39C flight at the latter stated altitude in the general vicinity of the ring cloud pattern show cloud tops generally at or below the aircraft flight altitude, using the aircraft horizontal delineated by the wings as a reference. These findings provide only an approximate idea of cloud heights (distance from the aircraft changes the height estimates significantly), but these heights agree generally with those determined from Discoverer weather radar data as discussed previously and with those heights inferred from the fixed ship rawinsonde temperature and moisture soundings and vertical mean upper level winds to be discussed shortly. The RFF photographic data also show that precipitation (showers) occurred in the South Grid cloud ring region only after ~1700Z which is the approximate time that the multiple ring pattern began to disappear.

2.1.3.2 Non-Supporting

The RFF and other BOMEX support aircraft flights also provide temperature and moisture observation data in the general region of the BOMEX July 18 cloud ring structures. These data are available at various heights above surface in relation to the various flight altitudes. However, the flights on July 18 were at altitudes considerably above and/or locations outside the cloud rings themselves and the flight speeds were relatively high and/or the data resolution relatively low, yielding no useful quantitative thermodynamic data on the scale on the cloud ring structures. Aircraft wind field data at various heights are also available for selected flights, but again the observations were made above and/or outside the specific ring structures. Quantitative thermodynamic and dynamic data are most usefully available from the fixed ship rawinsonde soundings which are discussed in Section 2.2 to follow. The aircraft data are seen to be of a qualitative nature for the most part.

2.1.4 Summary

In Summary, the BOMEX July 18 cloud ring structure physical description is as follows: The rings are like doughnuts, consisting of growing and decaying cumulus cloud wall elements and clear center areas; they are somewhat elongated along the mean wind direction over their depth; they occur singly or in a honeycomb type multiple pattern; they have a mean diameter of 80 km, a mean cloud wall width of 15 km, and a mean height of ~6 km; the honeycomb pattern cloud rings have a lifetime

of 6 hours, while the single rings last for only 1 to 3 hours; they travel very nearly with the mean wind over their depth, from 100° at 10.5 m/sec; precipitation appears to be confined to deeply developed ring cloud elements; cloud ring structures are observed during both the daytime and nighttime hours.

2.2 Cloud Ring Thermodynamic Description

Another major aspect of the ring cloud study is that of the synoptic scale thermodynamics of the ring and non-ring regions with comparison and contrast of these areas. Temperature and moisture are parameters important in stability and energy considerations. The rawinsonde temperature and moisture (specific humidity) soundings at the five fixed ship stations (Fig. 3) for 1200Z, 1500Z and 1800Z on July 18 are utilized. Nimbus 3 SIRS-A radiation inversion temperature soundings for July 18 are also used to extend temperature data above the usual BOMEX fixed ship 300 mb sounding limit. Surface and sea surface temperature observations at the fixed ships provide knowledge of surface layer stability and heat fluxes.

Temperature (T) and specific humidity (q) information are extracted from the published BOMEX 5-second-interval data at either ~20 mb intervals or significant levels such as inversions and dry layers. This method averages out small variations on the order of 10 mb. Erratic temperature and relative humidity data (from which are calculated the specific humidity values) are eliminated and the sounding at that point smoothed. Temperature and moisture sensor lags due to the rising balloon are considered small and are neglected, being present in all the soundings and

of small consequence in this study which deals with relative differences in meteorological parameters over various regions and periods of time.

There are two important aspects to note in regard to the BOMEX meteorological data utilized in the investigation of the July 18, 1969 ring cloud patterns. These aspects apply not only to the temperature and moisture discussions to follow immediately, but to all BOMEX thermodynamic and dynamic data and related parameter discussions. First, from Fig. 3 it is seen that the five fixed ship and Barbados stations form a meteorological observation network with a grid point spacing of 200 to 250 km, while from earlier discussion the ring cloud diameter size is found to be on the order of 60 to 80 km. The observing network and its data are on a scale three to four times that of the ring clouds and thus the data obtained on the larger grid scale and utilized in the BOMEX ring cloud investigation, as well as any findings and derivations therefrom, are synoptic in nature (at the lower end of the synoptic scale to be correct). There is only one known instance of data being obtained within a ring cloud structure itself (Ruprecht et al., 1973) and this event will be discussed in detail later in the Data Comparisons section.

The second important aspect of the BOMEX data utilized here, specifically the rawinsonde sounding temperature, moisture and wind data, is that these data are in the uncorrected A_0 form (De La Moriniere, 1972). No analysis of these data has been made which would lead to elimination of the erratic and bad data, due to instrument and other errors, which was discussed above. To make the data usable the irregularities have to be smoothed out and this is done as has been or will be described in this paper. However, at present the A_0 data are

being converted to the corrected A form (Holland and Rasmusson, 1973) by BOMEX data analysis, utilizing knowledge gained about the nature of the observations and instrumentation, and these corrected data should be available in the near future. Preliminary results of the correction process are that the major portion of the A_o data is good, lending validity to the ring-cloud investigation findings in this study.

2.2.1 Temperature

Fig. 10 displays typical BOMEX area near-ring and non-ring region temperature and moisture soundings for July 18. In this and subsequent figures delineation is made of data obtained within and/or representative of the ring occurrence area itself (Ring), of data obtained in or representative of ring occurrence boundary regions (Near-Ring) and of data obtained in or representative of regions away from ring occurrence (Non-Ring). The 15Z Discoverer sounding is representative of the near-ring region on July 18, while the 15Z Oceanographer and 18Z Rainier soundings are typical of the non-ring regions south and north of the South Grid honeycomb ring pattern. The Nimbus III SIRS-A temperature soundings for July 18 are also shown. As can be seen from Figure 3 these soundings were made by the satellite on its pass from south to north across the BOMEX area at just before 1500Z. Also soundings number 64 and 66 are seen to be located very near to Oceanographer and Discoverer respectively. Thus these two soundings are entered on Fig. 10 as high level extensions of the 15Z Oceanographer and Discoverer rawinsonde sounding data which terminate at around 300 mb. The SIRS-A temperature data are available from 1000 mb to

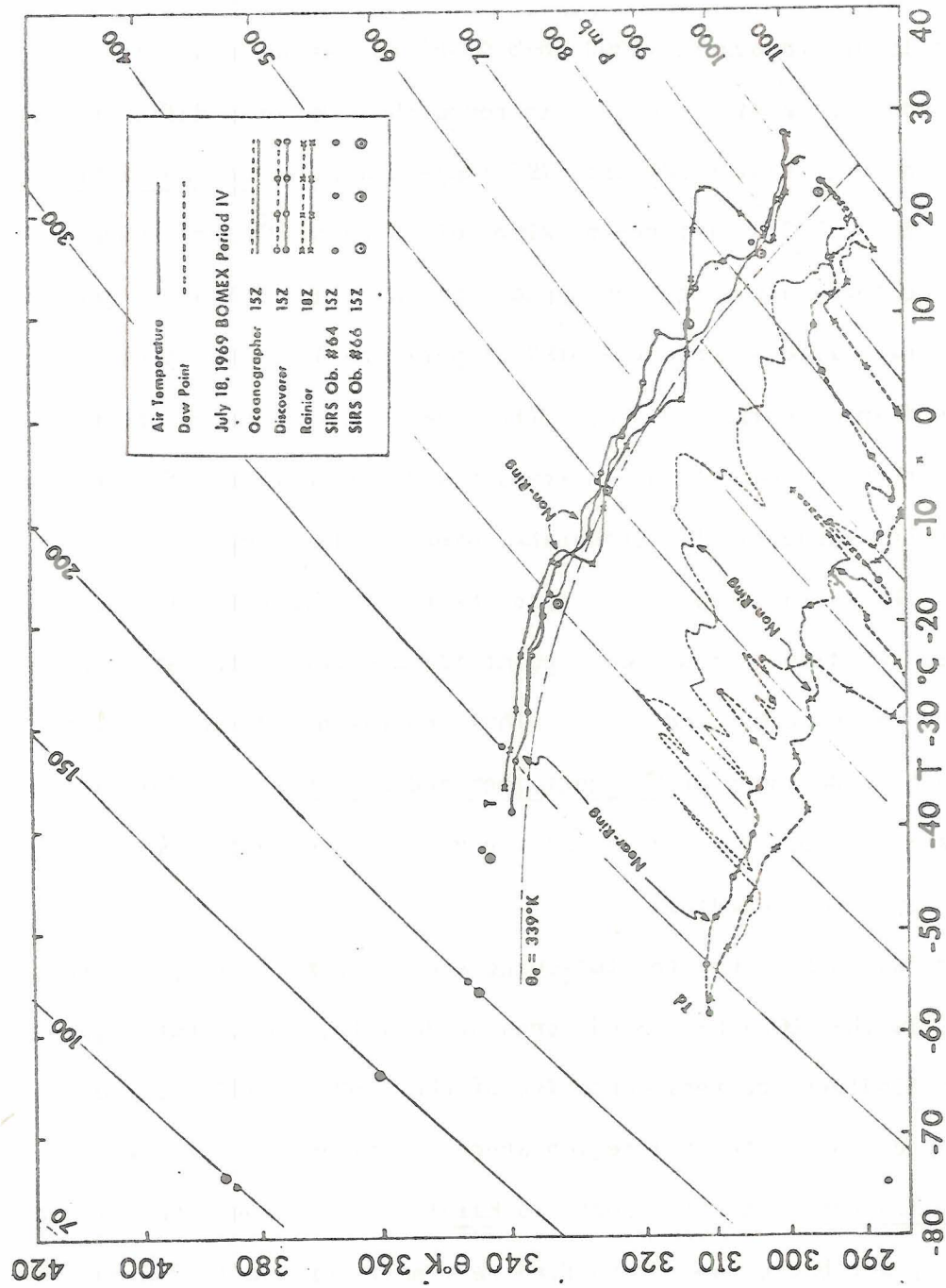


Figure 10 BOMEX July 18 Fixed Ship Rawinsonde Temperature and Dew Point Soundings and Nimbus III SIRS-A Radiation Inversion Temperature Soundings.

1 mb at standard upper air pressure levels by inversion of the infrared radiative transfer equation using the infrared radiation measurements made by the Satellite InfraRed Spectrometer (SIRS) radiation sensor. In comparing the lower atmosphere (1000 mb \rightarrow 300 mb) rawinsonde and satellite temperature soundings in Figure 10, it is found that the mean difference between common level rawinsonde and SIRS temperatures at Oceanographer and Discoverer is $+0.7^{\circ}\text{C}$. Difference values of up to $+4.0^{\circ}\text{C}$ are found at levels where there are large and rapid vertical fluctuations of temperature. The high levels where the SIRS temperature data are being considered here display small ($\sim 0.5^{\circ}\text{C}$) differences. A last point about SIRS-A data is that the output of the instrument and information inferred from it are results automatically integrated over the 11.5 degrees field of view (200 + km earth surface spot size) by the instrument. The SIRS-A temperature sounding is thus not a point measurement of the atmosphere, whereas the rawinsonde sounding is. Thus the rawinsonde-satellite temperature data comparisons at Oceanographer and Discoverer on July 18 are area comparisons, but very valid ones in view of the space-time closeness of the two types of soundings.

Referring to Fig. 10, the following are the general temperature conditions in the BOMEX Ring Study area on July 18, 1969. Note again that these findings are representative of the 1200Z to 1800Z period. In the portion of the South Grid region where the rings are numerous (Mt. Mitchell-Discoverer) and also north to Rainier, the T soundings display a marked dry adiabatic lapse rate from very near surface (~1015 mb) to around 920 mb. In the non-ring region to the south (Oceanographer) this adiabatic lapse rate is not present. In the ring-rich portion of the South Grid there is also present one or several relatively stable layers

of generally isothermal or even inversion lapse rate occurring at various levels between 600 and 800 mb and being up to 50 mb thick. South of this area the stable layer phenomenon appears periodically. In general the term "stable" as used in the discussions in this paper refers to any atmospheric temperature lapse rate which is less than the moist adiabatic through isothermal and inversion. At the northernmost station Rainier there is a very pronounced dry adiabatic lapse rate layer ($\theta \approx 313^{\circ}\text{K}$) around 600 mb to 700 mb being approximately 150 mb thick bounded above and below by inversions. The dry adiabatic layer is rather well mixed as exemplified by a rather uniform moisture distribution. This air mass is likely of the "Saharan" variety which has a 313K potential temperature mean and is a well mixed air mass. It is known to travel westward from Africa embedded in the tropical easterly flow and is usually readily identified by the dust or haze phenomena associated with it, as described in the literature (Prospero and Carlson, 1971). The dust phenomenon is noted in July 18, 1969 aircraft turbidity measurements in the vicinity of the Rainier. From the SIRS-A T-data plots it is seen that the lapse rate is generally moist adiabatic up to 200 mb or so, then more stable up to the ~90 mb tropopause where it becomes an inversion lapse prevailing into the stratosphere. Very little difference is seen between the ring and non-ring regions in the higher atmosphere above 300 mb. Except for the variations described above the temperature lapse rates are generally slightly greater than moist adiabatic from the lower troposphere up to 200 mb, the normal condition in a tropical atmosphere.

Surface (~10 meter level) air and sea surface temperature observations at the fixed ships are used to define the air-sea surface temperature difference and thus surface layer stability and heat flux conditions

in the BOMEX Ring Study area on July 18. These temperature data are obtained from the BOMEX Ship Station Surface Observations (1969). The results are that at Oceanographer and Mt. Mitchell the July 18 air-sea temperature differences are -1.8°C and -1.1°C , respectively (air colder than sea surface), while from Discoverer north they are effectively zero. Thus in the ring-rich Mt. Mitchell region and south to Oceanographer the heat flux is notably from sea to air and the surface layer is somewhat unstable with respect to this flux, while from Discoverer north there is very little heat flux and the surface layer is isothermally stable with regard to that situation. In regard to the north-south sea temperature variation over the ring grids, the data show that this difference is about 1°C ; air temperatures display a significantly larger N-S variation than this and account for the major portion of the N-S air-sea surface temperature difference variation. Therefore the concern is with the air-sea temperature difference rather than with the very small latitudinal variations in T_{sea} in regard to ring occurrence on July 18. It is also of importance to remember that in the tropics the horizontal gradients of temperature, pressure and moisture are generally relatively small, with moisture displaying the greatest time-space variations of the three parameters. Numerous references display and/or discuss these aspects of the tropics, among them Madden et al. (1971), Oort and Rasmusson (1971) and Atkinson (1971).

2.2.2 Moisture

Reference again to Fig. 10 provides information on the July 18 12Z to 18Z upper air moisture conditions in the BOMEX Ring Study area. In

the South Grid ring-rich area there is a sharply defined dry layer beginning at the isothermal or inversion temperature lapse point with rapid drying above. To the south at Oceanographer there is a same form but minor drying accompanying the periodic inversion occurrences. To the north at Rainier there is marked drying accompanying the inversion below the "Saharan" dry adiabatic layer, with the earlier stated generally well mixed moisture condition prevalent in the latter layer. Also notable is the general moistness of the Oceanographer and Rockaway soundings in the 12Z to 18Z period compared to the other ship areas. Further this moistness is rather uniform vertically at Oceanographer, but shows a bimodal moist layer pattern, near surface and ~500 mb, at Rockaway with a drier layer between at ~700 mb accompanying the temperature inversion. The moistness at Oceanographer is likely the result of location near the Intertropical Convergence Zone (ITCZ), while that at Rockaway is due to the presence of the easterly wave cloud "tail" (Fig. 2) at or near the station, with the clouds related to the middle troposphere moisture maximum.

2.2.3 General T-q Findings

Several results are obtained by consideration of the rawinsonde temperature and moisture sounding data together. The first is the approximate height of the cloud bases in the ring study area. Assuming parcel ascent and calculating the Lifting Condensation Level (LCL) graphically, the result is a mean theoretical cloud base in the ring area of ~915 mb or 900 meters above surface. There is little variation

of this over the region. Theoretical cloud base obtained from calculation of the Convective Condensation Level (CCL) agrees well with that found using the LCL method. These cloud base heights are in good agreement with those observed in tropical ocean regions.

Another result from the T-q combinations observed on July 18 is the correlation of these data with the estimated mean ring cloud height of ~6 km found from the Discoverer weather radar data. With the occurrence of the middle level stable and dry layer in the Discoverer-Mt. Mitchell area, the buildup of convective clouds much above this level is unlikely due to the stability there and cloud liquid water evaporation and detrainment from relatively slow-growing tropical clouds penetrating into the dry layer. Therefore the 600 mb to 700 mb level stable, dry layer likely limits the ring clouds to ~500 mb (~6 km) such that these clouds are confined in general to the lower half of the troposphere by this "lid" phenomenon.

The existence of the stable layer(s) with marked drying at lower middle tropospheric levels can be reasonably explained by the presence of a synoptic scale subsidence at and above these levels over the ring study area north of Mt. Mitchell on July 18. Referring back to Figs. 4 through 6 it is noted, as was mentioned in the Introduction, that this area is under the influence of a surface synoptic high pressure and easterly flow ridge system and this meteorological situation is characterized by subsidence in general. The ring areas are somewhat south of the anticyclonic center and thus the magnitude and depth of the subsidence there would be expected to be somewhat less than that further north, the subsidence to the south likely occurring more generally aloft with some convergence near the surface. This agrees with the thermodynamic

findings and further the divergence and relative vorticity dynamic results presented in the next section tend to verify this occurrence. Thus with this subsident flow occurring there is present a mechanism for maintaining the stable layer with drying and thereby limiting convective cloud growth to heights not exceedingly greater than the stable layer height. Also these stable and dry layers are likely parts of the normal trade wind inversion occurrence resulting from the general subtropical high pressure (STHP) subsidence climatologically present north of the ring areas at 25N to 30N in July (Oort and Rasmusson, 1971).

Two points of interest which should be kept in mind when considering the general T-q results presented here are the disappearance of the South Grid honeycomb ring pattern between 15Z and 18Z on July 18 and the presence, though short-lived, of two rings in the North Grid. The results presented are those generally representative of the areas and time period stated, but there are obviously some changes occurring causing the ring pattern disappearance or short duration of rings. These aspects also bring up the point that there are obviously necessary and sufficient conditions for ring formation and that the presence of a single parameter is not grounds for forecasting ring occurrence, as the T-q results show.

2.2.4 Summary

In Summary, the BOMEX July 18 cloud ring structure synoptic scale thermodynamic description is as follows: In the South Grid ring occurrence area the near surface layer is moist and nearly dry adiabatically

unstable, while at the middle or lower middle levels (600 mb \rightarrow 800 mb) a relatively stable lapse rate layer is present with considerable drying at and above the stable layer; except for the above the lapse rate is slightly greater than moist adiabatic to ~200 mb; above 200 mb the lapse rate becomes more stable and the tropopause is located at ~90 mb; there exists a 1°C + excess of sea surface temperature over surface air temperature with corresponding upward heat energy flux from the surface. In the non-ring regions the near surface unstable layer and/or the middle level stable layer are absent; in place of the dry, stable layer the atmosphere is relatively moist; above 300 mb the temperature sounding in the non-ring area does not differ significantly from that in the ring occurrence area; the air-sea surface temperature difference is essentially zero or exhibits a small air temperature excess with consequent downward heat energy flux.

2.3 Cloud Ring Dynamic Description

The third major descriptor of the cloud ring systems and their environment is the synoptic scale wind field, horizontal and vertical, and the associated dynamic properties of divergence and relative vorticity. Due to the large-scale nature of the data grid compared to the rings, it is not possible, with the data available for this study, to present quantitative results of the mass motions in the rings themselves. But in a qualitative way results about cloud ring mass motions are available from visual observation of the resulting pattern. With the evidence of a persistent cloud ring wall and clear center, the obvious

and only physical atmospheric process that can result in such a pattern is ascent in the cloud wall region and subsidence (or at least no rising motion of note) in the center of the ring.

2.3.1 Winds

Most all wind analysis in this study is based on the fixed ship and Barbados rawinsonde data. However, supporting data were obtained from a rather new method of obtaining winds, utilizing computer correlation of cloud displacements from ATS digital data. The rawinsonde wind data are treated in a manner similar to the temperature and moisture data except that the wind data are considered over a longer period of time on July 18. This is due, in part, to the occurrence of many missing wind observations in the 3-hourly rawinsonde flights at Rockaway, but primarily due to the desire to look at the dynamics outside the time span of the numerous ring occurrences. A station with winds missing at a standard observation time in the experiment negates obtaining area-average divergence, vertical motion, and relative vorticity values, due to the method used to obtain these results which will be discussed shortly.

An important point in regard to the general wind analysis should be noted at this time. In pursuing the analysis of wind profiles and cloud motion comparisons, it became evident that Rainier winds at all levels to ~300 mb are westerly and thus considerably in opposition to the easterly flow at Rockaway and south, while all stations are under the influence of the easterly flow on the southern side of the aforementioned surface high pressure system to the north of the ring grids.

Thus the Rainier wind data were dropped from consideration in this study. Also in regard to missing wind data, inferring winds geostrophically from the pressure field is ignored because of the closeness of the BOMEX region to the equator where the geostrophic approximation becomes uncertain.

Wind data (u and v components) are extracted from the rawinsonde soundings at 50 mb intervals or at significant levels from 1000 mb to sounding termination generally occurring around 300 to 400 mb. The considered wind data for the fixed ships excluding Rainier cover the period from 0300Z on July 18 to 0000Z on July 19, while for island station Barbados the period covered is 0600Z on July 18 to 0600Z on July 19.

The first use of the wind data is to compare the mean ring motion in the area between Mt. Mitchell and Discoverer during the period 1247Z to 1431Z on July 18, as discussed earlier, with the mean wind profile in that area during that period. To obtain the mean wind profile, the 12Z and 15Z wind data at Mt. Mitchell and Discoverer at the 1000, 850, 700, 600, 500 and 400 mb levels are utilized. The wind data levels above are chosen for their approximately equal vertical spacing (~1500 m) to avoid the necessity of weighting vertical averages. Utilizing the above data a space-time mean wind at each wind level over the South Grid honeycomb ring pattern occurrence time and region is calculated, along with the vertical means of the space-time individual wind level means between 850 mb and 600, 500 and 400 mb. The Fig. 11 space-time cross section displays the Mt. Mitchell-Discoverer area wind profiles (plotted in conventional symbols) at 12Z and 15Z, along with other available wind profiles at the fixed ship stations during the 12Z to 18Z period, all of which will be discussed further on.

findings and further the divergence and relative vorticity dynamic results presented in the next section tend to verify this occurrence. Thus with this subsident flow occurring there is present a mechanism for maintaining the stable layer with drying and thereby limiting convective cloud growth to heights not exceedingly greater than the stable layer height. Also these stable and dry layers are likely parts of the normal trade wind inversion occurrence resulting from the general subtropical high pressure (STHP) subsidence climatologically present north of the ring areas at 25N to 30N in July (Oort and Rasmusson, 1971).

Two points of interest which should be kept in mind when considering the general T-q results presented here are the disappearance of the South Grid honeycomb ring pattern between 15Z and 18Z on July 18 and the presence, though short-lived, of two rings in the North Grid. The results presented are those generally representative of the areas and time period stated, but there are obviously some changes occurring causing the ring pattern disappearance or short duration of rings. These aspects also bring up the point that there are obviously necessary and sufficient conditions for ring formation and that the presence of a single parameter is not grounds for forecasting ring occurrence, as the T-q results show.

2.2.4 Summary

In Summary, the BOMEX July 18 cloud ring structure synoptic scale thermodynamic description is as follows: In the South Grid ring occurrence area the near surface layer is moist and nearly dry adiabatically

unstable, while at the middle or lower middle levels (600 mb \rightarrow 800 mb) a relatively stable lapse rate layer is present with considerable drying at and above the stable layer; except for the above the lapse rate is slightly greater than moist adiabatic to ~200 mb; above 200 mb the lapse rate becomes more stable and the tropopause is located at ~90 mb; there exists a 1°C + excess of sea surface temperature over surface air temperature with corresponding upward heat energy flux from the surface. In the non-ring regions the near surface unstable layer and/or the middle level stable layer are absent; in place of the dry, stable layer the atmosphere is relatively moist; above 300 mb the temperature sounding in the non-ring area does not differ significantly from that in the ring occurrence area; the air-sea surface temperature difference is essentially zero or exhibits a small air temperature excess with consequent downward heat energy flux.

2.3 Cloud Ring Dynamic Description

The third major descriptor of the cloud ring systems and their environment is the synoptic scale wind field, horizontal and vertical, and the associated dynamic properties of divergence and relative vorticity. Due to the large-scale nature of the data grid compared to the rings, it is not possible, with the data available for this study, to present quantitative results of the mass motions in the rings themselves. But in a qualitative way results about cloud ring mass motions are available from visual observation of the resulting pattern. With the evidence of a persistent cloud ring wall and clear center, the obvious

and only physical atmospheric process that can result in such a pattern is ascent in the cloud wall region and subsidence (or at least no rising motion of note) in the center of the ring.

2.3.1 Winds

Most all wind analysis in this study is based on the fixed ship and Barbados rawinsonde data. However, supporting data were obtained from a rather new method of obtaining winds, utilizing computer correlation of cloud displacements from ATS digital data. The rawinsonde wind data are treated in a manner similar to the temperature and moisture data except that the wind data are considered over a longer period of time on July 18. This is due, in part, to the occurrence of many missing wind observations in the 3-hourly rawinsonde flights at Rockaway, but primarily due to the desire to look at the dynamics outside the time span of the numerous ring occurrences. A station with winds missing at a standard observation time in the experiment negates obtaining area-average divergence, vertical motion, and relative vorticity values, due to the method used to obtain these results which will be discussed shortly.

An important point in regard to the general wind analysis should be noted at this time. In pursuing the analysis of wind profiles and cloud motion comparisons, it became evident that Rainier winds at all levels to ~300 mb are westerly and thus considerably in opposition to the easterly flow at Rockaway and south, while all stations are under the influence of the easterly flow on the southern side of the aforementioned surface high pressure system to the north of the ring grids.

Thus the Rainier wind data were dropped from consideration in this study. Also in regard to missing wind data, inferring winds geostrophically from the pressure field is ignored because of the closeness of the BOMEX region to the equator where the geostrophic approximation becomes uncertain.

Wind data (u and v components) are extracted from the rawinsonde soundings at 50 mb intervals or at significant levels from 1000 mb to sounding termination generally occurring around 300 to 400 mb. The considered wind data for the fixed ships excluding Rainier cover the period from 0300Z on July 18 to 0000Z on July 19, while for island station Barbados the period covered is 0600Z on July 18 to 0600Z on July 19.

The first use of the wind data is to compare the mean ring motion in the area between Mt. Mitchell and Discoverer during the period 1247Z to 1431Z on July 18, as discussed earlier, with the mean wind profile in that area during that period. To obtain the mean wind profile, the 12Z and 15Z wind data at Mt. Mitchell and Discoverer at the 1000, 850, 700, 600, 500 and 400 mb levels are utilized. The wind data levels above are chosen for their approximately equal vertical spacing (~1500 m) to avoid the necessity of weighting vertical averages. Utilizing the above data a space-time mean wind at each wind level over the South Grid honeycomb ring pattern occurrence time and region is calculated, along with the vertical means of the space-time individual wind level means between 850 mb and 600, 500 and 400 mb. The Fig. 11 space-time cross section displays the Mt. Mitchell-Discoverer area wind profiles (plotted in conventional symbols) at 12Z and 15Z, along with other available wind profiles at the fixed ship stations during the 12Z to 18Z period, all of which will be discussed further on.

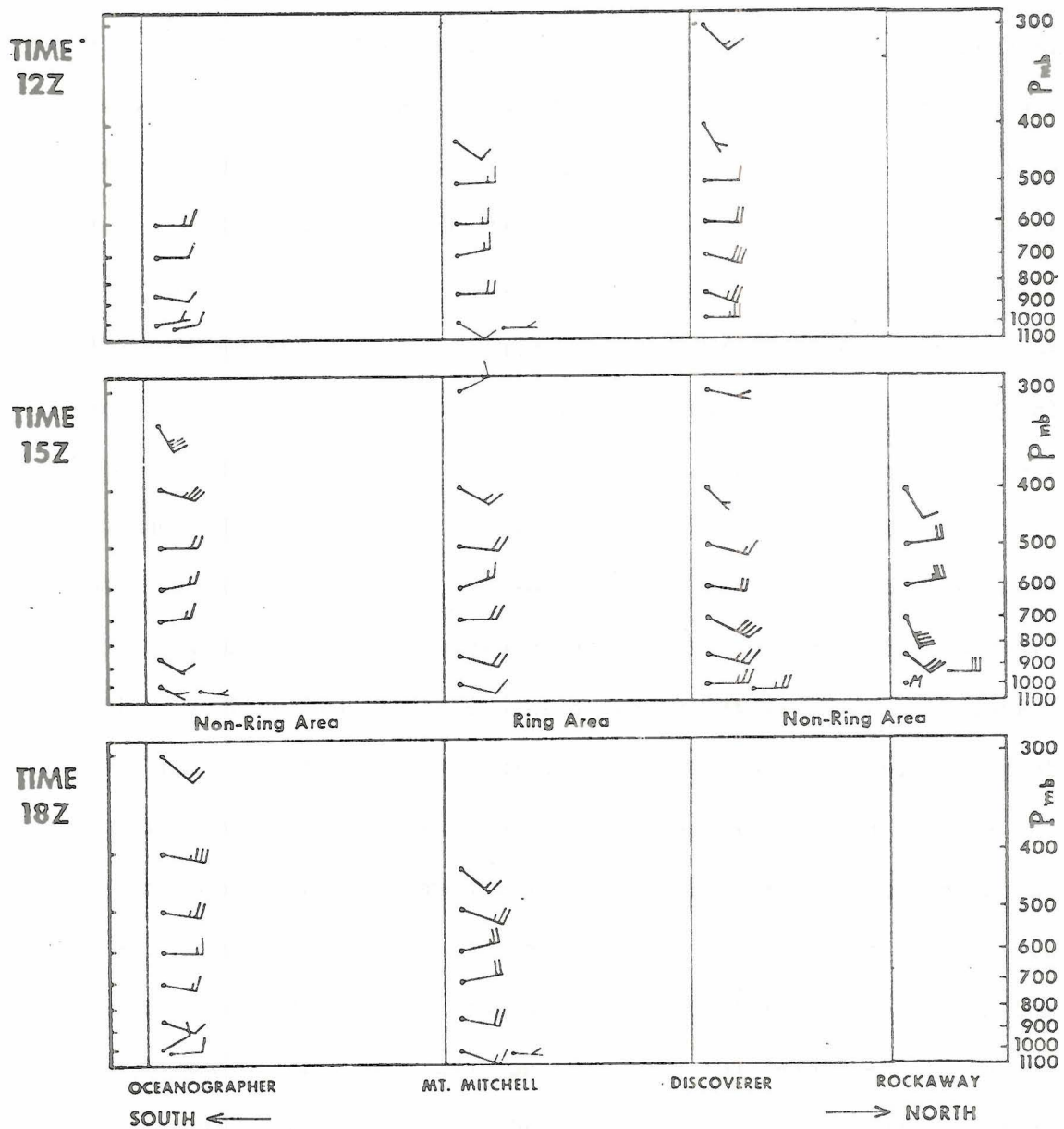


Figure 11 BOMEX July 18 Fixed Ship Wind Field Observations Time - North↔South Space - Height Cross Section Plotted in Conventional Wind Observation Symbols. (Half feather = 5 kts; Full feather = 10 kts).

The results of the averaging procedure are that the mean wind between 850 mb and 400 mb in the ring occurrence region is flow from 104 degrees at 9 m/sec. Comparing this with the mean ring motion of 101 degrees at 10.5 m/sec it is seen that the directions are very comparable, but that the speed of the rings is significantly greater than the mean wind over the 850 to 400 mb layer. This confirms the earlier results showing that the ring clouds do not extend to 400 mb since it is not likely that the ring clouds travel faster than the wind. But it is observed that above 700 mb the wind speed drops off noticeably with height. The 850 mb to 500 mb layer mean wind results are 097° at 10.2 m/sec where now both wind speed and direction agree well with mean ring motion. Taking the 850 mb to 600 mb mean yields a mean wind of the same direction but somewhat higher speed. Thus in consideration of the reasonable hypothesis (important, in need of investigation) that the ring clouds travel with or at slightly less than the mean wind speed over their depth and in the same general direction as the wind over that depth, the results found here seem to indicate that the clouds extend to heights not much above 500 mb and this finding from the wind data is in general agreement with the radar and aircraft estimated cloud height and thermodynamic sounding inferred cloud height results discussed earlier. There is, therefore, now good evidence that the ring clouds on July 18 in the South Grid region are confined with respect to height to the middle troposphere or slightly lower.

The next wind analysis deals with the wind profiles in and beyond the ring occurrence region and over the period of occurrence. The July 18 12Z, 15Z and 18Z wind sounding data from 1000 mb to 300 mb for the fixed ships Oceanographer north to Rockaway are used. These wind data

and only physical atmospheric process that can result in such a pattern is ascent in the cloud wall region and subsidence (or at least no rising motion of note) in the center of the ring.

2.3.1 Winds

Most all wind analysis in this study is based on the fixed ship and Barbados rawinsonde data. However, supporting data were obtained from a rather new method of obtaining winds, utilizing computer correlation of cloud displacements from ATS digital data. The rawinsonde wind data are treated in a manner similar to the temperature and moisture data except that the wind data are considered over a longer period of time on July 18. This is due, in part, to the occurrence of many missing wind observations in the 3-hourly rawinsonde flights at Rockaway, but primarily due to the desire to look at the dynamics outside the time span of the numerous ring occurrences. A station with winds missing at a standard observation time in the experiment negates obtaining area-average divergence, vertical motion, and relative vorticity values, due to the method used to obtain these results which will be discussed shortly.

An important point in regard to the general wind analysis should be noted at this time. In pursuing the analysis of wind profiles and cloud motion comparisons, it became evident that Rainier winds at all levels to ~300 mb are westerly and thus considerably in opposition to the easterly flow at Rockaway and south, while all stations are under the influence of the easterly flow on the southern side of the aforementioned surface high pressure system to the north of the ring grids.

Thus the Rainier wind data were dropped from consideration in this study. Also in regard to missing wind data, inferring winds geostrophically from the pressure field is ignored because of the closeness of the BOMEX region to the equator where the geostrophic approximation becomes uncertain.

Wind data (u and v components) are extracted from the rawinsonde soundings at 50 mb intervals or at significant levels from 1000 mb to sounding termination generally occurring around 300 to 400 mb. The considered wind data for the fixed ships excluding Rainier cover the period from 0300Z on July 18 to 0000Z on July 19, while for island station Barbados the period covered is 0600Z on July 18 to 0600Z on July 19.

The first use of the wind data is to compare the mean ring motion in the area between Mt. Mitchell and Discoverer during the period 1247Z to 1431Z on July 18, as discussed earlier, with the mean wind profile in that area during that period. To obtain the mean wind profile, the 12Z and 15Z wind data at Mt. Mitchell and Discoverer at the 1000, 850, 700, 600, 500 and 400 mb levels are utilized. The wind data levels above are chosen for their approximately equal vertical spacing (~1500 m) to avoid the necessity of weighting vertical averages. Utilizing the above data a space-time mean wind at each wind level over the South Grid honeycomb ring pattern occurrence time and region is calculated, along with the vertical means of the space-time individual wind level means between 850 mb and 600, 500 and 400 mb. The Fig. 11 space-time cross section displays the Mt. Mitchell-Discoverer area wind profiles (plotted in conventional symbols) at 12Z and 15Z, along with other available wind profiles at the fixed ship stations during the 12Z to 18Z period, all of which will be discussed further on.

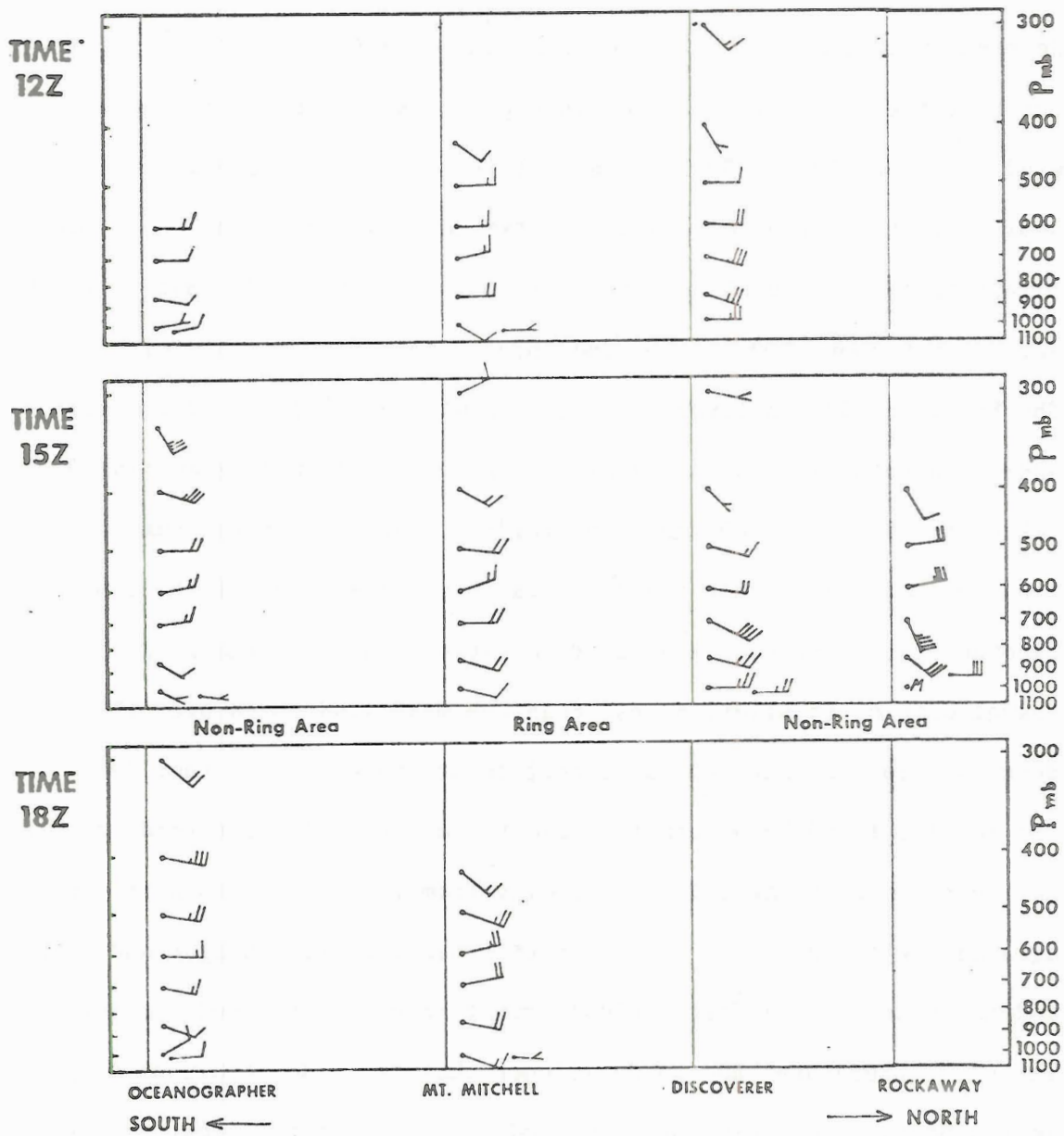


Figure 11 BOMEX July 18 Fixed Ship Wind Field Observations Time - North↔South Space - Height Cross Section Plotted in Conventional Wind Observation Symbols. (Half feather = 5 kts; Full feather = 10 kts).

The results of the averaging procedure are that the mean wind between 850 mb and 400 mb in the ring occurrence region is flow from 104 degrees at 9 m/sec. Comparing this with the mean ring motion of 101 degrees at 10.5 m/sec it is seen that the directions are very comparable, but that the speed of the rings is significantly greater than the mean wind over the 850 to 400 mb layer. This confirms the earlier results showing that the ring clouds do not extend to 400 mb since it is not likely that the ring clouds travel faster than the wind. But it is observed that above 700 mb the wind speed drops off noticeably with height. The 850 mb to 500 mb layer mean wind results are 097° ay 10.2 m/sec where now both wind speed and direction agree well with mean ring motion. Taking the 850 mb to 600 mb mean yields a mean wind of the same direction but somewhat higher speed. Thus in consideration of the reasonable hypothesis (important, in need of investigation) that the ring clouds travel with or at slightly less than the mean wind speed over their depth and in the same general direction as the wind over that depth, the results found here seem to indicate that the clouds extend to heights not much above 500 mb and this finding from the wind data is in general agreement with the radar and aircraft estimated cloud height and thermodynamic sounding inferred cloud height results discussed earlier. There is, therefore, now good evidence that the ring clouds on July 18 in the South Grid region are confined with respect to height to the middle troposphere or slightly lower.

The next wind analysis deals with the wind profiles in and beyond the ring occurrence region and over the period of occurrence. The July 18 12Z, 15Z and 18Z wind sounding data from 1000 mb to 300 mb for the fixed ships Oceanographer north to Rockaway are used. These wind data

are presented in Fig. 11. From this figure it is seen that in the near-ring region of Mt. Mitchell and Discoverer the vertical shear of the horizontal wind between 900 mb and 500 mb (the cloud depth layer) is on the order of 5 to 10 knots (2.5 to 5 m/sec) and 20 degrees. It is observed that the speed shear is a positive one aloft at Mt. Mitchell and a negative one aloft at Discoverer. Thus between these two stations, where the numerous rings occur, it appears that the vertical shear is quite small, on the order of a few knots in speed and small in direction. Vertical mean wind in this area, as stated previously and valid also for 18Z, is on the order of 100° at 10 m/sec.

In the non-ring regions of Oceanographer and Rockaway it is seen that the 900 mb to 500 mb shear is on the order of 15 knots (7.5 m/sec) and 30° to 50° , the latter being present at Rockaway. Also it is noted in the high level data available that there is a general shift at all stations to more southerly flow with slightly decreased speeds compared to the levels below. Vertical mean winds in the non-ring areas show Oceanographer speeds slightly less than those in the ring area and Rockaway speeds notably higher. These results are generally representative of the 12Z to 18Z period.

In regard to the horizontal shear of the wind from Oceanographer north to Rockaway, it is seen from Figure 11 that in the low levels the easterly wind speed increase is on the order of 20 knots (10 m/sec) with individually higher values. In the middle levels (500 to 600 mb) there is seen to be little or no speed change south to north. The higher levels show the reverse of the low level horizontal shear, displaying an easterly wind speed decrease north, but this result must be

considered in regard to much missing wind data at these levels. Between stations the horizontal speed shear is on the order of 5 to 10 knots (2.5 to 5 m/sec) with not any notable difference between ring and non-ring areas. The low level increase of easterly wind speed going north constitutes one possible important mechanism for initiating and/or maintaining ring cloud circulation. This shear is a cyclonic one implying near surface frictional convergence, the CISK (Conditional Instability of the Second Kind) mechanism detailed by Charney and Eliassen (1964) in their discussion of tropical depression development. No pattern of directional shear south to north or between stations in ring and non-ring areas is evident.

In regard to time-height cross section analysis, the above wind field results are found to be generally applicable to the time periods a few hours before 12Z and after 18Z.

2.3.2 Divergence

This and the next two sections deal with the dynamic characteristics of the BOMEX Ring Study area on July 18 which are derived from the basic u and v component wind data. Fixed ship (excluding Rainier) and Barbados surface winds and upper air wind data at 50 mb intervals from 1000 mb to 300 mb are utilized. Fixed ship data times of 03Z, 09Z and 15Z on July 18 and 00Z on July 19 are considered. To obtain Barbados data for these times, time interpolation of the July 18 06Z and 18Z and July 19 06Z observations wind data is performed. Missing desired levels wind data in the vertical are obtained by linear interpolation; BOMEX Ship Station Surface Observations (1969) wind data provide interpolation data for the case of near surface missing winds.

The first dynamic parameter to be discussed is the horizontal velocity divergence in the ring study area on July 18. To obtain values of this parameter a method based on first principles is employed. This method is discussed by Vonder Haar and Smith (1971) and starts with the first principle of horizontal divergence:

$$\text{DIV}_2 \vec{V} = \frac{\partial u}{\partial x} + \frac{\partial v}{\partial y} = \frac{1}{A} \frac{dA}{dt} \quad [2-3]$$

where A is the horizontal area of a fluid element whose boundary is delineated by a continuous chain of fluid particles and \vec{V} is the atmospheric wind velocity vector. From this a "polygon" method of obtaining the time rate of change of area of the fluid element (and consequently the divergence) by noting the displacements with time of the fluid particles forming the element boundary is constructed, where the N polygon vertices of an N -sided polygon of area A_N are formed by given fluid element boundary particles (clouds). The assumption of cloud element motion with the wind is made. It is understood that the area change must be small compared to the area or there will be great uncertainty as to the value of A_N to be used. Also the greater the number of polygon vertices, the more accurate will be the results obtained from this divergence method. The details of this "polygon" method are discussed in Appendix C, Part I.

However for the purposes of this study the wind data are available in u and v components and not in cloud displacement coordinates. Thus the available wind data are translated into latitude-longitude cloud displacement coordinates. The conversion from u and v wind

components to cloud displacement coordinates for the fixed ships and Barbados data at the times stated above, as well as the calculation of 50 mb interval divergence using the modified equation [2-3] discussed in Appendix C, are accomplished by computer with the u and v wind components at 50 mb intervals as data input. Where wind data are missing at a given observation time and level at one of the ships or Barbados forming a given triangle, the form of polygon used in this cloud ring study, the polygon does not exist and no divergence value can be obtained over that area at that time. It is understood here that the divergence values obtained are representative of the area covered by the polygon and are not point values. The fixed ship-Barbados station combinations making up the four triangular polygons used to obtain July 18 divergence and other dynamic parameter values are shown in Table 2 along with pertinent information about the polygons. Reference to Fig. 3 helps to locate the polygons visually.

TABLE 2

BOMEX FIXED SHIPS - BARBADOS POLYGON DATA

Polygon No.	Stations	Midpoint Location	Area, Km ²
1	OC, MM, DIS	10.3 N 54.4 W	103317
2	MM, DIS, ROCK	12.8 N 55.2 W	60775
3	MM, DIS, BARB	12.2 N 56.6 W	85085
4	DIS, ROCK, BARB	13.7 N 56.5 W	65637

OC=Oceanographer, MM=Mt. Mitchell, DIS=Discoverer, ROCK=Rockaway,
BARB=Barbados, W. I.

Horizontal divergence profiles are obtained for as many of the polygons as are defined at the 03Z, 09Z, 15Z and 00Z times. At 15Z on July 18 all four polygons are defined and the divergence profile results for this time are presented in Fig. 12. These results describe the divergence situation during the time of maximum South Grid ring occurrence and cover both the ring and non-ring regions. The profile itself should be considered more important than the absolute magnitudes of the individual data points, especially in regard to those which show large fluctuations due most likely to triangle polygon use rather than more numerous vertex polygons, which triangle polygons tend to emphasize a major wind fluctuation at one of their station vertices. From Fig. 12 it is seen that in the South Grid ring area (Polygon 1) there is low level convergence and middle level divergence, with a return to convergence in the high levels. Polygon 3, covering the non-ring area west of the rings, shows a very similar profile except that there is no high level convergence evident. Polygons 2 and 4, representative of non-ring regions, display generally more convergence than do Polygons 1 and 3, especially in the low levels and notably in the Polygon 4 area in the upper middle and higher levels. Polygon 2, somewhat closer to the ring area than Polygon 4, shows generally the same middle level profile as Polygon 1. In regard to the large fluctuations in divergence values between 600 mb and 800 mb for Polygons 2 and 4, the wind data for 15Z at Discoverer and Rockaway show relatively large wind speeds present at these pressure levels compared to neighboring levels. Finally the additional divergence profile results at the times before and after 15Z show general similarity to the 15Z findings.

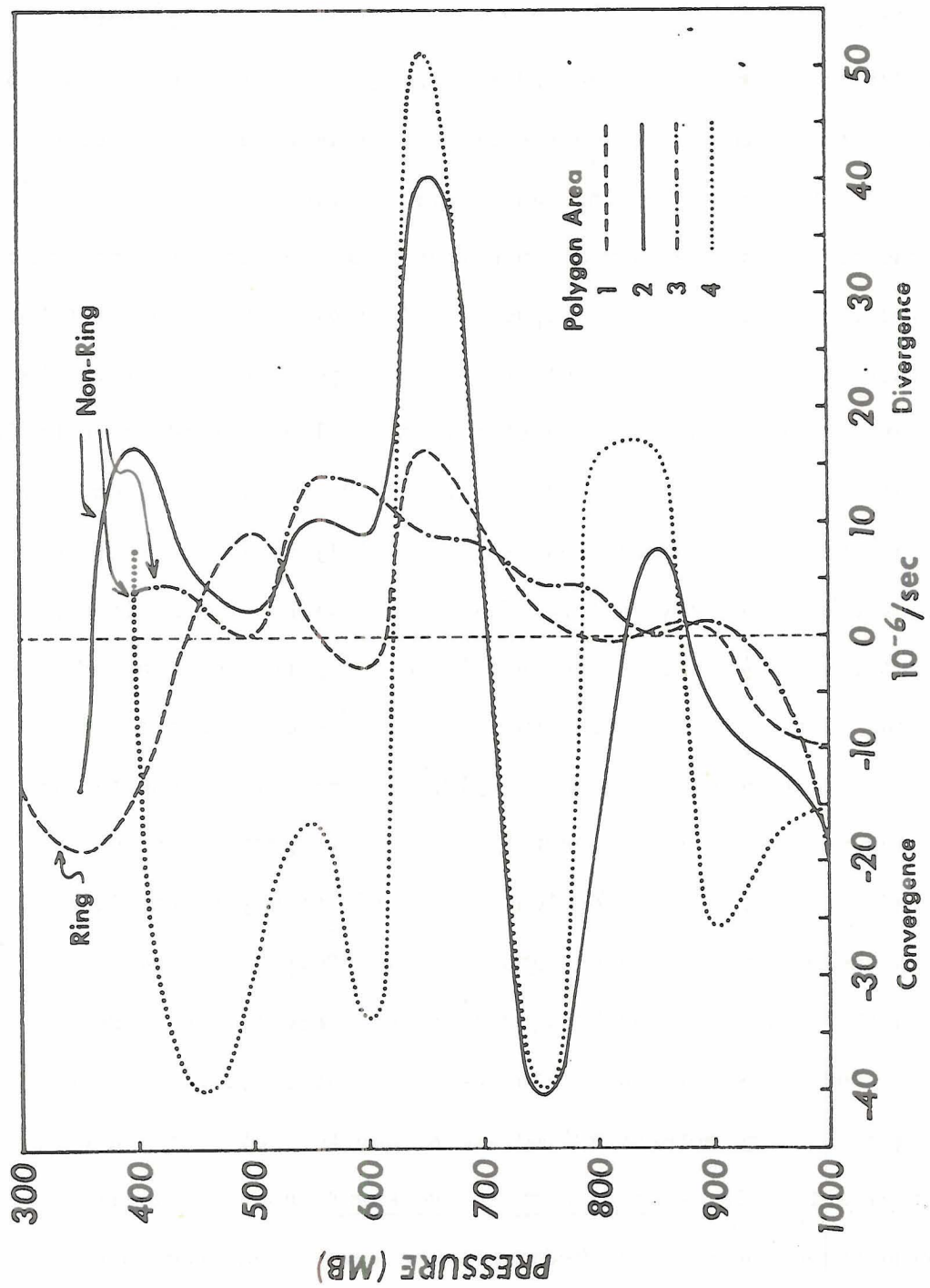


Figure 12 BOMEX July 18 15Z Ring Study Area Horizontal Velocity Divergence Vertical Profiles Obtained Using Polygon Method.

2.3.3 Vertical Velocity

The next dynamic parameter of interest and one which follows from the horizontal divergence calculations is the vertical motion field in the ring study area and its variations between ring and non-ring regions. As stated earlier wind data at the same times and stations are utilized in all the dynamic analyses on July 18. This parameter follows from the divergence as a result of the kinematic method employed to obtain vertical velocity, that of the pressure coordinates (pressure P replaces height Z as the vertical coordinate) continuity equation (hydrostatic equilibrium assumption implicit):

$$\left(\frac{\partial u}{\partial x} \right)_P + \left(\frac{\partial v}{\partial y} \right)_P + \frac{\partial \omega}{\partial P} = 0 \quad [2-4]$$

where $\omega = \frac{dp}{dt}$ is the vertical velocity in millibars per second and $\left(\frac{\partial u}{\partial x} + \frac{\partial v}{\partial y} \right)_P$ is the horizontal divergence, DIV_2 , measured along a constant pressure surface as is that obtained in this study since all wind data are being considered at given pressure levels. Equation [2-4] is integrated over a layer of atmosphere from its lower boundary pressure P_1 to its upper boundary pressure P_2 ($P_1 > P_2$) to obtain the vertical velocity equation:

$$\omega_2 = \omega_1 + \overline{DIV}_2 [P_1 - P_2] \quad [2-5]$$

where ω_1 and ω_2 are the vertical velocities at the lower and upper boundaries of the layer, respectively, and \overline{DIV}_2 is the mean divergence in that layer. Note that downward motion is positive in the ω vertical motion system. The hydrostatic assumption is valid due to the synoptic

scale nature of the wind data used. If later data become available on the scale of the ring clouds themselves, then great care must be taken as to the assumptions made due to the smaller space scale (meso-scale) nature of the rings.

Vertical motion profiles are computer calculated from Equation [2-5] for the four polygon areas and July 18 03Z, 09Z and 15Z and July 19 00Z times. Vertical velocities are obtained at 50 mb intervals from 975 mb to 275 mb, utilizing the previously calculated 50 mb interval horizontal divergence values as the means of 50 mb thick layers. At the earth's surface $\omega=0$ is assumed; no upper boundary condition is imposed because of the 300 mb level rawinsonde data limit. Where polygon divergence values are missing, no vertical motion computations are possible. As with the divergence results, the vertical velocity values are representative of the polygon areas as a whole. The ω vertical velocities are then converted to the w form in cm/sec, employing for this the hydrostatic conversion:

$$\omega = -\rho gw$$

[2-6]

where ρ is the air density at the pressure level where ω is being considered and g is the gravitational acceleration, 980 cm/sec².

The vertical velocity profiles for 1500Z on July 18 in the four polygon areas are shown in Fig. 13. In the ring cloud region (Polygon 1) the vertical motion is upward between the surface and ~700 mb and is downward (subsidence) at levels above this. Above 350 mb there is an apparent return to upward flow. In the non-ring region (Polygon 2) the vertical motion is upward at all levels except the highest around

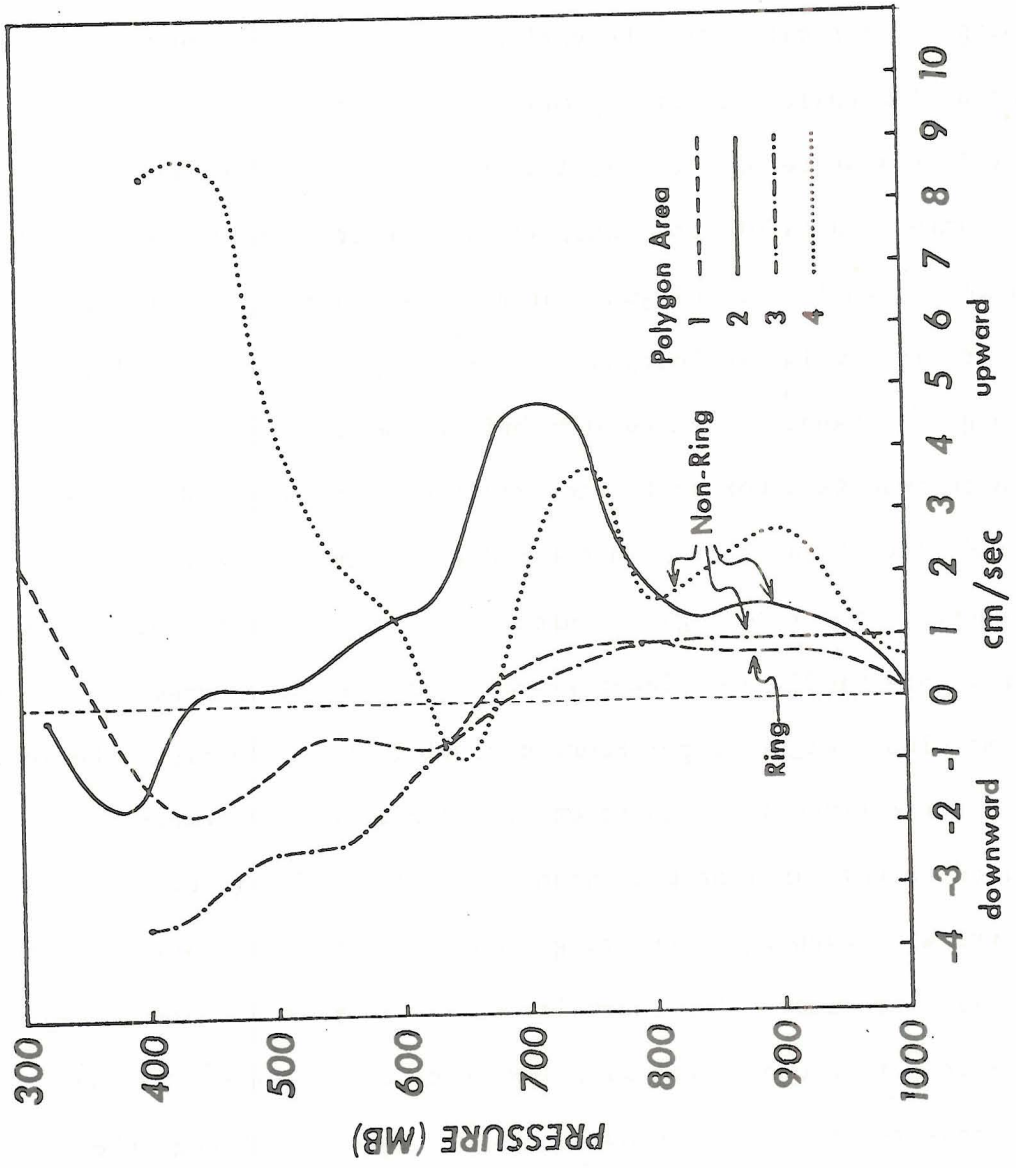


Figure 13 BOMEEX July 18 15Z Ring Study Area Vertical Velocity Vertical Profiles Kinematically Computed from Figure 12 Horizontal Divergence Profiles.

and above 400 mb. At the other wind data times giving July 18 vertical motion results it is observed that in the hours somewhat before 15Z, the Polygon 1 ring region profile is similar to that at 15Z, while in hours after 15Z it changes to one of upward motion at all levels. For the Polygon 2 non-ring area the earlier profile is also quite similar to that at 15Z while the later profile changes to one of downward motion at levels above 650 mb. At 15Z the Polygon 3 area shows low level upward motion and middle to higher level downward motion, very similar to Polygon 1, while the Polygon 4 area shows generally upward motion at all levels similar to Polygon 2. The Polygons 3 and 4 profiles show no great change in the periods before and after 15Z.

These results demonstrate the existence (hypothesized earlier) of subsident vertical motion in the middle and higher levels of the troposphere in the ring region, which correlates now with the findings of stable, dry middle and higher levels from the thermodynamic data and the radar cloud heights upper bound occurring at middle tropospheric levels. These three findings together indicate the existence of a ring cloud height limiting mechanism in the form of a general synoptic subsidence with capping of the ring cloud vertical circulations by the stable "lid" produced. The lower levels in the ring occurrence region show upward motion concurrent with low level convergence. The non-ring regions show generally upward motion at all levels, although there is some decrease in this motion at the higher levels in some of the non-ring region profiles. Also the earlier discussed disappearance of the "honeycomb" ring pattern in the South Grid area between 15Z and 18Z is correlated with the change in the Polygon 1 area vertical motion profile between 15Z and later times, over which period the motion

changes to upward at all levels. The generally upward motion in the non-ring (polygons 2 and 4) regions correlates with the easterly wave cloud "tail" extending into these regions with attendant general convergence and resultant dense cloudiness.

2.3.4 Relative Vorticity

The final but important dynamic parameter is the relative vorticity in the ring and non-ring regions of the BOMEX Ring Study area on July 18. A first principles equation for relative vorticity is modified to a form which utilizes the wind data and polygons in the same manner as that used in the divergence calculation. The u and v component wind data, converted to cloud displacement coordinates as in the divergence computations, are used to obtain relative vorticity values. The derivation of the modified relative vorticity equation to be used in the actual calculations, again based on the presentation by Vonder Haar and Smith (1971), is given in Appendix C, Part II. The first principles equation is:

$$\zeta = \frac{C}{A_N} = \frac{\oint \vec{V} \cdot d\vec{s}}{A_N} \quad [2-7]$$

where ζ is the relative vorticity or vertical component of the total vorticity, $\vec{\nabla} \times \vec{V}$, C is the circulation of the fluid obtained by integration of the velocity vector \vec{V} around a closed curve whose infinitesimal element is $d\vec{s}$, and A_N is again the area of the N-sided polygon with N vertices. Positive (cyclonic) and negative (anti-cyclonic) relative vorticity follows from the "right hand screw rule" sign convention for integration around closed curves.

Computer-calculated polygon-area-average relative vorticity profiles are obtained from the modified equation [2-7] for the four polygons and July 18 03Z, 09Z and 15Z and July 19 00Z times. Values are calculated at 50 mb intervals from 1000 mb to 300 mb. Again, missing wind data negates computation of polygon relative vorticity profiles.

The relative vorticity profiles in the BOMEX Ring Study area at 1500Z on July 18 are shown in Fig. 14. This shows that in the ring region (Polygon 1) cyclonic vorticity prevails, weakly in the lowest levels, below 500 mb with anticyclonic vorticity above 500 mb. The non-ring region (Polygon 2) exhibits generally cyclonic vorticity at all levels, though somewhat small, with the exception being the large anticyclonic fluctuation from the mean between ~600 mb and 700 mb due to the aforementioned relatively high wind speeds at these levels at Discoverer and Rockaway at 15Z. At the earlier times of interest the Polygon 1 ring region profiles are similar to that at 15Z, while after 15Z the lower level part of the profile changes to anticyclonic vorticity values. The Polygon 2 non-ring region profiles before and after 15Z show generally little change from that at 15Z, with the 00Z July 19 profile showing a major anticyclonic vorticity fluctuation present at ~600 mb to 700 mb similar to that at 15Z. Polygon 3 at 15Z shows generally anticyclonic vorticity except very near surface and between ~700 mb and 800 mb. At the earlier and later times Polygon 3 displays anticyclonic vorticity at all levels. Polygon 4 at 15Z shows a marked cyclonic vorticity profile which is little changed at the later time.

Altogether these results generally show a cyclonic vorticity present in the lower and middle troposphere regions where the ring cloud

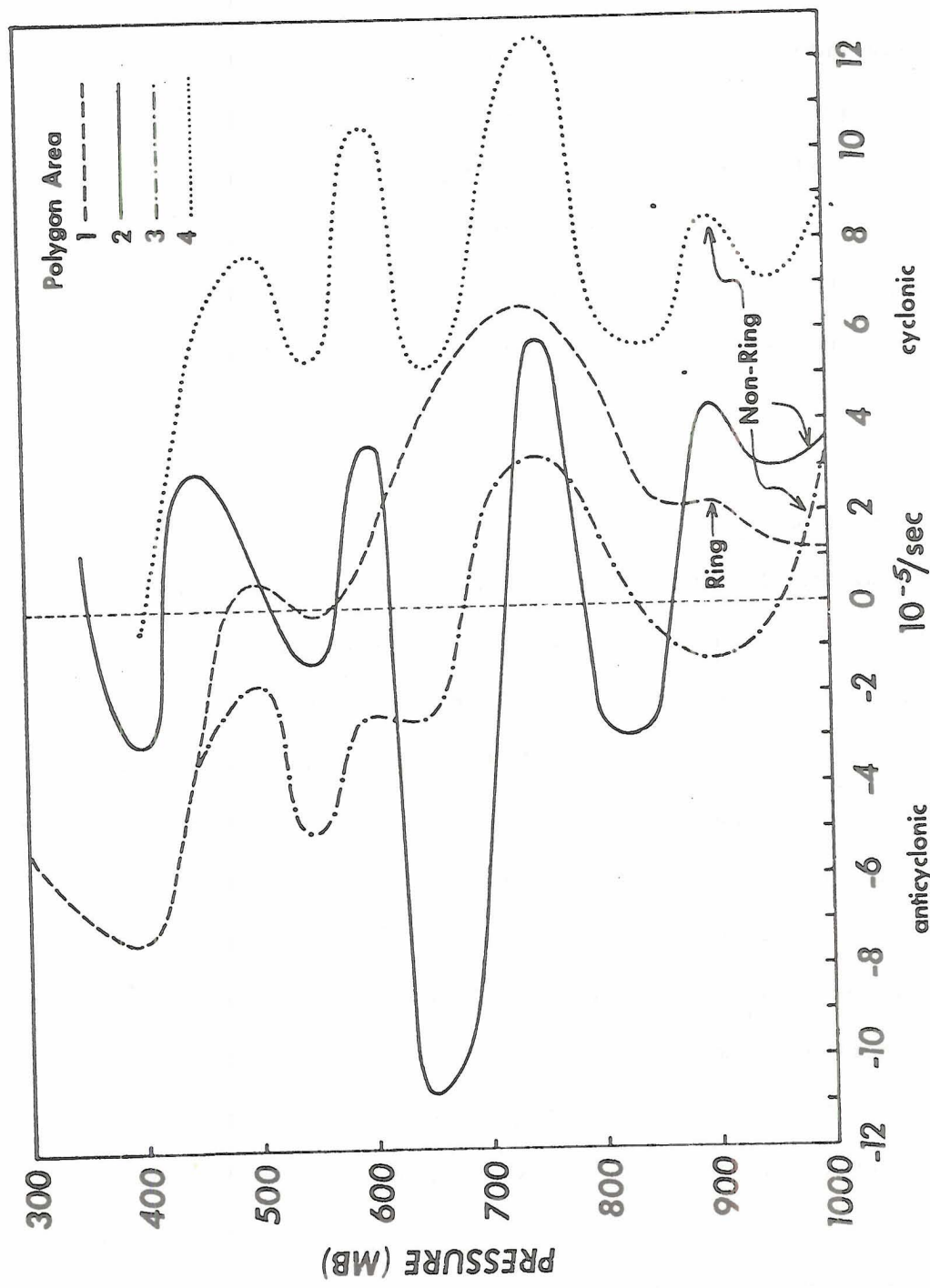


Figure 14 Same as Figure 12 for Relative Vorticity.

systems appear to be confined, while the upper troposphere regions where data is available display an anticyclonic vorticity. These results correlate well with the ring occurrence region low level cyclonic and high level anticyclonic horizontal wind shears discussed earlier. The non-ring regions, especially that near the easterly wave cloud "tail", display generally marked cyclonic vorticity at all levels. Also the observed change in the Polygon 1 area lower level profile from cyclonic to anticyclonic vorticity between 15Z and 00Z correlates with the observed disappearance of the honeycomb ring system at 18Z.

2.3.5 Summary

In Summary the BOMEX July 18 cloud ring structure synoptic scale dynamic description is as follows: In the South Grid ring occurrence region horizontal winds are generally easterly at speeds on the order of 5 to 10 m/sec, they display 900 mb \rightarrow 500 mb cloud depth layer vertical shear of $\sim 20^{\circ}$ and 2.5 m/sec to 5 m/sec, and they display an inter-ship station horizontal shear in speed of ~2.5 m/sec to 5 m/sec per 250 km. The horizontal shear is cyclonic in the low levels changing to anticyclonic in the high levels. In the non-ring areas the generally easterly horizontal wind vertical shear is 30° to 50° and ~ 7.5 m/sec over the 900 mb \rightarrow 500 mb layer, the horizontal wind speeds are near or notably higher than those in the ring region, and the horizontal shear between ship stations is essentially the same in magnitude and nature as that prevalent in the ring region. In the ring area in the low levels weak convergence, upward motion and weak cyclonic relative vorticity conditions are prevalent, while in the middle levels divergence,

subsidence and greater cyclonic relative vorticity are observed. In the higher levels there is a return to convergence and upward motion, with a change to anticyclonic relative vorticity. In the non-ring regions convergence, upward motion and cyclonic relative vorticity are in general prevalent at all levels. In the ring occurrence region, but in the period from 18Z on when the rings are observed to disappear, the dynamic conditions are observed to change to those similar to non-ring region conditions.

3.0 CLOUD RING - TROPICAL ATMOSPHERE COMPARISONS

Having determined the physical (phenomenological) properties of the rings and the thermodynamic and dynamic conditions prevalent during the cloud ring occurrence situation of July 18, 1969 in the BOMEX area, it is now desired to compare that situation with the BOMEX Phase IV periods a whole and with the work of other cloud ring investigators. A comparison of cloud ring and mean tropical conditions (Loranger, 1974) is not discussed in detail here, but is summarized in Section 4.0

3.1 Physical Comparisons

Table 3 presents a summary listing of cloud ring physical properties found by various investigators including the BOMEX study. For the BOMEX and other ring studies the given locations of the studies are the mean locations of a set of ring structures used in that particular analysis. The Ruprecht et al. (1973) study involves only the single ring observed on March 19, 1969. Note is taken that one of the physical studies is accomplished using only non-geosynchronous TIROS 1 satellite data and another using only weather radar data. This data usage leads to the observed lack of ring lifetime information for the non-geosynchronous data study and to an indeterminant lifetime for the radar data case.

The table shows that the ring sizes are all on the order of approximately 60 km mean inside diameter though with notable variations. The 50 km mean ring diameter found by Krueger and Fritz (1961) in their mid-latitude region of study is the smallest of the four results.

TABLE 3 CLOUD RING PHYSICAL DESCRIPTION
Comparison of Various Investigation Findings

63

SOURCE/ INVESTIGATOR(S)	DATE	DATA SOURCES(S)	LOCATION (mean)	RING SIZE (Diameter) km	RING CLOUD HEIGHTS km	RING DIAMETER TO RING CLOUD HEIGHT RATIO	RING LIFETIME OB=OBSERVED EST=ESTIMATED	MISCELLANEOUS CHARACTERISTICS
Loranger and Vonder Haar (Present, 1973)	July 18 1969 BOMEX PHASE IV	ATS 3 and DIS- COVERER Selenia Radar	10-15°N 52°W	80 km mean 55-115 km range (inside dia)	Upper bound, 7.1 km mean ~5-11 km range Estimated, ~6km mean	13:1	6 hrs. (OB)	E-W elongation; EW ~1.7; 9-19 km NS wide cloud bands Nighttime oc- currence
Vonder Haar, et. al. (1968)	April 25 1967	ATS 1	Central Pacific 10°S-10°N	60 km mean 30 km-90 km range (inside dia)	N.A.	N.A.	8 hrs. (OB) 14-16 hrs. (EST)	Notes some de- parture from circular form
Krueger and Fritz (1961) Fritz (1965) Hubert (1966)	Several days (1960- 1964)	TIROS 1	35°N 55°W	50 km median 20-90 km range	1.2 km-3.6 km range	31:1	N.A.	19-28 km wide cloud bands. Small distor- tion in direc- tion of wind shear noted.
Ruprecht, et al. (1973)	March 19 1969 APEX	METEOR Selenia Radar	0°N, 32°W	60 km (not constant)	to-8 km	7.5:1	1½ hrs. (OB) 2-3 hrs. (EST)	Variable sizes noted on other days; Single ring on Mar 19

The 20 km diameter sizes mentioned by these authors are of too small scale to be included in the mesoscale ring structure analysis being carried out here and should be dealt with as cumulonimbus scale phenomena. As for ring cloud heights, the studies reveal that the maximum mean heights, on the order of 6 to 8 km, occur in the equatorial areas, while from the mid-latitude area study by Krueger and Fritz (1961) the maximum heights are around 3.6 km. The ring cloud diameter to height ratio ranges from about 10:1 in the tropical regions to 30:1 in the mid-latitudes. Thus it appears that the mid-latitude rings are flatter and of somewhat smaller diameter than those occurring in the tropical regions. This indicates the likelihood of some different set of conditions for ring cloud occurrence in the mid-latitudes compared to the tropics.

Basic time duration values for ring patterns are seen to be available for all but the Fritz et al. cases. Data shortcomings such as nighttime terminating ring observation by satellite or weather radar tracking interruptions lead to minimmm lifetime values, questionable in general. The small amount of information available on this ring aspect negates coming to any solid conclusions on this subject at present, but the July 18 BOMEX day does show a shorter ring cloud lifetime than that of the Vonder Haar rings. The Ruprecht et al. (1973) single ring actual lifetime (radar study mentioned previously) is considered very indeterminant. Tracking of the March 19 ring cloud was interrupted by a rawin ascent and upon its completion the ring could not be located. ATS III data on this ring are not available due to location of the ring at the extreme eastern edge of the satelite picture. Other satellites also provided no data on this ring.

The subject of duration needs to be studied more in order to broaden the knowledge of ring structure lifetimes. This will become possible with the availability of infrared geosynchronous satellite pictures and/or continuous weather radar observations.

It is observed that the rings do occur in low and mid-latitude regions and in various seasons, this combined with the earlier described ring occurrences on a number of days during the BOMEX experiment and the note of presence of ring patterns during the nighttime hours. Miscellaneous characteristics shown in Table 3 demonstrate some further physical similarities and differences between rings in the various studies.

3.2 Thermodynamic Comparisons

The first few following paragraphs deal with obtaining mean temperature and moisture profiles, as well as mean surface air temperature - sea surface temperature differences and consequent air-sea interface heat fluxes, for the BOMEX Phase IV covering July 11 to 28, 1969 and comparing these findings with those for the July 18 ring occurrence day. Temperature and moisture findings of other ring cloud investigations will also be compared to the BOMEX ring day results.

The first mean thermodynamics to be discussed are the mean temperature profiles for the BOMEX July 10 to 30, 1969 period obtained from the sun-synchronous Nimbus III SIRS-A radiation-inversion temperature profiles discussed earlier. The area covered by the averaging process extends from 7S to 27N and 30W to 75W, the latter chosen to

include data some 15° on either side of the BOMEX Ring Grids. Zonal averages of the ~1200 LT and 2400 LT SIRS temperature observations are calculated over 2° latitude zones and for the standard SIRS data levels from 1000 mb to 1 mb. The average of the 1200 LT and 2400 LT observations is considered representative of ~1800 LT. With an $\sim 2^{\circ}\text{C}$ diurnal temperature variation over tropical oceans, the 1200 LT - 2400 LT mean is also a rather representative mean temperature for the day as a whole.

Figure 15 presents the 8N and 12N BOMEX Period IV mean SIRS temperature profiles, along with the July 18 15Z Oceanographer and Discoverer area rawinsonde and SIRS-A temperature soundings presented previously in Figure 10. The 8N and 12N profiles are chosen for their very close correspondence with the latitudinal locations of ships Oceanographer and Discoverer respectively. From Figure 15 it is seen that in the 8N region the SIRS July 18 15Z and BOMEX Period IV mean temperature profiles differ very little except near the surface where the July 18 temperatures are higher, while at 12N the two profiles differ only very slightly in the lowest and highest levels, but show the July 18 temperatures to be 1°C to 2°C cooler than the mean in the middle levels. Note that the observed deviations from the mean temperatures are due to both the differences in representative times of the daily and mean soundings and actual daily weather variations. In regard to the general variation in the SIRS mean temperature profiles from 7S to 27N, they show the expected cooling going north from the equator, greatest at the surface, and very little N-S variation in temperature in the higher levels in the near-equator regions. These results lend credence to the validity of the SIRS mean temperature profiles obtained.

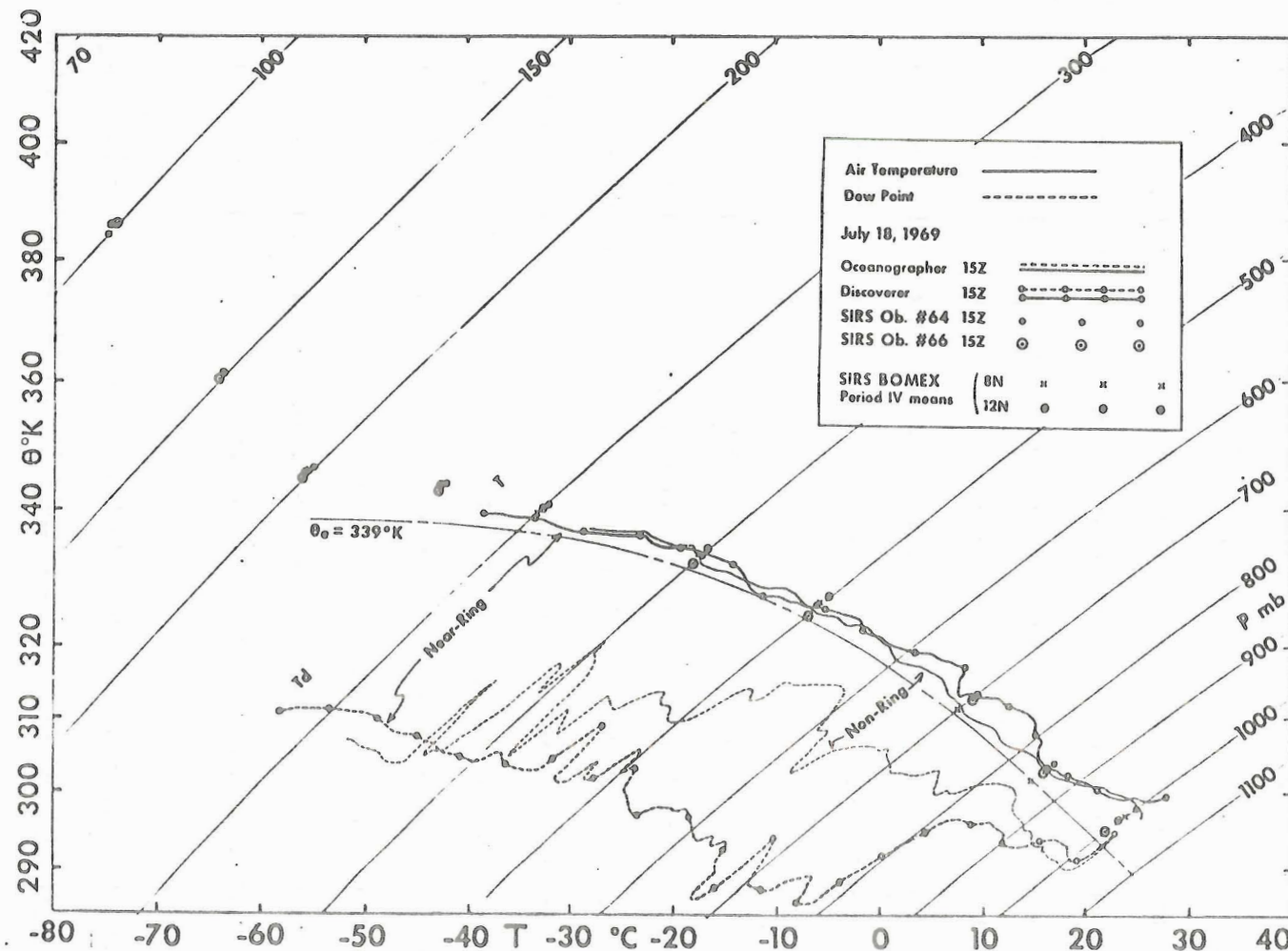


Figure 15 BOMEX July 18 Fixed Ship Rawinsonde Temperature and Dew Point and NIMBUS III SIRS-A Radiation Inversion Temperature Soundings and BOMEX Phase IV Mean SIRS-A Temperature Soundings.

Another set of mean soundings for the BOMEX Phase IV period is obtained from the fixed ship rawinsonde temperature and specific humidity moisture data. The 12Z and 18Z daily temperature and specific humidity data at 25 mb intervals from 1000 mb to 300 mb are averaged to produce the mean profiles. These times are chosen for maximum daily data availability and correspondence with the July 18 ring occurrence time period. Erratic and erroneous temperature and/or moisture data are eliminated from the averages through the use of ranges of acceptable values which vary with height in the atmosphere and are constructed from subjective examination of the raw data. Use of this method of data checking no doubt leads to occasional elimination of good data and retention of bad data.

The above procedure yields the BOMEX Period IV mean temperature and moisture profiles at the five fixed ships for 12Z and 18Z. General characteristics of the mean soundings going from south to north are a rather unstable layer from surface to ~940 mb, a stable layer between ~700 mb and 800 mb which is most defined to the north, and dryness increasing to the north. The dryness also shows the most marked increase at and above the stronger stable layer in the north. Except for the above the temperature lapse rates are generally moist adiabatic. The 12Z and 18Z mean sounding differences are very minor as is expected in the tropics.

Specific comparisons are made between the July 18 15Z Oceanographer and Discoverer T-q soundings and the 12Z and 18Z BOMEX Period IV mean T-q soundings at the same ships. These are displayed in Figure 16. Note that the 12Z and 18Z times form a mean at ~15Z. It is seen from the figure that at Oceanographer the July 18 and mean soundings show

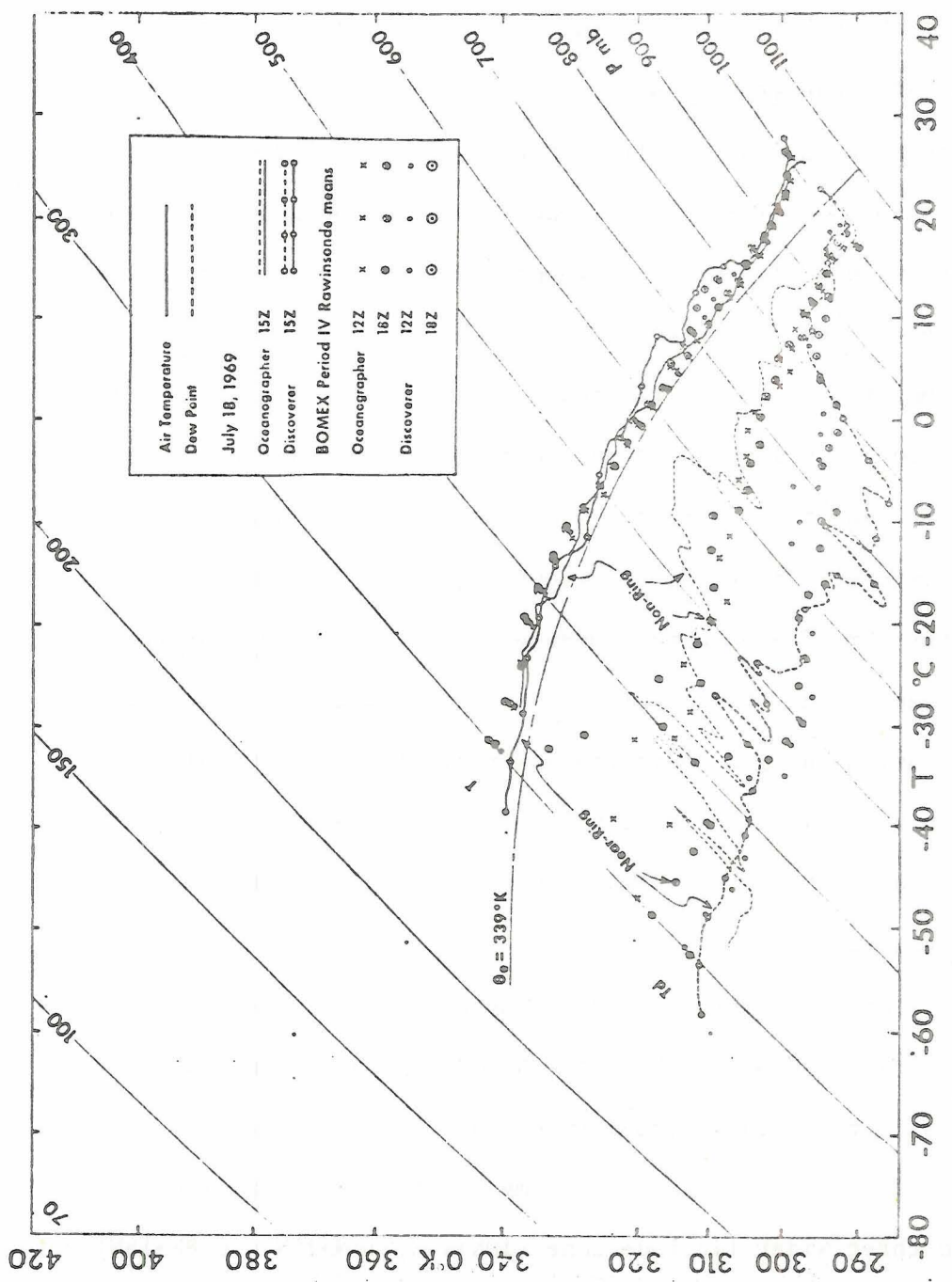


Figure 16 BOMEX July 18 and BOMEX Phase IV Mean Fixed Ship Rawinsonde Temperature and Dew Point Soundings.

a very similar temperature profile except near surface where the mean shows a somewhat unstable layer (related to the nearly dry adiabatic near-surface layer noted before in the ring occurrence regions and also observed in the other mean soundings). The July 18-mean moisture comparison at Oceanographer shows that the 18th is somewhat more moist than the mean in the lower half of the troposphere and similar to the mean above ~500 mb. The July 18-mean soundings comparison at Discoverer shows that on July 18 the lower troposphere temperatures are somewhat warmer than the mean with two well defined stable layers present on the 18th compared to one in the mean. The ~800 mb level stable layer present in both the 18th and mean soundings is more defined on the 18th. Both the 18th and mean soundings show the well-defined unstable layer near the surface. In the upper troposphere the temperatures for the 18th and the period are quite comparable. As for the Discoverer area moisture, comparison of the July 18 and mean soundings shows a much more rapid drying at and above the lower stable layer on July 18 than in the mean and this drier aspect is present to ~550 mb, above which the 18th is a bit more moist than the mean. Above 450 mb the moistures are comparable and small.

Anomaly analysis also provides a method of making daily-mean comparisons. This is done for both the Nimbus 3 SIRS-A temperature data and fixed ship rawinsonde temperature and specific humidity data. The SIRS 2° -latitude-zone BOMEX Phase IV mean temperature profiles are combined into three wider latitude zone (10N \rightarrow 14N, 14N \rightarrow 18N and 8N \rightarrow 18N) period mean profiles and the daily and period means in these zones are differenced to obtain the daily temperature anomaly profiles. As with the SIRS means, the anomalies are considered representative of ~1800 LT.

Specifically referring to the 10N \rightarrow 14N zone which covers the July 18 cloud ring occurrence region discussed in the above comparisons, but generally applicable to the entire 8N \rightarrow 18N zone covering most of Ring Grids area, the anomaly results are that the 18th of July displays relatively small deviations from the period mean, compared to various other days which show relatively large deviations from the mean. These non-mean days are observed to be those on which rather disturbed weather was occurring in or near the BOMEX area.

The anomaly procedure is also applied to the BOMEX Phase IV 12Z rawinsonde temperature and moisture data at fixed ship Discoverer. The July 11 \rightarrow 28, 1969 daily 12Z soundings are corrected with regard to erratic data as discussed previously and compared to the computer-processed BOMEX Phase IV period 12Z mean temperature and moisture soundings at Discoverer to yield the daily 12Z temperature and specific humidity moisture anomaly profiles. Temperature and specific humidity anomaly time-height cross sections, based on the daily anomaly profiles, are presented in Figs. 17 and 18, respectively. From these figures it is again seen that the 18th of July is a relatively small deviation day compared to various other days of the BOMEX Phase IV at 12Z in the Discoverer area. Partagas and Estoque (1970) have also performed a BOMEX Phase IV Discoverer 12Z rawinsonde temperature and moisture (dew point) anomaly analysis as part of their preliminary survey of BOMEX Phase IV meteorological conditions. The results of these authors' BOMEX Phase IV Discoverer 12Z anomaly analysis are significantly similar to those obtained by this investigator, though the results do differ in some specific details. The dates of notable anomaly occurrences as seen in Figs. 17 and 18 agree very well with the occurrence items of large anomalies as found by Partagas and Estoque

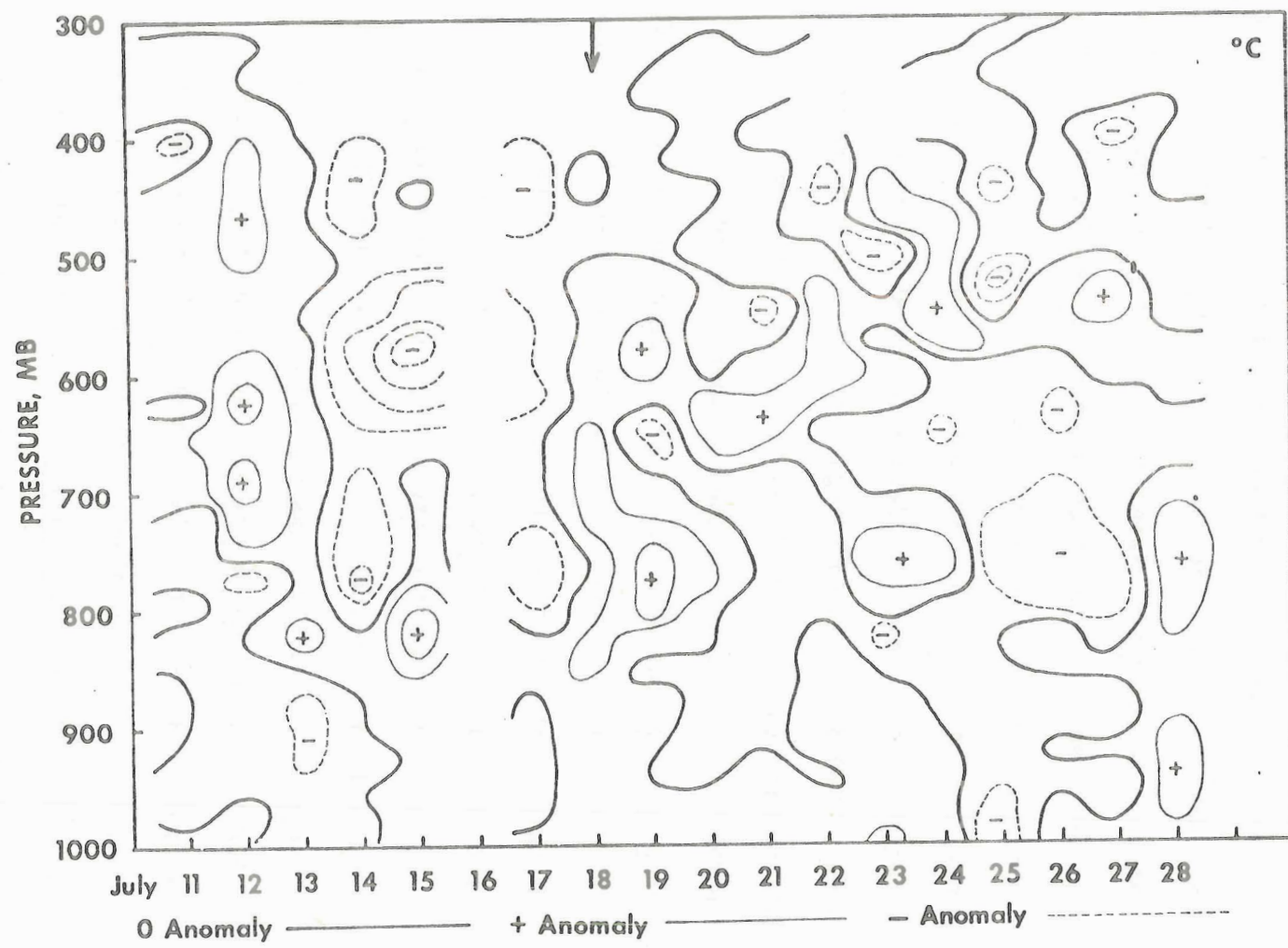


Figure 17 BOMEX Phase IV Time-Height Cross Section of Fixed Ship Discoverer 12Z Daily Temperature ($^{\circ}\text{C}$) Anomaly Profiles Based on Rawinsonde Data (Contour Interval 10°C).

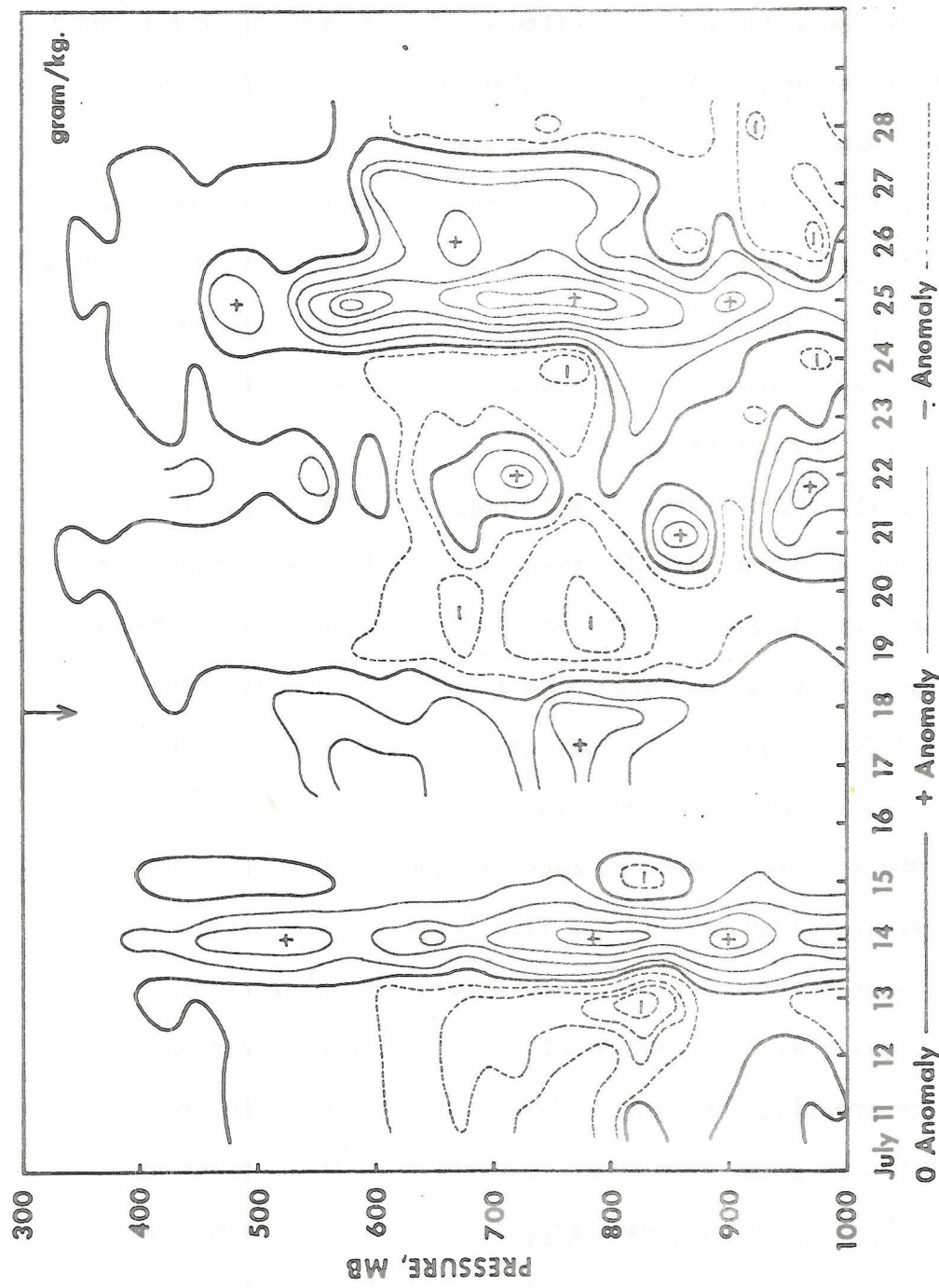


Figure 18 Same as Figure 17 for Specific Humidity Moisture in gr/kg (Contour Interval 1gr/kg).

in their anomaly analysis. Further in this line, with regard to temperature only, these large anomaly occurrence times agree well with the SIRS findings as discussed above and these large anomalies are all correlated with the relatively disturbed weather occurring in the BOMEX region at those times. Again note that there are specific detail differences among the various anomaly analyses.

In regard to the relationship between disturbed and undisturbed weather situations and the Figures 17 and 18 anomaly cross sections, it is noted that in the transition from disturbed to undisturbed weather there is a transition from cool-moist to warm-dry conditions, respectively, as would be expected.

In all the above thermodynamic comparisons show that the 18th of July conditions do not vary drastically from the BOMEX Phase IV mean conditions. But it must be kept in mind that conditions in the tropics do not generally vary drastically over short periods and also that the small differences observed may well be those which at least partly determine whether or not cloud rings will form.

The BOMEX Phase IV mean surface air temperature-sea surface temperature difference at each of the five fixed ships is also obtained. The BOMEX Ship Station Surface Observations (1969) provides the twice- or 4-times-daily air and sea surface temperature observation data utilized in creating the Period IV mean differences. The resulting mean differences going from south to north show the largest values (-1.5°C , $T_{\text{air}} < T_{\text{sea}}$) at Oceanographer, a decrease to a minimum value (-0.4°C) at Discoverer and an increase to (-0.7°C) at Rainier. The specific observation time mean differences at each ship show a decrease from night to day, in keeping with the expected greater warming of the

air during the day compared to that of the ocean. Comparison of the July 18 values of the ($T_{air} - T_{sea}$) difference with the BOMEX Phase IV mean values of that parameter shows that at Oceanographer and Mt. Mitchell the July 18 and mean values are only slightly different, while at the three northern ships the mean ($T_{air} - T_{sea}$) values are significantly different than those on July 18. From Discoverer north to Rainier the mean differences display significant negative values, while on the 18th the differences display relatively small positive and negative values.

As discussed earlier a negative value of ($T_{air} - T_{sea}$) corresponds to an ocean-to-atmosphere heat flux. As seen from the BOMEX Phase IV mean differences, this condition prevails in the mean at all five fixed ship stations. On July 18 the upward heat flux is significantly occurring only in the Oceanographer and Mt. Mitchell regions (the latter near where the ring cloud pattern is present), while at the northern ships the flux is small and even downward at some locations. These comparisons appear to indicate that a positive correlation exists between ring cloud occurrence and upward heat flux related to a negative ($T_{air} - T_{sea}$) value, in that on July 18 ring clouds are present in regions of upward heat flux and are weakly or not present in regions of very small or downward fluxes and further that the upward flux is prevalent in all areas in the mean, making the North Grid regions on the 18th of July unfavorable for ring cloud occurrence compared to the South Grid region. From this it appears that significant sea surface-to-atmosphere heat flux is one of the necessary conditions for ring cloud occurrence.

Having compared the July 18 cloud ring occurrence day and the BOMEX Phase IV mean conditions of temperature and moisture, it is next desired to compare the BOMEX ring day thermodynamic situation with the ring region situations found by other ring cloud phenomena investigators who have been mentioned already in the ring cloud physical comparisons section. However, not all the studies of ring phenomena have included thermodynamic and/or dynamic analyses.

Table 4 presents a summary of the thermodynamic conditions accompanying ring cloud occurrences as found by the investigator(s) listed, including the BOMEX ring study. The dates and locations of the studies are the same as those listed in Table 3. Table 4 shows that general correlation exists between the BOMEX ring region conditions and those found by others. Ring occurrences are favored in synoptic scale anticyclonic regions. A dry, stable layer capping a moist rather unstable near-surface layer is common to all cases, as is an upward heat flux due to a warmer sea surface than atmosphere just above. The Ruprecht et al. (1973) investigation results related to the single ring occurrence in the ITCZ region are somewhat different from the above description in that the near-surface unstable layer is the least deep and the moist layer very deep compared to the other two case studies. The dry layer is also not as marked as in the other cases and occurs at a higher level. The soundings were obtained within and outside this ring as is discussed below. Krueger and Fritz (1961) note highest clouds where the inversion is highest and in this regard the table shows the middle latitude region discussed by Fritz, Krueger and others to have a lower stable layer in the mean than that prevalent in the BOMEX area. From Table 3 the cloud heights in the mid-latitude region

TABLE 4: CLOUD RING THERMODYNAMIC DESCRIPTION

Comparison of Various Investigation Findings

SOURCE/ INVESTIGATORS	DATA SOURCE(S)	UNSTABLE LAYER(S)	STABLE LAYER(S) ¹	MOIST LAYER(S)	DRY LAYER(S)
Loranger and Vonder Haar (Present, 1973)	Nimbus III SIRS-A, Fixed Ship Rawin- sonde and Sur- face observation	Dry Adiabatic, 1015 mb → 920 mb	Isothermal or in- version, 1 or 2 occur between 600mb and 800mb	Sfc to lowest stable layer	At and above lowest stable layer
Krueger and Fritz (1961), Fritz(1965) Hubert(1966)	Ship Radiosonde and sfc obs, Aircraft and dropsonde.	Near sfc dry ad- iabatic layer.	Inversion, occur between 700 mb and 900 mb.	Sfc to Inver- sion.	Above inversion
Ruprecht, et al., (1973)	Ship Rawin- and Radiosonde and sfc obs.	Dry abiabatic, 1015mb→965mb	Inversion or near isothermal, sev- eral occur, small between 500mb and 700mb	Sfc to ~600mb base of defined stable layer	In and above stable layer starting at ~575 mb.

TABLE 4 (cont)

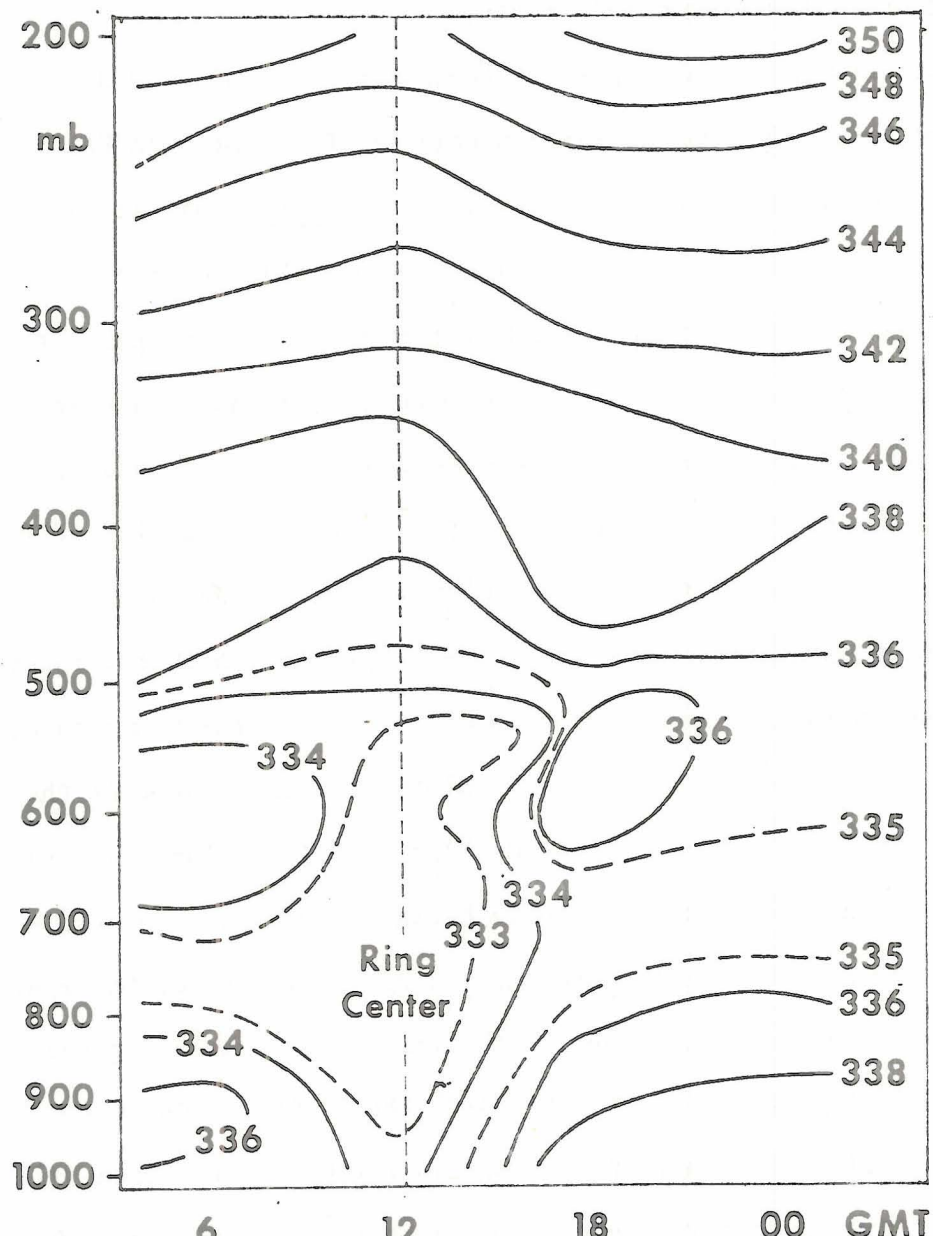
GENERAL LAPSE RATE	AIR-SEA TEMPERATURE DIFFERENCE, HEAT FLUX	RING CLOUD BASE C()=CALCULATED (TYPE) M()=MEASURED (TYPE)	MISCELLANEOUS CHARACTERISTICS	MISCELLANEOUS CHARACTERISTICS
Moist Adiabatic	$\sim 1^{\circ}\text{C}$, Sea sfc to Atmosphere	900 meters, C(LCL,CCL)	Occur in STHP anticyclone region, SW of Center	
Between dry and moist adiabatic	$\sim 3^{\circ}\text{C}$, Sea sfc to Atmosphere	600m-900m, M(aircraft)	Occur generally near S. of anti-cyclone center, behind cold front, ahead of warm front	Cloud thickest where inversion highest
Low levels, somewhat $>$ moist adiabatic; Moist adiabatic above	$\sim 2^{\circ}\text{C}$, Sea sfc to Atmosphere	700 m, C(LCL)	Occur in ITCZ region; soundings obtained inside and outside ring	

are lower than those in the BOMEK region, lending additional credence to the previously discussed subsidence-caused stability being the major factor governing the vertical extent of the ring cloud circulation and thus limiting cloud height.

The very important aspect of the Ruprecht et al. (1973) ring study on March 19, 1969 during the Atlantic Experiment (APEX) is that a ring cloud passed directly over the R. V. Meteor ship at ~1200Z on that day. This is an extremely lucky and valuable occurrence in that it provides the only known available ring scale data compared to the synoptic scale data available in all the ring studies discussed to this point. Radiosonde soundings were made inside and outside the ring as it passed over the ship and Fig. 19 displays the results of these soundings in terms of the equivalent potential temperature θ_e . This temperature parameter, which implicitly represents both the internal energy and moisture content of a parcel of air in the atmosphere, displays a marked minimum at constant pressure at the center of the ring cloud (~12Z) with highest values outside the ring. The lower values of θ_e inside the ring are seen to extend to 200 mb. The explanation for the reduced θ_e is the presence of drier air inside the ring than outside it and not lower ring-center temperature. Relating again to the only logical physical process which can be operating to produce the open cell ring cloud, that of upward motion in the cloud wall and subsidence in the central region, it is reasonable to assume that subsidence in the ring's central region is responsible for the observed dryness there. Also this subsidence further negates the aspect of net cooling in the ring central region unless there is a relatively very large radiational cooling there which is not very likely. In

OPEN CELL, 19. 3. 69

Equivalent Potential Temperature



ATLANTIC EXPEDITION 1969

Figure 19 APEX March 19, 1969 R.V. Meteor Equivalent Potential Temperature θ_e Time - Height Cross Section during Cloud Ring Passage over Ship Station (After Ruprecht et al, 1973).

regard to the above discussion the ring's vertical circulation can be equated in a very basic sense to that of a "miniature hurricane". This aspect deserves future consideration in regard to tropical disturbance evolution.

3.3 Dynamics Comparisons

The cloud ring dynamic situations are now compared in a manner similar to that used for the thermodynamics. The first comparison will again be that of the July 18 ring day conditions with the BOMEX Period IV mean winds and dynamics. As with the 12Z and 18Z fixed ship temperature and moisture means obtained from the BOMEX fixed ship rawinsonde data, the 12Z and 18Z mean winds, in terms of u and v components, at each fixed ship and 25 mb interval from 1000 mb to 300 mb are calculated. In contrast to the temperature and specific humidity data, no wind data elimination is done in obtaining the mean winds since the wind data appear smooth and no solid basis for elimination is present. Linear interpolation and the BOMEX Ship Station Surface Observations (1969) data are again utilized to fill in missing

winds at the 25 mb interval levels. The Rainier mean winds show the anomalous west wind for the whole Phase IV period and again these wind data are dropped from consideration. No Barbados 12Z or Rockaway 18Z mean winds are available due to lack of wind soundings at these times. The available mean wind data at 50 mb intervals for the four fixed ships (Rainier excluded) plus Barbados as input to the dynamics computation program discussed earlier yield the BOMEX Period IV mean horizontal divergence, vertical velocity and relative vorticity profiles in the same four triangular polygon areas used in the July 18 analysis.

Figure 20 displays wind soundings representative of the non-ring and near-ring areas at 15Z on July 18, along with the 12Z and 18Z BOMEX Period IV mean wind profiles at the same stations, Oceanographer and Mt. Mitchell. Again the 12Z and 18Z mean results together form an approximate 15Z mean. Comparison of the July 18 and mean soundings reveals that the Oceanographer displays the greater vertical shear of the zonal wind u in both the July 18 and mean soundings compared to Mt. Mitchell where the shear is relatively small, especially at 12Z in the mean. Oceanographer 1000 mb to 500 mb u component speed shear (absolute value) is on the order of 6 to 8 m/sec, while at Mt. Mitchell the shear is from 2 to 4 m/sec, the smaller values present in the means. These 1000 mb to 500 mb wind shears are of an increasing easterly wind aloft nature. In comparing the Mt. Mitchell-Discoverer region wind data, it is found that in the mean, as on July 18, the vertical shear is small. In general the 12Z and 18Z mean soundings display the same property as that found in the July 18 profiles, that of a S \rightarrow N low level east wind speed increase, little change in the middle levels, and a decrease in east wind speed in that

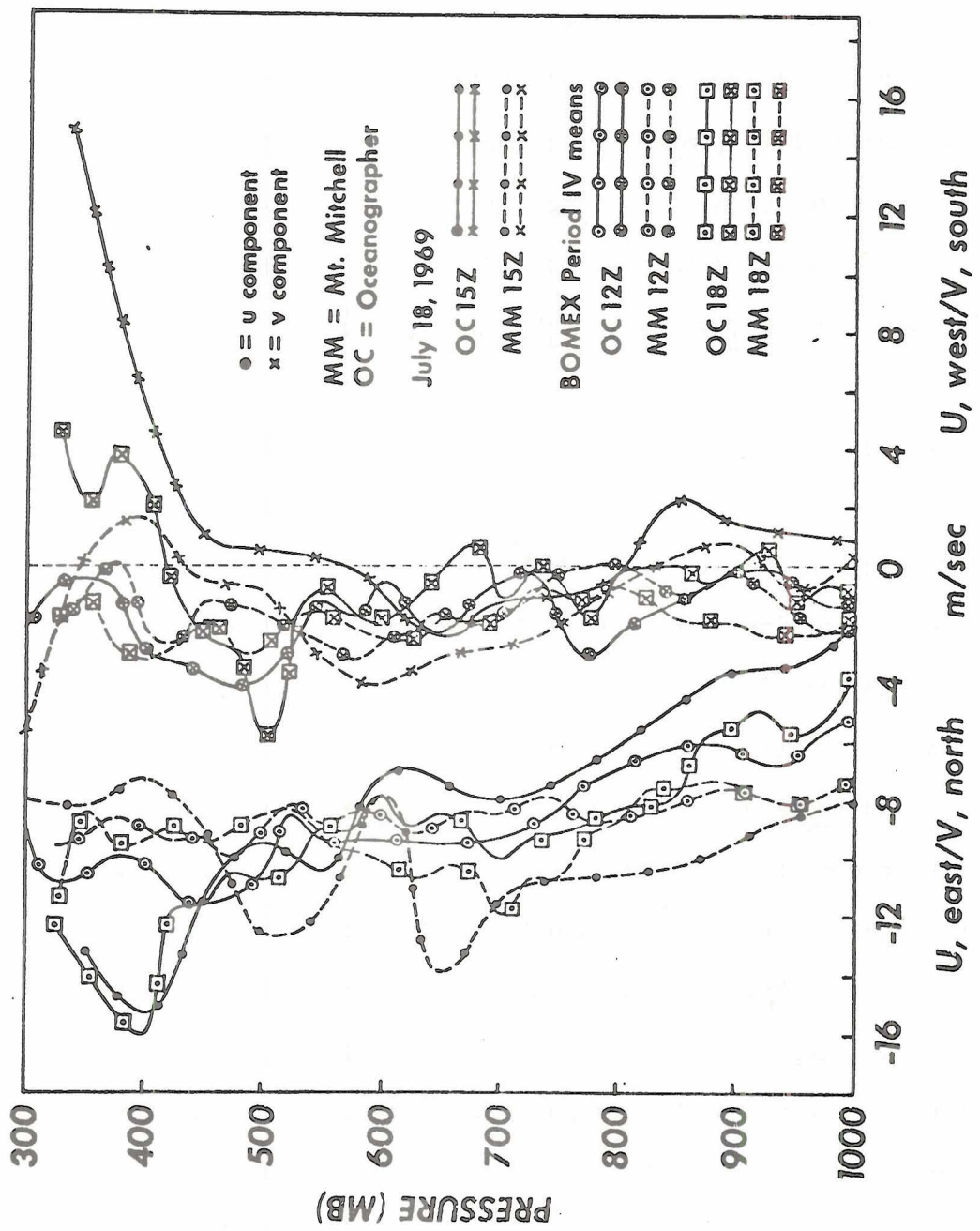


Figure 20 BOMEX July 18 and BOMEX Phase IV Mean Fixed Ship Rawinsonde Zonal (u) and Meridional (v) Component Winds Aloft Profiles.

direction at the higher levels to 300 mb. Rockaway in the mean shows the highest wind speeds as it does on July 18. The v components in all cases show little definition and cluster generally around zero with maximum values of several meters per second.

Therefore in all the July 18-BOMEX Period IV mean wind comparison shows that considerable similarity exists between the ring occurrence day and period mean conditions. Magnitude variations are the only significant differences. The July 18 ring and non-ring region profiles especially show good agreement with the BOMEX Period IV means for those areas.

The mean dynamic parameters following from the mean winds are next compared. The July 18 ring and non-ring region polygon horizontal divergence results, along with the BOMEX Period IV mean divergences for those regions, are displayed in Fig. 21. 12Z means for Polygons 1 and 2 are compared to 15Z July 18 results for those areas, due to the lack of mean divergence values resulting from missing 12Z and 18Z mean winds at Barbados and Rockaway, respectively. The figure shows that in the July 18 ring cloud area (Polygon 1) the earlier discussed near surface and higher level convergence and middle level divergence are present, while the mean for that area shows convergence prevalent at all levels. The July 18 non-ring area (Polygon 2) shows relatively deep convergence (1000 to ~700 mb) with divergence above prevalent in both the July 18 and period mean profiles which are thus quite similar except for some magnitudes which in turn are sensitive to the wind data used to derive the divergence values. These magnitudinal variations are generally on the order of a factor of 2 or 3 and thus are not extreme.

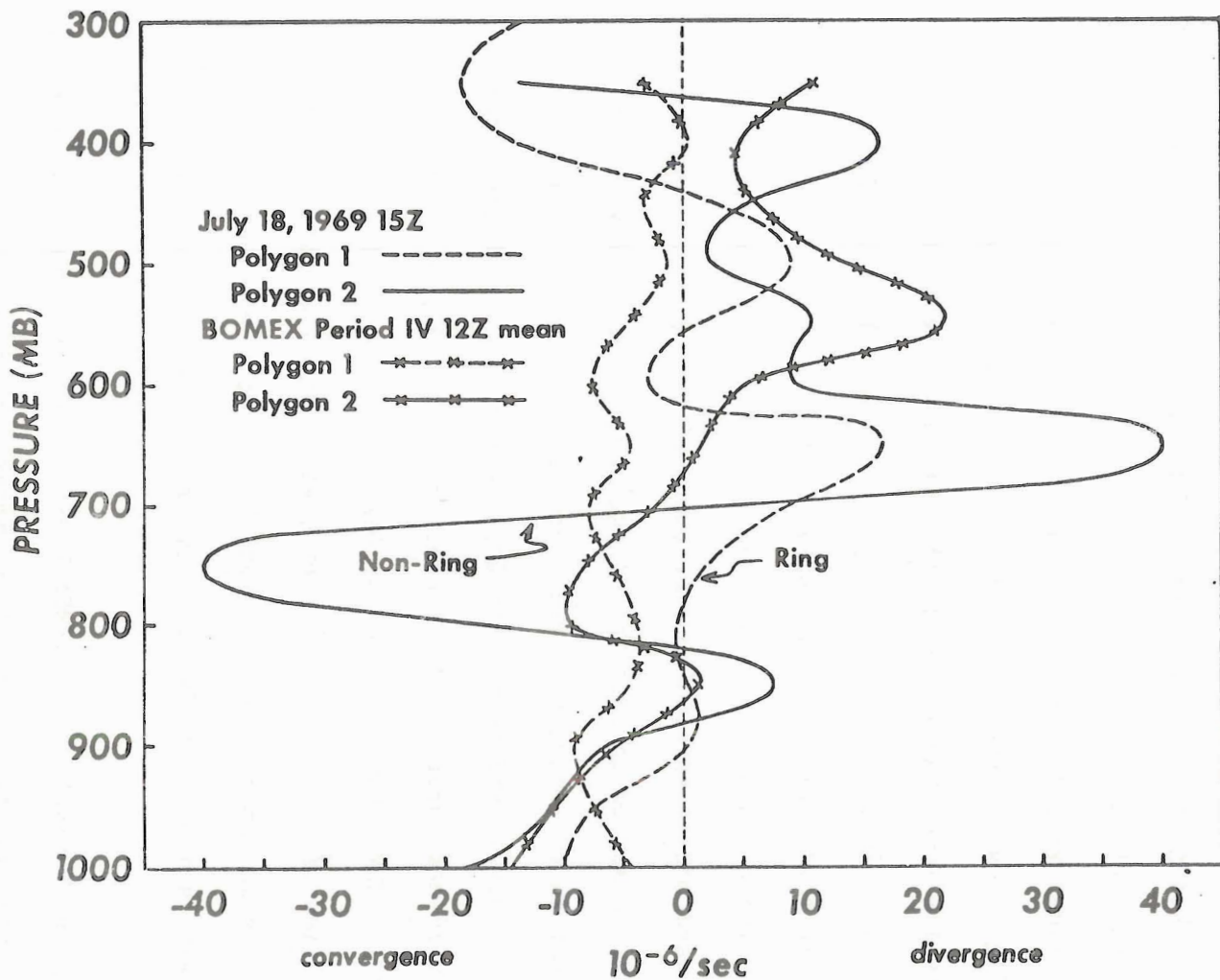


Figure 21 BOMEX July 18 and BOMEX Phase IV Mean Ring Study Area Horizontal Velocity Divergence Vertical Profiles Obtained Using Polygon Method.

It is also found that the Polygon 3 area displays a very similar profile on both July 18 and in the mean, that of divergence at all levels except for a small convergence in the near surface layers. Also Polygon 1 displays a significant similarity between the 12Z and 18Z means, this area being the only one where BOMEX Phase IV mean data are available at both times.

Vertical velocity profile comparisons for the same areas and times as in Fig. 21 are presented in Fig. 22. On July 18 upward motion prevails in the lower and higher levels with downward motion in the middle levels in the Polygon 1 ring cloud area, while the BOMEX Period IV mean in that area shows that upward motion prevails at all levels. In the Polygon 2 non-ring region both the July 18 and mean profiles show upward motion to ~450 mb with downward motion above that level. It is thus observed in both the divergence and vertical velocity profiles that in the Polygon 1 area there is considerable difference between the July 18 and mean conditions, while in the Polygon 2 region the July 18-mean profile differences are small. Again the Polygon 1 12Z and 18Z BOMEX Period IV means comparison shows similarity of the two profiles with a somewhat lesser upward motion magnitude at 18Z. Polygon 3 also shows some similarity between the July 18 and mean profiles, with slightly greater downward motion at the lower levels in the mean.

Figure 23 displays the BOMEX Phase IV relative vorticity comparisons for the same times and polygon areas considered in the preceding two figures. Polygon 1 (ring cloud occurrence region) shows cyclonic vorticity prevailing in the lower half of the troposphere on July 18 with anticyclonic vorticity above. The Polygon 1 BOMEX Phase IV mean

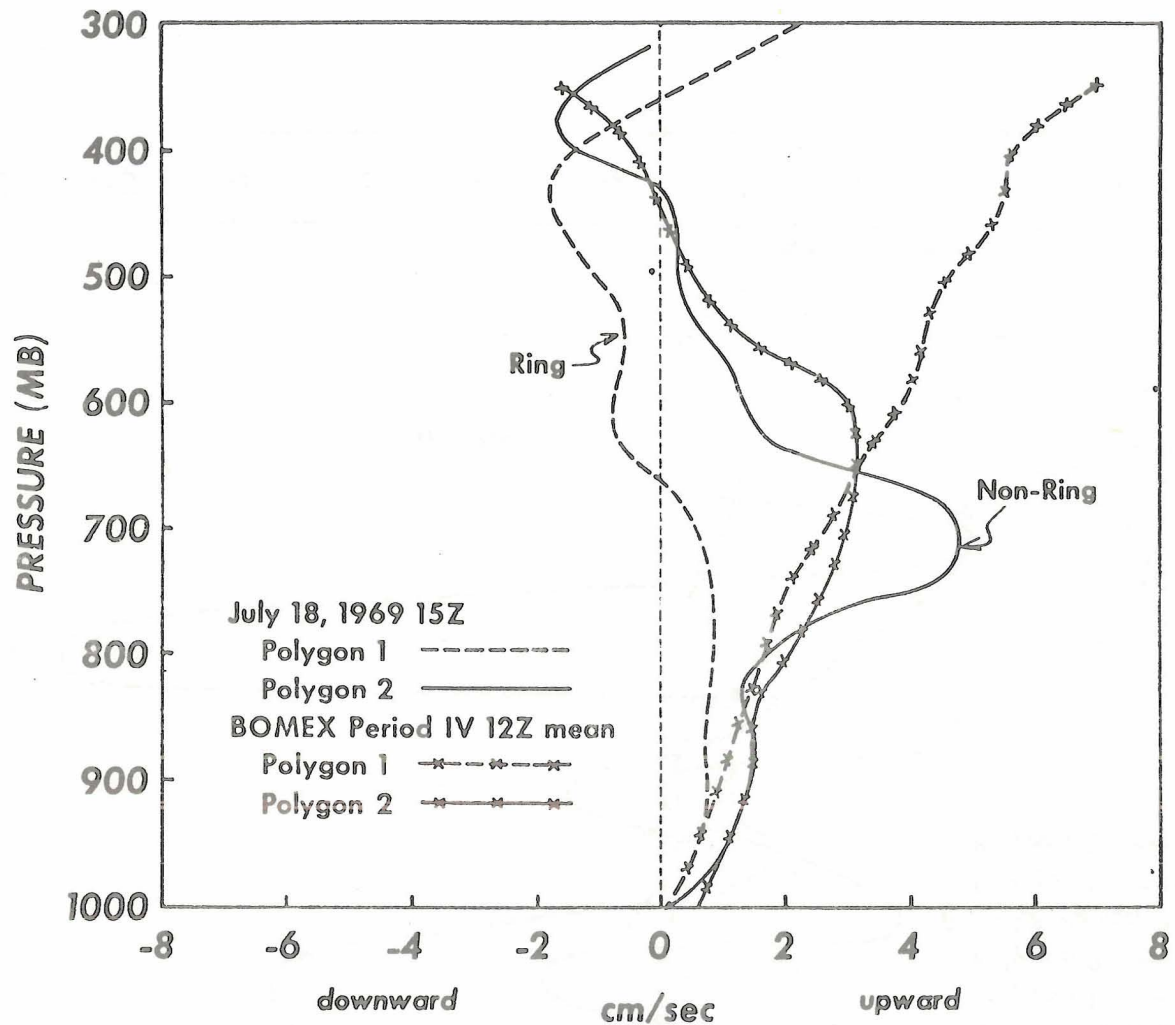


Figure 22 BOMEX July 18 and BOMEX Phase IV Mean Ring Study Area Vertical Velocity Vertical Profiles Kinematically Computed from Figure 21 Horizontal Divergence Profiles.

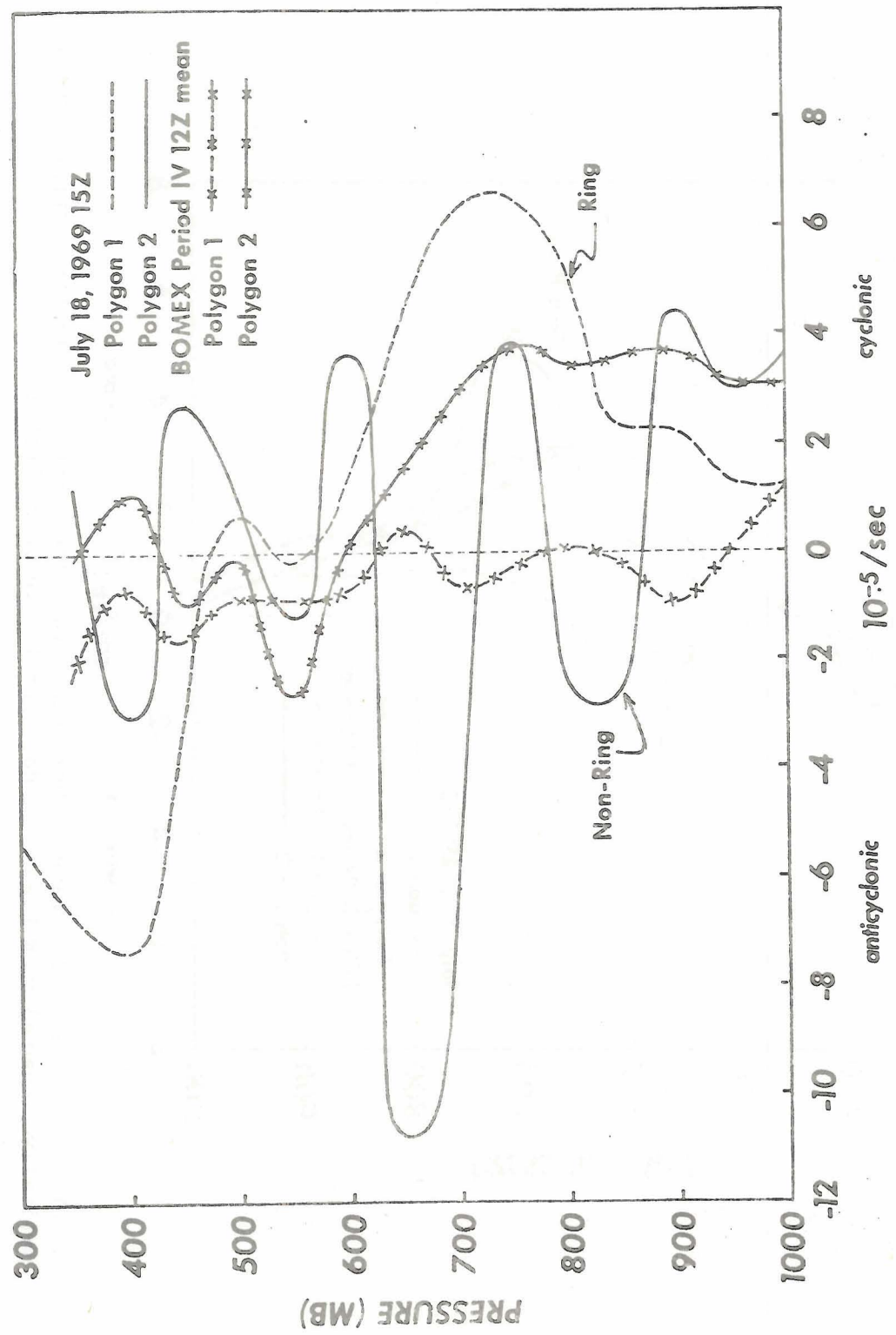


Figure 23 : Same as Figure 21 for Relative Vorticity.

profile shows general, but small, anticyclonic vorticity prevailing at all levels. The Polygon 2 (non-ring) region displays generally cyclonic vorticity in the low levels in both the July 18 and period mean profiles, but with some anticyclonic vorticity present in the middle levels on July 18 compared to cyclonic vorticity there in the mean. In the higher levels both the July 18 and mean profiles display vorticities fluctuating around zero. Thus in the case of relative vorticity both polygons 1 and 2 show notable differences between the July 18 and mean profiles. The Polygon 1 12Z and 18Z mean relative vorticity profiles again show considerable similarity. Polygon 3 displays a similar nature in both the July 18 and mean profiles, with a lower middle level cyclonic tendency on July 18 and anticyclonic values elsewhere in the two profiles.

The dynamic comparisons of ring occurrences studied by the investigators listed in Table 4 are confined to those of wind profiles, since the investigations other than the BOMEX effort covered the wind fields only with respect to magnitudes and shear and contained no related dynamic parameter studies. Figure 24 displays the ring region wind profiles from the BOMEX and two other investigations. The u component is used since it represents the major portion of the total wind prevalent in the investigation areas and is convenient. Also since the Krueger and Fritz (1961) discussion presents only a wind speed shear value of ~5 m/sec from surface to maximum cloud top (~3.6 km or 650 km), a straight line representing this shear is entered in Fig. 24. From the figure it is seen that the shears are generally the same in all the ring occurrences, with the lower 200 mb of the Ruprecht profile (personal

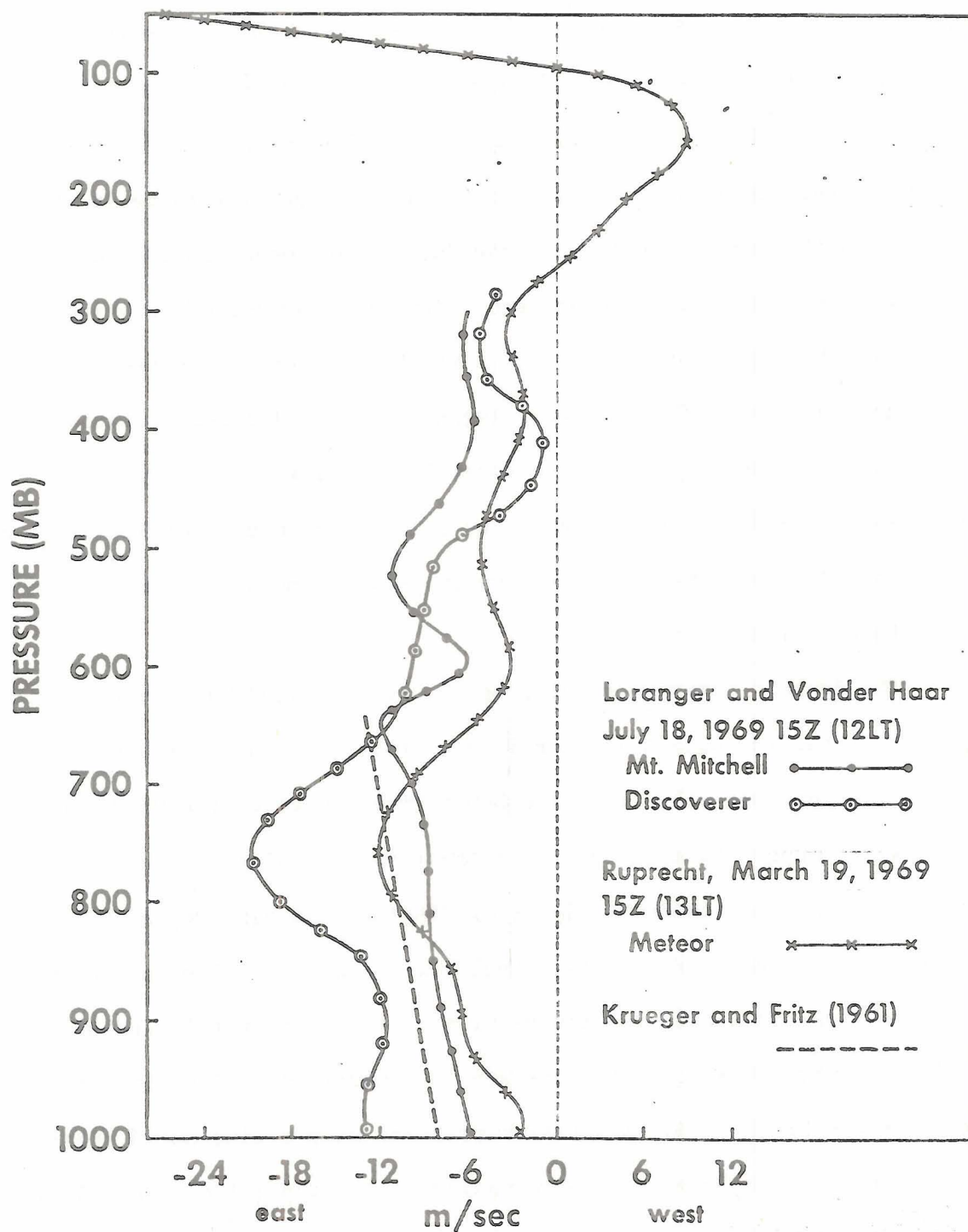


Figure 24 Zonal (u) Component Winds Aloft Profiles in Regions of Ring Cloud Occurrence as Obtained from Various Cloud Ring Investigations.

communication) showing the largest shear. The shears are all on the order of an ~5 m/sec east wind speed increase from 1000 mb to various levels between 500 and 750 mb, with a reversed shear above these maximum wind speed levels. Wind speeds are predominantly in the light category with a mean of ~10 m/sec. Thus over the lower half of the troposphere the vertical shear of the horizontal wind is small in the vicinity of all the investigated cloud ring occurrences. A small veering of the winds in the lowest kilometer or two of the atmosphere and a similar magnitude backing aloft in the ring cloud occurrence regions is also observed.

4.0 SUMMARY DISCUSSION AND HYPOTHESES

4.1 Cloud Ring System Composite Summary

From the foregoing sections a composite picture of ocean region convective cloud ring structures emerges. These "doughnuts", occurring singly or in multiple "honeycomb" patterns, consist of individual cumulus elements forming and decaying to produce the ring wall and a clear center area. The pattern persists for periods of time ranging from several to 8 hours with estimated longer durations. Single occurrences appear to be of shorter duration than multiple occurrences. The rings are found in both tropical and mid-latitude oceanic regions of undisturbed weather which is frequently associated with an anti-cyclonic synoptic weather pattern. Mean tropical rings possess diameters of 60-80 km, cloud wall widths of 14 km and cloud tops of 6-8 km, while mean mid-latitude rings show diameters of 50 km, cloud wall widths of 23 km and cloud tops <4 km. The theoretically important ring diameter to height ratio is on the order of 10:1 in the tropics and 30:1 in the mid-latitudes. From ring cloud vicinity synoptic scale wind field data tropical rings are found to travel with the mean wind in the lower 500 mb of the troposphere, correlating with the estimated cloud heights from radar echo data and inferred heights from synoptic scale thermodynamic sounding data.

From these latter data, ring cloud occurrence is correlated with a surface-based ~60 mb thick dry adiabatic lapse rate layer which is relatively moist, a relatively stable layer in the lower or middle levels (located higher toward the equator) with considerable drying at and above this layer, and a generally moist adiabatic lapse rate at other than these discussed levels. An atmosphere that is cooler than

the sea surface just below it, i.e., upward heat flux, prevails during ring cloud occurrences.

Winds in the vicinity of rings are on the order of 5 to 10 m/sec with a small vertical shear of <5 m/sec between surface and 500 mb. Horizontal easterly wind shears from south to north are on the order of 5 m/sec over 200 km, cyclonic at low levels (implying frictional convergence and CISK) and anticyclonic at high levels. Ring cloud vicinity wind field dynamics reveal the presence of low level convergence, upward motion and small cyclonic relative vorticity, while in the middle to some higher levels divergence, downward motion and anticyclonic vorticity prevails. From the above it is seen that a significant correlation exists between the observed wind field and calculated dynamics with regard to horizontal wind shears and correlation also exists between these dynamics and the thermodynamic structure in regard to moist, unstable and dry, stable layer occurrence and location.

In comparison with the BOMEX Phase IV several-weeks-period mean about the "honeycomb" ring cloud pattern occurrence day and in that same area, the ring occurrence day thermodynamics show considerable similarity to the mean thermodynamics with upward heat flux also prevalent in the mean. The ring occurrence day and mean wind profiles are also similar, while the mean dynamics show generally convergent, upward motion, and anticyclonic vorticity conditions prevalent at all levels (to 300 mb), differing considerably from the ring occurrence related conditions in that region. Atmospheric dynamics thus appear to govern in a large measure the occurrence of cloud ring structures. From the mean tropical atmosphere comparisons the cloud ring occurrence conditions lie intermediate between those associated with disturbed

and undisturbed weather situations. It is noted here that the major portion of the wind field and dynamic findings presented here is based on the BOMEX Phase IV ring cloud study. Also of importance is the fact that the ring cloud occurrence conditions are not equal to those in the mean (statistical) or else these patterns would be present either much less frequently or much more frequently than actually observed.

4.2 Cloud Ring Model Hypotheses

It is very important to understand, in regard to the cloud ring system description presented in the above summary, that the picture of the system presented by the combination of conditions attending cloud ring occurrence is the resultant of the interactions of all the atmospheric processes operating during cloud ring structure occurrence. In other words the meteorological conditions noted accompanying cloud ring occurrence represent the steady state and not necessarily causes of formation.

A hypothetical resultant conditions model of cloud rings or "open cell convection" follows from the cloud ring occurrence descriptions presented in this paper. From the observed physical form of the cloud ring structure it qualitatively and necessarily follows that upward flow is occurring where the convective clouds appear forming the ring wall and subsidence (or at least non-upward motion) is occurring in the ring center resulting in the clear area there. In regard to the "honeycomb" pattern of multiple ring occurrence, it is considered that an invisible atmospheric circulation pattern exists forming a "mold" in which the upward and downward motions are delineated and cloud

walls and clear areas, respectively, are the visible results of the molded circulation pattern. This "mold" forms in response to some favorable conditions and the disappearance of the visible pattern marks the demise of the "mold" circulation pattern due to loss of one or more of the conditions necessary for ring pattern maintenance. It is also important to note that there are necessary and sufficient conditions for ring cloud occurrence inherent in the above hypothesis and which are included in the following.

The model connection between cloud ring occurrence and synoptic scale meteorological parameter distributions is also hypothesized. This discussion is mainly related to tropical area cloud ring findings, but should be basically applicable to all cloud ring phenomena. The relatively moist near-surface dry adiabatic lapse rate layer, the upward flux of heat from the sea surface, and the low level convergence together imply potential instability and a trigger for its release. The presence of the moist and unstable near-surface layer, heated from below, allows convective activity to mainly initiate thermally with only very weak dynamic forcing present, as exemplified by the shallow and rather weak low level convergence that is observed in the vicinity of ring clouds. With the presence in the mean of the moist unstable near-surface layer and warming of the air from the sea surface below, the low level convergence "trigger" becomes one critical factor determining ring cloud occurrence. Due to the moist, thermodynamically unstable nature of the low level air mass in the regions where cloud rings are found, only a relatively weak mechanism is needed to trigger the release of the potential instability in this air mass as well as

bring it to condensation initially by lifting to the relatively low cloud base level of ~920 mb.

In regard to the cloud ring-air-sea interface heat flux relationship, a recent review of mesoscale cellular convection by Agee et al. (1973) presents the important result of a satellite cloud picture survey that open cell convection (cloud rings) occurs predominantly in the western regions of oceans (east of continents) where relatively warm currents are present with consequent ocean-to-atmosphere heat flux. This result agrees with the cloud ring findings discussed in this paper. Closed cells, on the other hand, are found to be favored in the eastern regions of oceans (west of continents) where relatively cold currents prevail and there is no significant upward heat flux. Thus all findings to the present indicate that upward heat flux from the ocean surface is a very necessary condition for cloud ring occurrence.

As is also observed, cloud rings are not favored in regions of deep convergence with its accompanying upward vertical motion field, generally associated with disturbed weather situations. Rings are favored in relatively undisturbed weather anticyclonic regions of middle level divergence and subsident motion, resulting in the observed stable temperature lapse layer occurrence in the middle or lower middle levels as well as the subsidence-caused drying at and above the stable layers. The subsident vertical motion is a "lid" mechanism which contains the vertical circulation within a defined layer, as well as allows the thermal structure near the surface to be maintained. With deep convergence and upward motion to high levels, the circulation covers larger horizontal areas with strong inflow from these areas, negating the organized mesoscale up-down circulation of the cloud ring pattern.

and resulting instead in a large disturbed weather region such as a cloud cluster.

That the stable layer "lid" associated with anticyclonic subsidence is an important factor in ring occurrence is shown by the observed lower ring cloud heights in the middle latitudes where the inversion is located at a lower level than it is in the tropics. In both regions the ring cloud tops are observed to be correlated with the drying aloft, growth of the clouds into the dry layer being inhibited by evaporative and detrainment processes along with the stabilization which is often not excessive. In regard to this latter point, radiative processes are also present with infrared energy net outward flux at the levels of the subsidence and drying, implying radiative cooling of relatively large magnitude there and thus partial cancellation of the stabilizing effect of the subsident warming.

And the final factor in the cloud ring model is the small vertical shear of the horizontal wind which allows the relatively slow vertical circulation pattern to be maintained in the vertical without being torn apart, tilted excessively from the vertical, or excessively ventilated by environmental air resulting in elimination of the ring cloud wall local concentrations of heating and moisture. Associated with this factor is the overall rather light wind speed which is an expected occurrence in relatively undisturbed weather situations. Strong winds are generally associated with a disturbed weather situation of some kind.

In regard to the low level convergence and higher levels divergence with subsident motion there and the small vertical shear of the horizontal wind prevalent in ring cloud occurrence areas, comparison

with Williams' (1970) and other investigators' cloud cluster and clear area meteorological conditions indicates that the cloud ring associated conditions lie intermediate between cloud cluster disturbed weather and clear area undisturbed weather situations. Thus the ring clouds possibly represent a phase in a transition from clear weather to disturbed weather occurrence. Further there is noted a less organized and/or short lived ring cloud pattern (single occurrence frequently) when a model parameter or two are marginal or when a single parameter value is sufficient to compensate for the near absence of some other necessary parameter configuration. In general the cloud ring model thermodynamics are those near the average for the area, but the dynamics show considerable difference between cloud ring occurrence and mean conditions. This seems to indicate that the dynamics are generally the critical factor in determining whether or not cloud ring patterns will occur. The ring and non-ring region meteorological parameter comparisons for the July 18 case study day also generally demonstrate the validity of the above conclusion.

In all, then, the model of the cloud ring is that of a circulation pattern delicately balanced, favored by light wind and small vertical shear conditions, weak wind dynamics fields (low level convergence) associated with relatively undisturbed weather situations and containment of the ring pattern circulation within a limited vertical extent of the atmosphere based at the surface, with moist, unstable conditions at and near the ocean surface which is in turn heating the boundary atmosphere. Significant deviation from these model conditions results in destruction of the delicate balance needed to maintain the cloud ring pattern circulation.

5.0 CONCLUSIONS

To conclude this discussion of cloud ring (open cell) convection systems, the present understanding of these systems is summarized in Table 5. This summary displays the understanding in terms of three categories: (1) Confident; (2) Preliminary; and (3) Unknown. The Confident category includes ring system findings that are based on a number of investigations and which show significant agreement in these studies. Findings which are based generally on a single case study or are only initially observed but not specifically investigated at present are included in the Preliminary knowledge category. Knowledge desired about the ring systems which is not at present available is included in the Do Not Know category. Table 6 presents a summary of the similarities and differences between tropical and mid-latitude cloud rings. In the instances where data are not available for both types of rings, comparisons cannot be made.

The information contained in the Confidently and Preliminarily known columns of Table 5 is a general summary of the findings in the investigation of cloud ring phenomena discussed in this paper, more specifically detailed in the previous sections. The major portion of ring cloud thermodynamic and dynamic information is based on fixed ship station synoptic scale data and this information is so indicated in the table. The major portion of cloud ring physical description information is obtained from satellite and weather radar observation data. Findings based on tropical region investigation only are also indicated. It is considered here that the investigation of more ring cloud pattern occurrences, especially on the BOMEX days, will provide

TABLE 5 CLOUD RING SYSTEM: PRESENT UNDERSTANDING

KNOW WITH CONFIDENCE	KNOW PRELIMINARILY	DO NOT KNOW
Convective cloud ring pattern (cloud wall, clear center) exists (well-defined) for a significant period of time.	Multiple ring occurrences (honeycomb pattern) are of longer duration than single isolated occurrences.	Characteristics, especially magnitude, on the ring cloud pattern mesoscale of thermodynamics, dynamics, and circulations.
Sense of ring pattern circulation: upward motion in cloud wall, downward motion in clear center area.	Occurrence in relatively undisturbed weather regions (anticyclonic). (S)	Energy transfer and conversion processes in and around ring patterns.
Multiple (honeycomb) and single ring occurrences.	Pattern exists during nighttime hours. (T) Brief occurrence over tropical land areas.	Precipitation characteristics of ring clouds.
Occurrence in tropical and middle latitude ocean regions in various seasons.	Occur predominantly on west sides of oceans.	Critical parameters and their magnitudes for ring cloud formation and existence.
Moist, unstable lapse rate in lowest levels with middle level stable layer and considerable drying above it. (S)	Relative dryness in ring center compared to exterior regions indicative of subsident motion in center. (T)	If ring circulation pattern is of local or advective origin.
Temperature gradient related sea surface-to-atmosphere heat flux. (S)	Cyclonic shear of the horizontal wind in the low levels with anticyclonic shear of that wind in the high levels. (S,T)	If and where there are favored regions of formation and if and when there are favored times of formation and occurrence.
Ring cloud heights positively correlated with synoptic scale middle to low level stable layer height.	Movement with the mean wind in the cloud depth layer. (S,T)	Model of atmospheric ring cloud pattern origin.
Small vertical shear of the horizontal wind. (S)	Low level convergence and upward motion with middle to higher level divergence and subsident motion. (S,T)	Interaction between ring pattern mesoscale and smaller cumulus scale and larger synoptic scale processes.
Moist adiabatic lapse rate in the mean to the tropopause. (S,T)	General cyclonic relative vorticity, small in low levels. (S,T)	
In comparable (data available) respects BOMEK July 18, 1969 and other investigated ring patterns are significantly similar.	No unique temperature profile in upper troposphere, isothermal to inversion lapse rate above tropopause into stratosphere. (S,T)	(S) Synoptic scale findings (T) Tropical region findings
	Thermodynamic conditions on occurrence days very similar to mean conditions. (S,T)	
	Dynamic conditions on occurrence days differ significantly from mean conditions. (S,T)	

TABLE 6 COMPARISON AND CONTRAST OF
TROPICAL AND MID-LATITUDE CONVECTIVE
CLOUD RINGS

SIMILARITIES	DIFFERENCES
<p>Roughly circular convective cloud wall surrounding a clear center; cloud wall cumulus elements growing and decaying.</p> <p>Ring pattern remains defined over significant time intervals.</p> <p>Occurrence favored in undisturbed weather regions.</p> <p>Moist and relatively unstable boundary layer capped by middle level stable layer with marked dryness.</p> <p>Ring cloud and stable layer heights positively correlated.</p> <p>Occur in regions of cooler air overlying warm ocean with consequent sea surface \rightarrow atmosphere sensible heat flux.</p> <p>Small vertical shear of the horizontal wind prevalent, $\leq 5\text{m/sec}$. between 1000 mb and 500 mb.</p> <p>Single and multiple ring occurrences.</p>	<p>Mean Diameters: (T) 60-80 km, (ML) 50 km.</p> <p>Mean Cloud Height: (T) 6-8 km, (ML) <4 km.</p> <p>Diameter-Height Ratio: (T) 10:1, (ML) 30:1.</p> <p>Cloud Wall Width: (T) 15 km, (ML) 25 km.</p> <p>Stable layer height: (T) 500 mb-800 mb, (ML) 700mb-900 mb.</p> <p>(T) = Tropical Findings (ML) = Mid-Latitude Findings</p>

sufficient information to permit shifting the Preliminary knowledge over to the Confident category with regard to tropical cloud ring occurrences. Middle and higher latitude studies will fill in the information gap in these regions, especially in regard to dynamics. The additional investigations will also add to the confidence in the presently accepted findings.

In addition to providing supplementary information with regard to the present and rather meager understanding of convective cloud ring systems, the further investigations can provide data on the Unknown factors related to ring cloud formation and occurrence. The major Unknown factors are listed in the Do Not Know column of Table 5. The first major need in regard to the Unknown cloud ring factors is to obtain data on the space scale of the rings themselves, this mesoscale information to include thermodynamic, dynamic and energy measurements along with surface and atmosphere interactions including precipitation. Only with these data available can the cloud ring pattern itself be thoroughly understood and its interaction with the atmosphere as a whole be deduced. The precipitation information (radar methods?) would be most useful for use in inferring energy transport and conversion where the flux type measurements may be difficult.

Another major Unknown is whether the ring circulation pattern moves into an area from another area of formation a significant distance away or whether it forms in a given area by virtue of the coming together of the necessary and sufficient conditions for formation and occurrence in that area at a given time. This latter aspect has an analogy in the inception of severe storms in the middle latitudes where such

factors as low level moisture, middle level dry line and upper level jet coincide in a given manner to initiate the tornado or other severe weather phenomena in the given area and at the given time of necessary and sufficient condition coincidence. In regard to the local or advective nature of ring cloud patterns, especially the tropical ones, there is speculation that some tropical easterly disturbances may travel considerable distances, from the Indian Ocean or Africa land mass into and across the Atlantic Ocean and even into and across the Pacific Ocean and further even circumnavigate the world in the easterly flow. The above would allow for the possibility: (1) of the cloud ring associated circulation patterns travelling over significant distances from remote formation areas such as Africa in the case of the BOMEX ring occurrence; or (2) that certain of the cloud ring associated parameters are advected into a given favorable region from a distance resulting in cloud ring circulation initiation. Thus there is the great need to determine the critical factors in cloud ring formation and existence in order to subsequently discover where the various parameters originally are present and how they interact in ring system formation and perpetuation. At present the author's speculation is that the cloud ring pattern is of a local nature, possibly with some advected properties, due to the rather delicate nature of the pattern organization. Further in regard to formation and occurrence of ring cloud patterns, there is the question of whether or not there are favored regions (affirmative according to Agee et al., 1973) and/or times of formation and occurrence, which if there are would add to the knowledge of critical formation and existence factors.

Combining the results of the above discussed needed investigations when they become available will lead to the eventual formulation of a basically complete model of open cellular convection systems. This "portrait" will include the nature and magnitude of ring cloud system interaction with the atmosphere as a whole and will provide knowledge of the cloud ring pattern mesoscale circulation's role in the hierarchy of atmospheric scales of motion in the transport of energy and momentum. From this knowledge follows the ability to include, by some appropriate method such as parameterization, the cloud ring systems in the numerical models of various kinds, diagnostic or prognostic, general circulation or energetics. (These above form the ultimate goal of this investigation of cloud ring systems as stated in the Introduction to this paper). And further, only when the sum total of atmospheric processes is accounted for as accurately as possible in the numerical and other models will the output of those models accurately represent the real atmosphere. In all, this and future investigations will lead to a better understanding of the nature of these most interesting and intriguing doughnuts in Nature's teacup.

REFERENCES

1. Agee, E.M., T.S. Chen and K.E. Dowell, 1973: A Review of Mesoscale Cellular Convection. Bulletin of the American Meteorological Society, 54, 10, October.
2. Air Weather Service, 1965: General Application of Meteorological Radar Sets, Technical Report 184, U.S.A.F., Scott AFB, Ill., April.
3. Atkinson, G.D., 1971: Forecasters' Guide to Tropical Meteorology, Technical Report 240, Air Weather Service, USAF, April.
4. Braham, Jr., R.R., L.J. Battan, and H.R. Byers, 1957: Artificial Nucleation of Cumulus Clouds. Meteorological Monographs, 2, 11, July.
5. Charney, J.G. and A. Eliassen, 1964: On the Growth of the Hurricane Depression. Journal of the Atmospheric Sciences, 21, 1, Jan.
6. De La Moriniere, T., 1972: BOMEX Temporary Archive Description of Available Data. NOAA Technical Report EDS 10, January.
7. Fernandez - Partagas, J.J. and M.A. Estoque, 1970: A Preliminary Report on Meteorological Conditions During BOMEX, Fourth Phase (July 11-28, 1969), Rosenstiel School of Marine and Atmospheric Sciences, Division of Atmospheric Science, University of Miami, Coral Gables, February.
8. Fritz, S., 1965: Local Circulation As Seen from Satellite cloud Pictures. Unpublished Paper to appear in Proceeding of the Workshop on the Use of Satellite Data in Meteorological Research, National Center for Atmospheric Research, Boulder, Colorado, August.
9. Goddard Space Flight Center, 1967-70: Meteorological Data Catalog for the Applications Technology Satellite, ATS Project, Greenbelt, Maryland.
10. Hubert, L.F., 1966: Mesoscale Cellular Convection. Report Number 37, Meteorological Satellite Laboratory, Washington, D.C., 68 pp.
11. Krueger, A.F. and S. Fritz, 1961: Cellular Cloud Patterns Revealed by TIROS 1. Tellus, 13, 1, pp. 1-7, February.
12. Loranger, D.C., 1974: Convective Cloud Ring Structures in the Tropical Atlantic. Master's Thesis, Department of Atmospheric Science, Colorado State University, Fort Collins, Colorado.

13. Madden, R., E. Zipser, E. Danielson, D. Joseph, and R. Gall, 1971: Rawinsonde Data obtained During the Line Islands Experiment. Volumes I and II, National Center for Atmospheric Research, Boulder, Colorado, February.
14. Oort, A. and E. Rasmusson, 1971: Atmospheric Circulation Statistics NOAA Professional Paper 5, U.S. Department of Commerce, Rockville, Maryland, September.
15. Peekna, S.K., R.J. Parent, and T.H. Vonder Haar, 1970: Possibilities for Quantitative Radiance Measurements in the 450-650 nm Region from the ATS-1 Satellite, Measurements from Satellite Platforms, University of Wisconsin, Madison, August.
16. Prospero, J.M. and T.N. Carlson, 1971: Radon-222 and African Dust in the North Atlantic Trade Winds. BOMEX Bulletin #10, The BOMAP Office, ESSA, Rockville, Maryland, June.
17. Reynolds, D. and T.H. Vonder Haar, 1973: A Comparison of Radar-Determined Cloud Height and Reflected Solar Radiance Measured from the Geosynchronous Satellite ATS-3. Unpublished paper, Department of Atmospheric Science, Colorado State University, Fort Collins, December.
18. Ruprecht, E., L. Bruer, K. Bucher, E. Scheidtmann, and W. Zack, 1973: Radarbeobachtungen der Konvektionsgebiete im Bereich der Inner-tropischen Konvergenzzone über dem aquatorialen Atlantischen Ozean. Meteor Forschungsergebnisse Reihe B.
19. Sikula, G.J. and T.H. Vonder Haar, 1972: Very Short Range Local Area Weather Forecasting Using Measurements from Geosynchronous Meteorological Satellites. Atmospheric Science Paper #185, Department of Atmospheric Science, Colorado State University, Fort Collins, April
20. U.S. Department of Commerce, 1969: BOMEX Preliminary Data, Volume 1, Ship Station Surface Observations, BOMAP, ESSA, Rockville, Maryland, December.
21. Vonder Haar, T.H., K. Hanson, V. Suomi, and U. Shafirir, 1968: Phenomenology of Convective Ring Clouds in the Tropics Derived from Geosynchronous Satellite Observations. Preprint from Proceedings of the International Conference on Cloud Physics, Toronto, Canada, August.
22. Vonder Haar, T.H., and E. Smith, 1971: Vorticity and Divergence Computations from Cloud Displacements. Measurements from Satellite Platforms, University of Wisconsin, Madison, August.
23. Williams, K.T., 1970: A Statistical Analysis of Satellite Observed Trade Wind Cloud Clusters in the Western North Pacific. Atmospheric Science Paper #161, Department of Atmospheric Science, Colorado State University, Fort Collins, June.

24. Private Communication with Dr. Thomas Vonder Haar regarding the information relating to the satellite systems and University of Wisconsin Procedures.
25. Personal Communication with Dr. E. Ruprecht regarding wind profile and lifetime estimate details of Meteor cloud ring passage on March 19, 1969, as well as Selenia METEOR 200 radar characteristics.

APPENDIX A

ATS III CAMERA SYSTEM TECHNICAL ASPECTS AND DATA PROCESSING

I. Analog to Digital Data Conversion and Use

The preparation of the digital data tapes (used in this study) from the analog data tapes was done at the University of Wisconsin and utilized a linear conversion between the analog data voltage outputs of the camera-data signal transmission system and a set of digits representing those voltage outputs.

The conversion was such that a 500 millivolt output was assigned a digital value of 255 and other outputs lower than this were given digital values in the ratio of these two numbers. The 500 mv output (255 digital count) was considered the highest value that would be likely to result from measuring cloud reflected energy. This aspect is connected with the fact that the ATS III MSSC system has the provision for system voltage gain setting changes to allow for measurement of a wide range of earth surface and cloud reflectivities. The variable settings allow compensation for very bright reflectors to prevent system saturation and limit digital values to 255 at 500 mv system output. Further the variable settings allow for various output voltage values and corresponding digital values to represent the same reflected energy input. This point must be kept in mind when using ATS digital data in analyses, especially comparative studies.

With the digital data magnetic tapes available and also gridded with respect to latitude and longitude, computer input of these will result in a printed array of numbers from 1 to 255 representing the

various magnitudes of energy reflected from surfaces at or near earth. A map is thus obtained of the bright and dark areas, as in the photographs, but in much more detail and in which large digital values represent bright or highly reflective areas and small digital values represent dark or slightly reflective areas. It must be remembered that for the major portion of the ATS III satellite lifetime, including July 18, 1969, the reflected energy measured is comprised of only the "green channel" portion of the solar spectrum. Also the ATS III ground resolution is ~2 nautical miles while the digital data resolution is ~3 nautical miles. Further in Peekna et al. (1970) is discussed the ATS III MSSC aspect of non-uniform response across its field of view. Only reflective elements of 10 n.m. diameter or more are well represented in the picture and digital data; smaller elements are generally not correctly displayed.

II. ATS III Digital Data Normalization Procedure

In order to compare space-time span ATS III (or other satellite) cloud picture data with respect to only cloud, ocean and land surface differences themselves, two factors related to the camera system and reflected energy input must be considered and compensated for. The first factor is the variable voltage gain setting provision in the ATS III MSCC camera and ground receiver system. This provision allows for measurement of a wide range of reflected energy magnitudes or reflective element brightnesses without saturation of the system occurring. The variable gain factor leads to ambiguity in the actual reflectivity that is being represented by a given digital data value. This factor is important in studies of both actual and relative reflected energy; the latter is the nature of the ring cloud study presented in this paper. Thus some common reference basis must be found to enable quantitative and comparative reflected energy studies to be accomplished. The pre-launch calibration reference state of the ATS III camera system provides a very satisfactory common reference basis for any desired studies. Reference to the calibration state is necessary only for quantitative reflected energy studies. Any common gain state of a set of ATS III pictures allows for relative reflected energy comparison of all such data.

The method for accomplishing the voltage gain portion of the "normalization" consists of finding the digital value which a given reflective element's brightness would be represented by when the measurement of its reflected energy is made in a reference voltage gain state. Mathematically this reference state digital value D is given by:

$$D = \left[\frac{1}{G_{s/c}} \quad \frac{1}{G_g} \right] D'$$
[A-1]

where D' is the given digital brightness value and $G_{s/c}$ and G_g are the spacecraft camera system and ground receiver system voltage gains, respectively. Voltage gain is defined as the ratio of the given voltage in a system component during a picture-taking period to the reference state voltage in that component. For all pictures being considered the quantity in brackets in Eq. [A-1] is calculated for each picture and the given digital values in that picture are multiplied by that quantity to yield the reference state picture. All pictures so treated are then comparable with respect to the camera-transmission system. But there is the second factor regarding comparison which must be considered before the pictures are truly comparable.

This second factor actually consists of two parts. Part 1 is the varying reflected energy from surfaces due to the varying sun-object geometry which occurs over the space and time of the pictures. Thus due to this fact and the fact that the desire is to compare pictures only with respect to the differences in the reflective surfaces themselves, all pictures must be referenced to a common set of space-time conditions. This "geometry" normalization is based on a discussion contained in a paper by Sikula and Vonder Haar (1972) where another study was done over space and time, presenting the need for a common reference for the digital data in order to make valid picture comparisons. However, Part 2 of the second factor enters into the normalization procedure here from Sikula and Vonder Haar's discussion. This part relates to the fact that clouds, ocean and most real surfaces

are not Lambert reflectors and thus there is varying reflected energy from these reflectors depending on the sun-object-satellite geometry. Thus we must take the position of the satellite (observer) at various space-time points into account in the normalization procedure so as to complete the reduction of the pictures to a common basis. It is important to undersatnd that the basic need for normalization comes from the sun-object geometry variations and not from the isotropy-anisotropy of reflective surfaces. Even if a surface were an isotropic reflector, normalization would be necessary in order to compare the pictures. However in this case the normalization would be complete with consideration only of Part 1. Part 2 considerations are necessary to complete normalization when surfaces are anisotropic.

While the normalization procedure used here is a mathematical operation, the physical meaning can be best understood by a simple analogy. First measure the reflected radiation from a given cloud or ocean element and note the digital value obtained. Then apply the chosen normalization conditions to the cloud or ocean element, measure the reflected energy, and note this digital value. The ratio of the second digital value to the first is the "normalization" factor which references that element to the normalization basis. However in regard to referring a reflective element of the normalization conditions, this is not really possible in actual analysis and the normalization reflected energy cannot be obtained for use in the mathematical equations. Thus a "reflective model" for clouds and ocean, based on Nimbus 3 data and discussed by Sikula and Vonder Haar (1972), is used to relate the reflected energies to the sun-object-satellite geometry

angles which are known for both given and normalization reference conditions. The ratio procedure would be repeated for all reflective elements of interest and then all the elements would be comparable. Variations in digital value would be only the result of element differences themselves.

The mathematics of the ATS III digital data normalization procedure from Sikula and Vonder Haar (1972) is based on the following equation relating digital value output to reflected radiance input to the camera:

$$D = K_1 K_2 N_r = K_1 K_2 \rho H_i \cos \zeta \quad [A-2]$$

where K_1 and K_2 are constants; K_1 is the voltage output to digital value conversion factor of 255 digital counts equivalent to 500 mv output and thus equals 0.51. Note that this value is constant for all ATS III pictures digitized at the University of Wisconsin. K_2 is the factor which relates the voltage output to the reflected radiance input and this factor includes the camera system voltage gain factors discussed previously and thus this "constant" is only a constant for a particular picture with its particular gain settings or for all pictures which are at a common gain setting. The voltage output-radiance input conversion is obtained from the calibration and gain setting data obtained before the satellite launch. N_r is the reflected radiance entering the camera, which radiance can be rewritten as shown in Eq. [A-2]. H_i is the solar constant for the wavelength or spectrum band under consideration, ζ is the solar zenith angle, and ρ is the bi-directional reflectance which is defined as the ratio

of reflected radiation in a particular direction to incident radiation from a particular direction. Therefore ρ is the anisotropy descriptor for the particular reflective element under consideration. Thus ρ and N_r are functions of ζ , the solar zenith angle, θ , the satellite zenith angle, and ψ , the relative azimuth angle of the sun and the satellite. These three angles (ζ, θ, ψ) are just the definers of the sun-object-satellite geometry and Fig. A1 diagrams this geometry. Next Eq. A-2 is defined for both the individual given cloud or ocean point and normalization reference point by assigning the unprimed value equation to the normalization space-time point and primed value equation to the given element space-time point. The latter becomes:

$$D' = K_1 K_2' \rho' H_i \cos \zeta' \quad [A-3]$$

Then the ratio of Eq. A-2 to Eq. A-3 gives the normalization factor, n , for a given cloud or ocean element:

$$n = \frac{K_2}{K_2'} \frac{\rho}{\rho'} \frac{\cos \zeta}{\cos \zeta}, \quad [A-4]$$

However since all pictures with various gain settings are reduced to a common one or the pictures are already in that state and also since the same gain conditions are used at the normalization point as in the gain-normalized pictures, then K_2 and K_2' are equal and thus:

$$n = \frac{\rho}{\rho'} \frac{\cos \zeta}{\cos \zeta}, \quad [A-5]$$

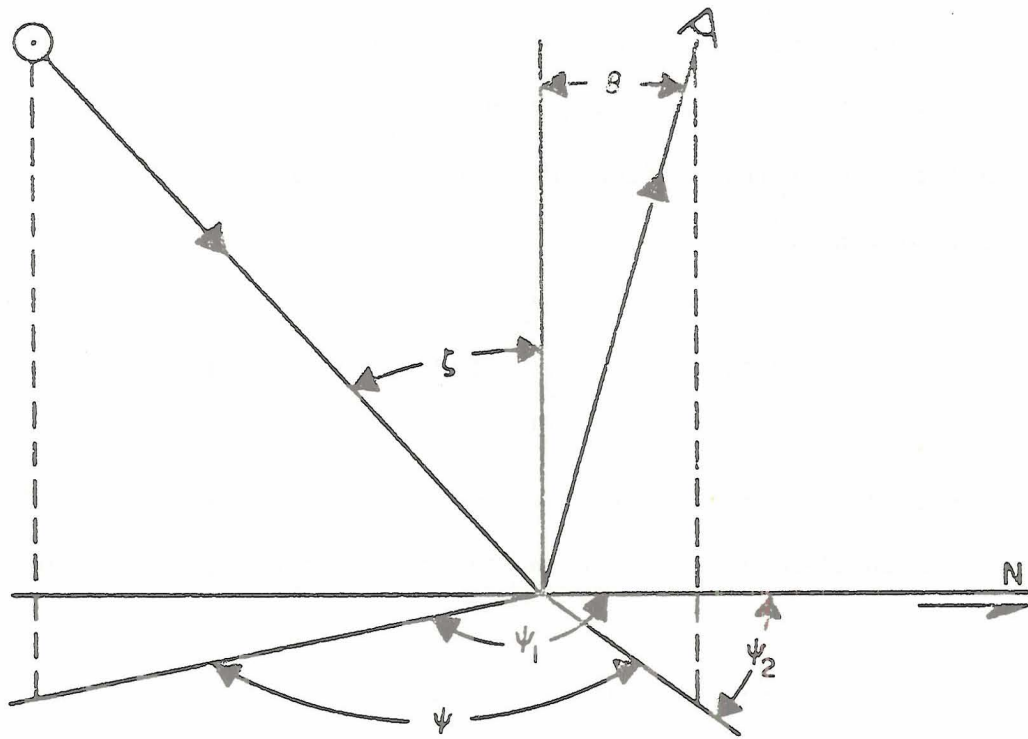


Figure A1 Sun - Reflective Element - Satellite Geometry (After Sikula and Vonder Haar, 1972).

But since the normalization point bi-directional reflectance for the desired cloud or ocean elements cannot be obtained because no observations were made of the elements in that normalization state, then the ratio of ρ to ρ' must be obtained from some equivalent expression. This is done by utilizing the Nimbus 3 cloud or ocean "model" presented in the normalization discussion by Sikula and Vonder Haar (1972). The factors $r(\zeta)$ and $\chi(\zeta, \theta, \psi)$ comprising the model describe the varying reflected energy from cloud or ocean reflectors as a function of the sun-object-satellite geometry which must usually be taken into account in normalization of real reflectors. The directional reflectance, $r(\zeta)$, is given by:

$$r(\zeta) = \int_0^{2\pi} \int_0^{\frac{\pi}{2}} \rho(\zeta, \theta, \psi) \cos \theta \sin \theta d\theta d\psi \quad [A-6]$$

This is seen to be the total reflectance into the hemisphere from the cloud or ocean element at a given solar zenith angle. χ is defined by:

$$\chi(\zeta, \theta, \psi) = r(\zeta) / \pi \rho(\zeta, \theta, \psi) \quad [A-7]$$

where $\pi \rho(\zeta, \theta, \psi)$ is just the directional reflectance from a given cloud or ocean element when it is considered an isotropic reflector with a constant bi-directional reflectance equal to that from the actual surface in some particular directional defined by (ζ, θ, ψ) .

With these quantities in mind the primed and unprimed versions of Eq. A-7 are created and the ratio ρ/ρ' is formed:

$$\rho/\rho' = \chi'/\chi \frac{r(\zeta)}{r'(\zeta')} \quad [A-8]$$

One small step is needed to put Eq. A-8 into the form for use with the complete reflective model. This is entering the factors $r(\zeta=0)$ and $r'(\zeta=0)$ which are equal because directional reflectance, when the sun is directly overhead of a reflective element, is independent of where that element actually is located on earth. The result is:

$$\begin{aligned} \rho/\rho' &= \chi'/\chi \frac{r(\zeta)/r(\zeta=0)}{r'(\zeta')/r'(\zeta=0)} \\ &= \chi'/\chi \frac{r(\zeta)/r(\zeta=0)}{r'(\zeta')/r(\zeta=0)} \end{aligned} \quad [A-9]$$

Then from Eqs. A-5 and A-9 the normalization factor becomes:

$$n = \chi'/\chi \left(\frac{r(\zeta)/r(\zeta=0)}{r'(\zeta')/r(\zeta=0)} \cdot \frac{\cos \zeta}{\cos \zeta'} \right) \quad [A-10]$$

which is now completely soluble since the geometries of both cloud or ocean element point and normalization point are known, which geometries in turn determine the cloud or ocean model values to be used. Multiplication of the related given digital brightness values and computed normalization factors yields the normalized and thus comparable ATS III pictures.

For the BOMEX July 18 cloud ring study the normalization place-time is chosen as 0N latitude, 46W longitude at local noon on July 19. This date was chosen because of its solar declination of 20N, which defined a part of the solar geometry. The whole normalization condition set was chosen so as to simplify the geometry as much as possible and to also keep those conditions somewhat in the region of the space-time of the study. The usual solar elevation and azimuth equations

are employed and the author has derived the satellite geometry equations used. Since the satellite is fixed with respect to the earth, the satellite geometry remains a constant for any point on earth. However since ATS III is occasionally moved to study various regions, care must be taken to note its subpoint on any pictures used other than a given one as, for example, July 18, 1969 when it was located at 0N, 46W. Also the procedure for normalization used here is to calculate the normalization factors at the midpoints of 1° square areas of the ring study grids and consider these factors valid for the whole 1° square. The calculation of the cloud normalization factors was accomplished by computer using the cloud model and geometry values read in by hand. For the ocean normalization the model was incorporated into the program, while the geometry was the same as before. For any future use of the normalization procedure, which will likely be for other days and times, both the model and the solar and satellite geometry equations will be incorporated into the program (a little less work to say the least).

APPENDIX B

RADAR CLOUD HEIGHT DETERMINATION

I. Cloud Height Geometry

The following describes the derivation of an equation for apparent cloud height from weather radar cloud echo data. The equation is a general one giving the height of a point above its local subpoint on earth in terms of the distance of that point from another given point on the earth surface measured along a plane tangent at that latter point and the angle between the tangent plane and the point whose height is desired. For this derivation the earth is assumed to be a sphere. The general equation is specifically related in this case to the cloud height aspect, where the radar site is the tangent point, the horizontal distance of a cloud element from the radar site is measured from the site along the line tangent at the site, and the radar set antenna (beam center) elevation provides the angle of the cloud element's apparent top above the local surface plane. The angle of interest is that at which the echo disappears, which marks the height point from the above discussion in terms of the cloud top. The geometry for determining cloud height is shown in Figure B1 along with the notation used in the height equation derivation.

Applying the Law of Cosines to triangle OXC with respect to angle $(\beta + \pi/2)$ yields:

$$(R_E + h)^2 = R_E^2 + (\overline{OC})^2 - 2 R_E \overline{OC} \cos (\beta + \pi/2) \quad [B-1]$$

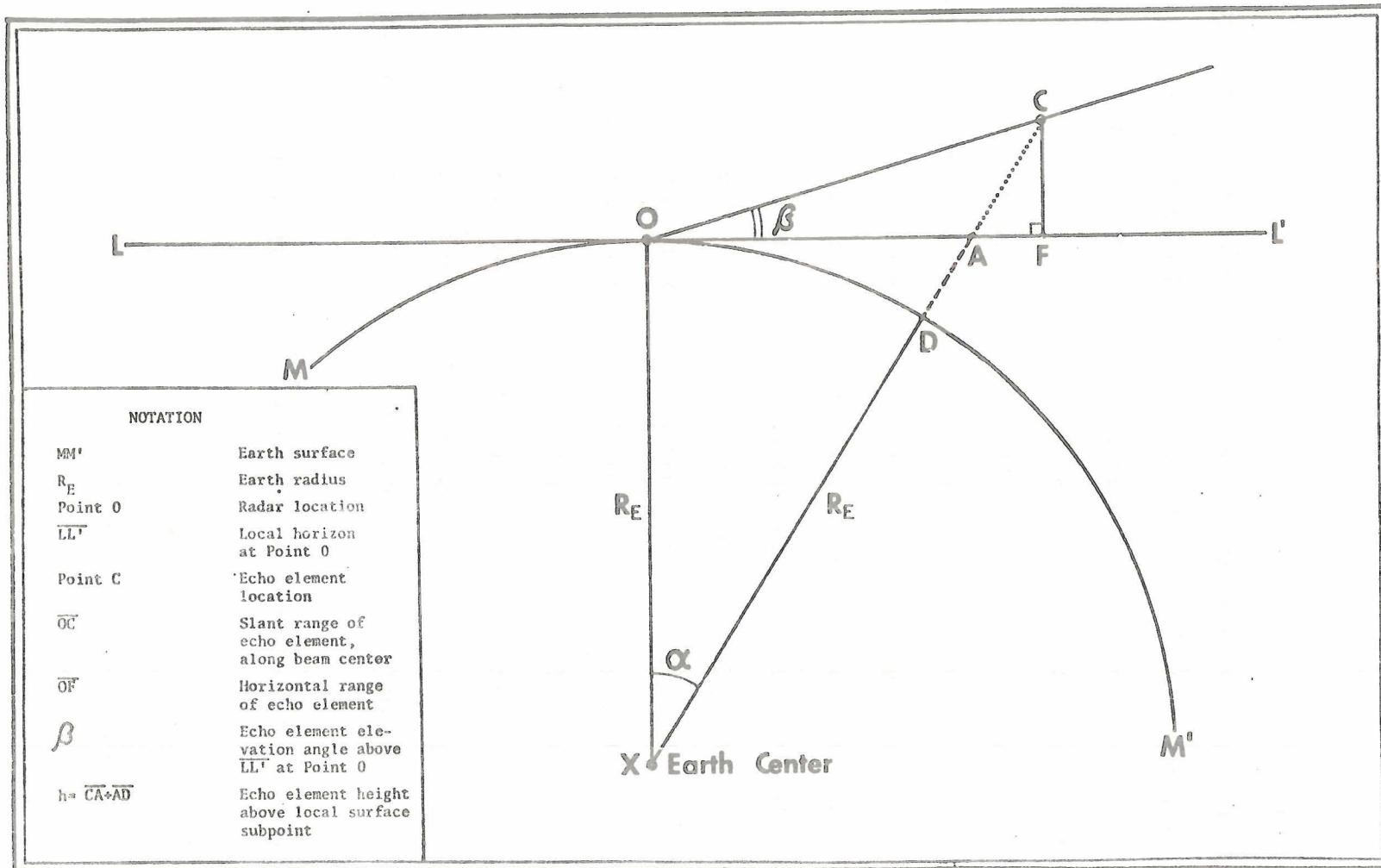


Figure B1 Radar Cloud Height Geometry

Expanding and simplifying the above and using the Quadratic Formula gives for h :

$$h = -R_E + (R_E^2 + \overline{OC}^2 + R_E \overline{OC} \sin\beta)^{\frac{1}{2}} \quad [B-2]$$

Next it is seen that $\overline{OC} \ll R_E$ since \overline{OC} is on the order of several hundred kilometers maximum. The square root term is rearranged into \overline{OC}/R_E terms and the Binomial Theorem is used, neglecting terms of \overline{OC}^3/R_E^3 and higher order, to obtain:

$$h = \frac{\overline{OC}}{2R_E} [1 - \sin^2 \beta] + \overline{OC} \sin \beta \quad [B-3]$$

Now since h is desired in terms of β and \overline{OF} , use the fact that $\cos \beta = \overline{OF}/\overline{OC}$ to obtain:

$$\overline{OC}^2 \cos^2 \beta = \overline{OF}^2 \quad [B-4]$$

Then also $\sin \beta = \overline{CF}/\overline{OC}$ and $\tan \beta = \overline{CF}/\overline{OF}$ which yield:

$$\overline{OC} \sin \beta = \overline{OF} \tan \beta \quad [B-5]$$

Using the relation $1 - \sin^2 \beta = \cos^2 \beta$ and substituting Equations B-4 and B-5 into Equation B-3 yields the final form of the height equation as:

$$h = \overline{OF}^2 / 2R_E + \overline{OF} \tan \beta \quad [B-6]$$

where the tangent term represents that part of the height above the tangent plane and the other term represents the height portion due to the earth curvature away from the radar site tangent point. This equation then can be used with any combination of cloud echo disappearance elevation angles of the antenna and horizontal distances of cloud elements from the radar site to obtain apparent cloud heights. The heights are apparent since such factors as radar beam spread and beam bounce are or may be present. Computer calculation of Equation B-6 is valuable in providing tabular height results, which method is used in the BOMEX cloud ring study.

II. Apparent Cloud Height Correction

The cloud heights determined as described in the first part of this appendix are in question as to their validity, due mainly to beam spread with distance which would yield a cloud height increase with distance greater than that due to earth curvature away from the radar site. The existence of such an anomalous height increase is of interest for the July 18 ring study, but the method discussed here is applicable at all times and in any area. The radar elevation sequences at 1303Z and 1433Z on July 18 are used. For these two times the apparent heights of a total of 105 cloud elements are found using the cloud element echo disappearance elevations and horizontal distances and the computer calculated apparent height tables. These apparent heights are then plotted versus their horizontal distances as shown in Figure B2. The 0° (antenna-beam center) elevation minimum visible cloud heights are also plotted. These heights constitute the lower limit of actual cloud heights visible at given horizontal distances. From the graph it can be seen that the cloud heights do indeed increase with distance from the radar site and at a greater rate than that of the 0° elevation minimum visible cloud heights. A correction is therefore needed. This correction is based on the difference in height increase rate between the apparent cloud heights and the minimum visible cloud heights. The horizontal distance axis on the graph is divided into four 50 nm sections, two best-fit straight lines are drawn through the points of the apparent height distribution and four are drawn through the minimum visible cloud height curve corresponding to the four horizontal distance sections, and in those four sections four differences in height increase rate

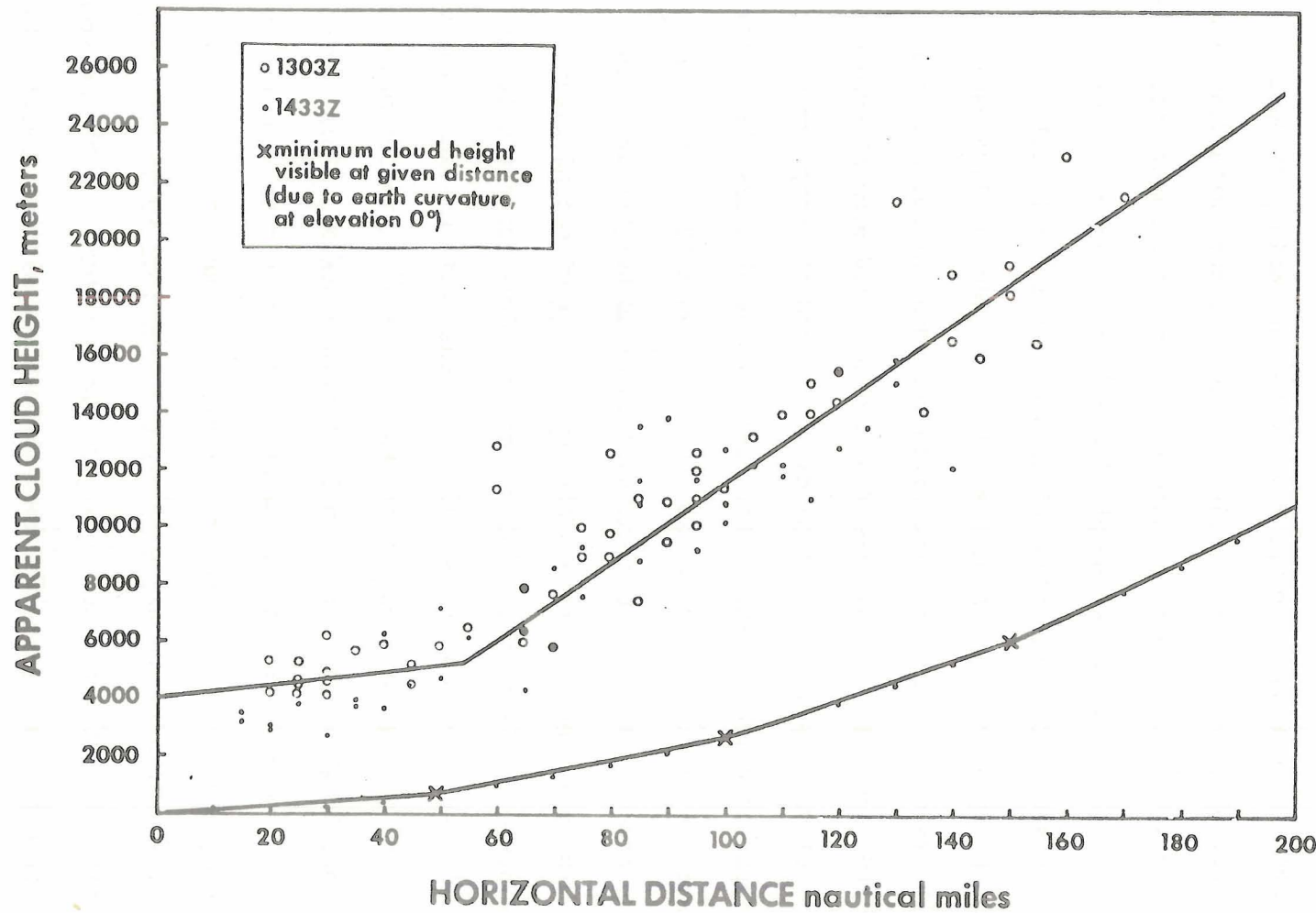


Figure B2 BOMEX July 18 Discoverer Weather Radar Determined Apparent Cloud Heights as a Function of Horizontal Distance from Radar Site with Minimum Visible Cloud Height Curve.

are obtained. From these differences four corrections to the apparent heights applicable in the respective horizontal distance section are obtained. These corrections are then entered in the cloud heights computer program which employed Equation B-6 to obtain the apparent cloud height tabular values and the modified program is rerun to obtain corrected or "true" cloud heights in tabular form in terms of the same echo disappearance elevations and horizontal distances as used before to obtain apparent cloud heights. The correction program also took into account the above mentioned lower limit of "true" cloud heights. The true height tabular results show that the corrections are such that only 1° elevation actual cloud heights at horizontal distances greater than 65 nm are forced below the horizon and therefore the corrections can be considered quite reasonable in regard to the considerations made and in regard to the fact that very few clouds showed echo disappearance elevations of less than 1.5° . Note also that these "true" cloud heights are still subject to some small variations which may exist and which are not accounted for here. One of these is beam bounce from inversions in the atmosphere. Another is related to the nature of determining "exact" echo disappearance elevation by the linear interpolation method used here, such that the actual disappearance elevation is always greater than the nearest lower step elevation and may be biased toward too high values due to assuming linear echo strength decrease between elevation steps, as the real clouds have rather distinct tops. Further the corrections made here are minimum ones, relative to the minimum visible cloud height aspect, such that "true" cloud heights found for July 18 are an upper bound; the

heights are likely somewhat lower. Height increase, other than a possible small amount due to the aforementioned cloud droplet detection characteristics of the 3.2 cm radar, seems very unlikely in view of the nature of the graphical plot of apparent cloud heights and by observation of the true cloud heights found. Further the data used from the radar are those less than 150 nm and preferably 100 nm or less which is the generally accepted range of confidence.

APPENDIX C

POLYGON METHOD DYNAMIC PARAMETER CALCULATIONS

I. Horizontal Divergence

The calculation of the horizontal velocity divergence in a fluid is most commonly accomplished by the Cartesian coordinate system equation:

$$\text{DIV}_2 \vec{V} = \frac{\partial u}{\partial x} + \frac{\partial v}{\partial y} \quad [\text{C-1}]$$

where \vec{V} is the fluid velocity vector with horizontal speed components u and v in the x and y directions respectively. In the atmosphere x and u relate to E-W, positive eastward, while y and v relate to N-S, positive northward. In regard to Equation C-1, the data needed for solution are those along the Cartesian coordinate grid, but in actual practice atmospheric wind observations at surface and upper air sounding stations, which are usually randomly distributed, are rarely of such a rectangular nature. In this random data case the wind observations are utilized according to streamline and isotach analysis or the related u and v component analysis, with interpolation used to pick data values along the Cartesian grid for use in solving Equation C-1. However in some cases the wind data are of such a spacial distribution nature that even the above methods are impractical. A first principles method of horizontal divergence calculation, discussed by Vonder Haar and Smith (1971), covers this latter case and is applicable in the other wind data nature cases as well.

This first principles method is based on the time rate of change of horizontal area of a fluid element due to differences in velocity across the fluid element. The fluid element area boundary is delineated by a chain of given fluid particles. Manipulating the area change aspect in terms of the Cartesian coordinate atmospheric notation yields the horizontal divergence equation:

$$\text{DIV}_2 \vec{V} = \frac{\partial u}{\partial x} + \frac{\partial v}{\partial y} = \frac{1}{A} \frac{dA}{dt} \quad [\text{C-2}]$$

where A is the fluid element area and dt is the time interval over which the area change is measured. Vonder Haar and Smith (1971), utilize the above equality by defining the horizontal area, A_N , delineated by a set of N cloud element "vertices" forming an N -sided closed polygon. Making the assumption that the cloud elements are displaced with the wind, the beginning, mid and end points of displacement are utilized along with the time interval (implicitly indicating wind speed and direction) to obtain the change in the polygon (atmospheric fluid element) area during the given time interval. The positions and displacements of cloud elements are given in terms of the x - y earth coordinate system. Specifically with respect to Vonder Haar and Smith's cloud displacements measured from satellites this system would be the earth's latitude-longitude grid. Derivation notation is as follows:

(a_i, b_i) are beginning points, (x_i, y_i) are mid points and (c_i, d_i) are end points of cloud element displacement which is measured over a time interval of t seconds. The subscript i denotes the cloud element or polygon vertex number with i running from 1 to N and vertices numbered in counterclockwise order around the polygon.

Figure C1 displays the polygon geometry and notation. From the above the area A_N becomes:

$$A_N = \frac{1}{2} \left| \sum_{i=1}^{i=N} y_i (x_{i+1} - x_{i-1}) \right| \quad [C-3]$$

where $\left| \cdot \right|$ denotes absolute value and $i=0 \equiv i=N$ and $i=1 \equiv i=N+1$. From this and the area change the horizontal divergence:

$$\text{DIV}_2 \vec{V} = \frac{1}{A_N} \frac{d A_N}{dt} \quad [C-4]$$

follows as:

$$\text{DIV}_2 \vec{V} = \frac{\left| \sum_{i=1}^{i=N} d_i (c_{i+1} - c_{i-1}) \right| - \left| \sum_{i=1}^{i=N} b_i (a_{i+1} - a_{i-1}) \right|}{\left| \sum_{i=1}^{i=N} b_i (a_{i+1} - a_{i-1}) \right| \cdot \Delta t} \quad [C-5]$$

which is the usable form. It should be noted that divergence is a differential quantity with infinitesimal changes with time and as such A_N is considered constant over the short time interval dt . But in the above the finite difference form of divergence calculation is used and thus A_N changes significantly over the finite time interval of atmospheric observation. Thus the area change must be small compared to the area itself or else there arises considerable ambiguity as to the true value of divergence due to the uncertainty of which A_N value to use as representative of the finite time interval. Also it is noted that the more accurate divergence values will be obtained with an increasing number of polygon cloud element vertices and that the divergence

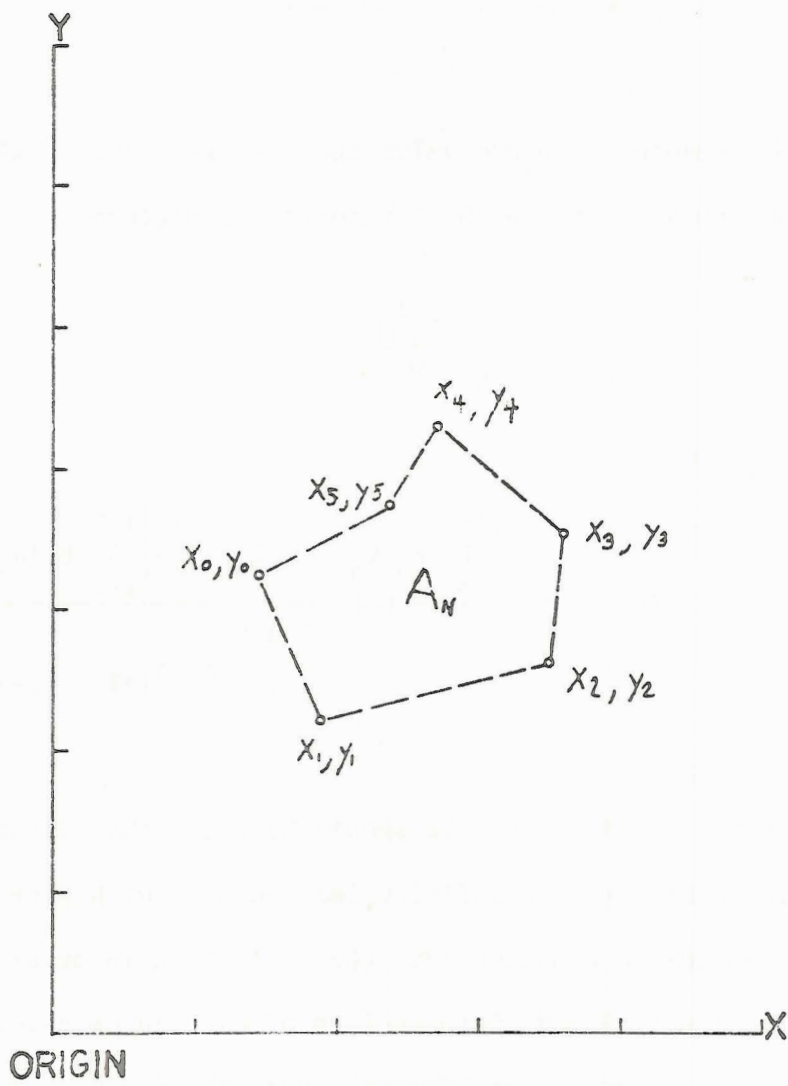


Figure C1 Polygon Geometry and Notation Related to Polygon Method of Horizontal Velocity Divergence Computation (After Vonder Haar and Smith, 1971).

value obtained is a representative mean over the polygon area. Finally it is seen that the polygon method utilizes the same basic wind data as is employed in the more common divergence calculation methods; only the form of the data differs with the method used to obtain horizontal velocity divergence.

II. Relative Vorticity

Atmospheric relative vorticity is commonly represented by the earth grid Cartesian coordinate system (described in its particulars in Part I) equation:

$$\zeta = \frac{\partial v}{\partial x} - \frac{\partial u}{\partial y} . \quad [C-6]$$

This is the third or vertical component of the total vorticity, $\vec{\nabla} \times \vec{V}$, the curl of the fluid velocity. Equation C-6 is of course applicable to any fluid system utilizing Cartesian coordinates and the corresponding velocity components (as discussed in Part I). However Equation C-6 follows from a first principles definition of relative vorticity, that relative vorticity is equal to the circulation per unit area or:

$$\zeta = \frac{C}{A} = \frac{\oint \vec{V} \cdot d\vec{S}}{A} \quad [C-7]$$

where C is the circulation, defined by the line integral around a closed curve bounding the surface area A and $d\vec{S}$ is an element of that curve. \vec{V} is the fluid (wind) velocity vector. Vonder Haar and Smith (1971) proceed from this first principles equation to obtain a working equation for relative vorticity computation in much the same manner as employed in obtaining the divergence equation discussed in Part I of this appendix. Cloud elements again define the closed polygon of area A_N with the closed curve line integral in the vorticity equation being that around the polygon area boundary, cloud element displacements over a given time interval again form the wind velocity

data set, and the position, displacement and other notations are the same as in Part I. Some additional notation is needed here for the relative vorticity equation derivation and it follows below with Figure C2 displaying the particular geometry and notation used in this derivation.

Equation C-7 can be rewritten in summation form, using a definition of vector dot product, as:

$$\zeta = \frac{\sum_{i=1}^{i=N} (V_i) \cdot (dS_i) \cos\theta_i}{A_N} \quad [C-8]$$

with A_N defined as in Part I. Further definitions are as follows:

$$V_i = e/\Delta t$$

$$dS_i = (a+d)/2$$

$$\cos\theta_i = (a^2 + b^2 - c^2)/2ab$$

$$a = \left[(x_{i+1} - x_i)^2 + (y_{i+1} - y_i)^2 \right]^{1/2}$$

$$b = \left[(x_i - a_i)^2 + (y_i - b_i)^2 \right]^{1/2}$$

$$c = \left[(x_{i+1} - c_i)^2 + (y_{i+1} - d_i)^2 \right]^{1/2}$$

$$d = \left[(x_{i-1} - x_i)^2 + (y_{i-1} - y_i)^2 \right]^{1/2}$$

$$e = \left[(a_i - c_i)^2 + (b_i - d_i)^2 \right]^{1/2}$$

From the above the working equation for relative vorticity computation by the polygon method follows as:

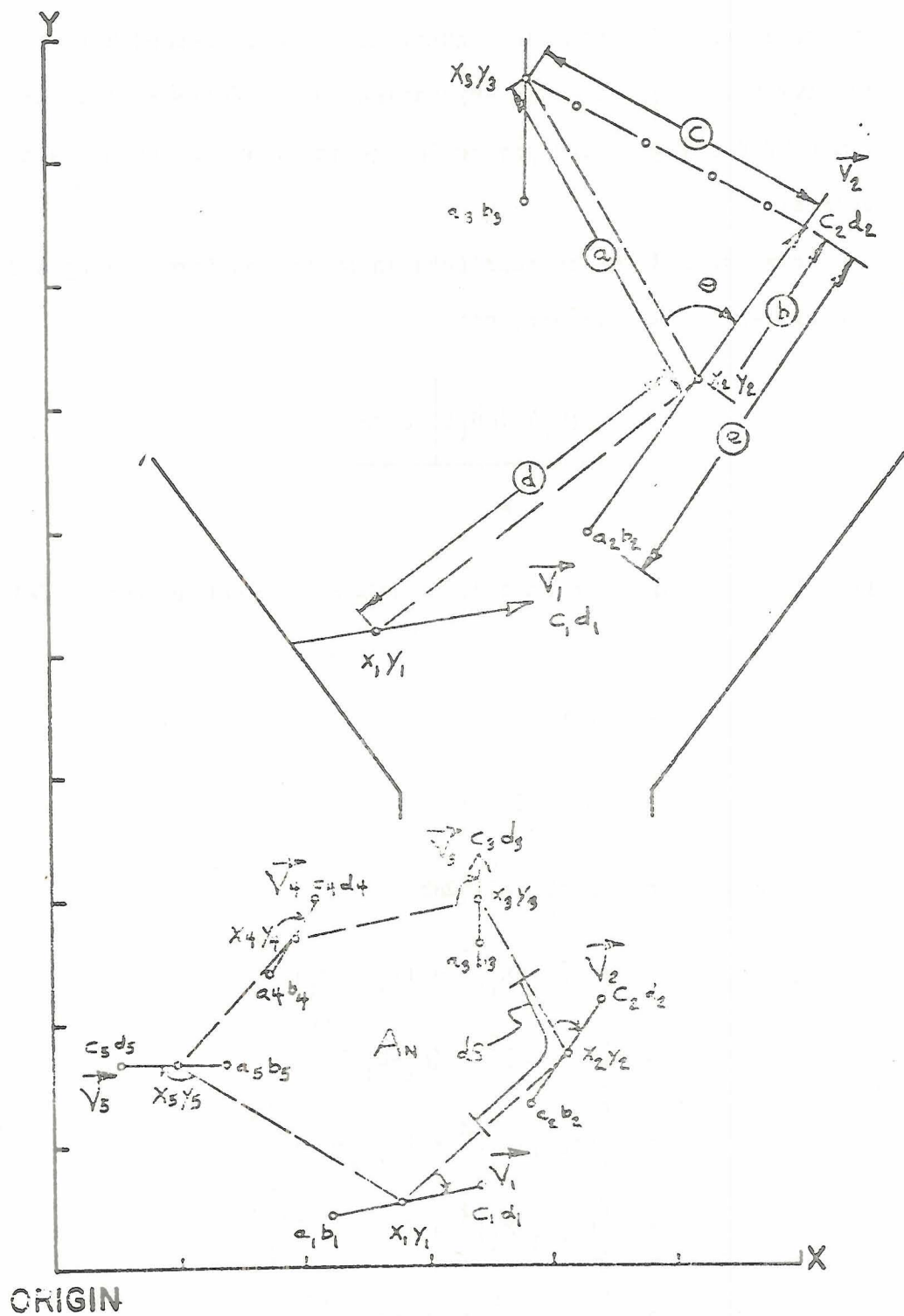


Figure C2 Same as Figure C1 for Relative Vorticity (After Vonder Haar and Smith, 1971).

$$\zeta = \frac{\sum_{i=1}^{i=N} \left[\left| \left(\frac{e \cdot (a+d)}{\Delta t} \right) \right| \cdot \left| \frac{a^2 + b^2 - c^2}{2ab} \right| \right]_i}{\sum_{i=1}^{i=N} y_i (x_{i+1} - x_{i-1})} \quad [C-9]$$

The latter two notes in Part I regarding wind data and dynamic parameter calculated value validity are equally applicable here.

